ONIRICA
A Conceptual Design Study of a Large FoV Near-IR Imager for OWL

OWL-CSR-ESO-00000-0165

Issue: 1.0
14th October 2005

Responsible: Ragazzoni Roberto[1]

Authors: Ragazzoni Roberto[1], Arcidiacono Carmelo[1], Bertelli Giampaolo[4], Castellano Marco[2], Diolaiti Emiliano[3], Falomo Renato[4], Farinato Jacopo[1], Fontana Adriano[2], Gaessler Wolfgang[5], Grazian Andrea[2], Greggio Laura[4], Le Roux Brice[1], Lombini Matteo[1], Herbst Tom[5], Rix Hans-Walter[5]

Institutes: [1] INAF-Osservatorio Astrofisico di Arcetri (Fi) - Italy

[2] INAF-Osservatorio Astrofisico di Monte Porzio (Roma) – Italy

[3] INAF-Osservatorio Astronomico di Bologna (Bo) – Italy

[4] INAF-Osservatorio Astronomico di Padova (Pd) – Italy

[5] Max-Planck-Institut für Astronomie (Heidelberg) - Germany

EUROPEAN SOUTHERN OBSERVATORY
Organisation Européenne pour des Recherches Astronomiques dans l'Hémisphère Austral
Europäische Organisation für astronomische Forschung in der südlichen Hemisphäre

Change record

Issue	Date	Section / Paragraph affected	Reason / Initiation Documents / Remarks		
1.0	14.10.2005	All	First Issue of the Document	Author(s)	Ragazzoni R., Arcidiacono C., Bertelli G., Castellano M., Diolaiti E., Falomo R., Farinato J., Fontana A., Gaessler W., Grazian A., Gerggio L., Le Roux B., Lombini M., Herbst T., Rix H.W.
				Approval	

Content

	Abbreviations	Symbols	
AD	Applicable Document	r_0	atmospheric turbulence coherence length
ADC	Atmospheric Dispersion Compensator	L_0	atmospheric turbulence outer scale
AO	Adaptive Optics	C_n^2	integrated atmospheric turbulence profile
CCD	Charge Coupled Device	τ_0	atmospheric turbulence coherence time
CDM	Cold Dark Matter		
CMB	Cosmic Microwave Background		
DM	Deformable Mirror		
FOV	Field of View		
GLAO	Ground Layer Adaptive Optics		
HST	Hubble Space Telescope		
JWST	James Webb Space Telescope		
ICD	Interface Control Document		
IGM	Inter Galactic Medium		
LBCIMSIM	Large Binocular Camera Image Simulator		
MCAO	Multi-Conjugate Adaptive Optics		
NIR	Near Infrared		
OWL	OverWhelmingly Large Telescope		
PSF	Point Spread Function		
RD	Reference Document		
SF	Star Formation		
SFH	Star Formation History		
SFR	Star Formation Rate		
SN	Supernovae		
SNR	Signal to Noise Ratio		
UV	Ultra Violet		
WF	Wave front		
WFS	Wave front sensor		

1 Scope

The scope of this document is to report a conceptual study of an imaging camera that should fully exploit the sensitivity and the spatial resolution capabilities of OWL in the near-IR. This camera will take advantage of a low order correction exploited by an MCAO system. The conceptual study includes also the very preliminary design of the MCAO wavefront sensor that drives the tertiary adaptive mirror of the telescope with the purpose to remove essentially the layers close to the ground. Provisions to extend the design of the WFS to full MCAO correction are also presented. An analysis of the relevant science cases is carried out together with a simulation of the possible results that the camera could achieve, above all in term of sky coverage and limiting magnitudes and when compared to possible 30-60 meters class competitor telescopes.

2 References and applicable documents

2.1 References

Reference documents about the ESO OWL concept study can be retrieved from the web at www.eso.org/owl. These documents shall be taken as background information only; in the event of conflict between these documents and the present one, the contents of this shall be considered as superseding.

No	Title	Doc. Number	Issue
RD1	Ragazzoni, R. & Farinato, J., "*Sensitivity of a pyramidic WaveFront sensor in closed loop Adaptive Optics*" A&A 350, L23 (1999)		
RD2	Ragazzoni R. et al, "*A smart fast camera*" in Ground-based Instrumentation for Astronomy, Alan F. Moorwood, Masanori Iye, eds, Proc. of SPIE, 5492, pp.121-127 (2004).		
RD3	Ragazzoni R. et al.,"*Arbitrary small pupils in Layer Oriented Multi-Conjugate Adaptive Optics*", PASP, Volume 117, Issue 834, pp. 860-869.		
RD4	Xompero M. et al., *"An active wave front sensor to make feasible on 100mt class tlescope"*, Proceedings of the SPIE, Volume 5382, pp. 588-594 (2004).		
RD5	Conan R. et al., "*Wavefront outer scale measurements at San Pedro Martir observatory, its impact on adaptive optics performances*", RevMexAA (Series de Conferencias), 19, pp.31-36 (2003)		
RD6	Monet D. G. et al., "*The USNO-B catalog*", *Astronomical Journal*, 125, pp. 984-993, 2003.		
RD7	Oke, J.B. 1974, ApJS, 27, 21		
RD8	Grazian A. et al., 2004, PASP 116, 750		
RD9	Giallongo et al. 2000 ApJ 530L , 73		

RD10	Bouwens et al. 2004 ApJ 611L, 1		
RD11	http://www.maccon.de/FTPROOT/schrittmot_d.pdf		
RD12			

2.2 Applicable documents

The following applicable document of the exact issue shown forms a part of the present document to the extent specified herein. In the event of conflict between the document and the content of the present specification, the latter shall be taken as superseding.

No	Title	Doc. Number	Issue
AD1	6-mirror solution, f/1.25 primary mirror Optical design and properties	OWL-CSR-ESO-00000-xxxx	1
AD2			

3 Introduction

A very large optical-infrared telescope will allow us to derive the important processes of galaxy formation and evolution in the full range of environments. Several complementary lines of attack are possible, directly connecting present-day Universe with the high redshift Universe, where the old stars near the Sun formed. Both the star formation histories of galaxies and the mass assembly histories of galaxies will be elucidated. We know that interactions and mergers between galaxies occur and play a (probably crucial) role in determining the morphological type of a given galaxy, but we do not know what merged, or when it merged - how do the merging histories of (non-baryonic) dark matter and of baryons compare? Similarly, stars clearly form(ed) at some rate from gas, but at what rate, where, with what stellar Initial Mass Function, and what were the effects of this star formation on the remaining gas? What is the connection between galaxies and the supermassive black holes at their centres? Again, the unprecedented spatial resolution of a 100m-class telescope, comparable to those achieved by VLBI in the radio, will provide unique insight. Thus Extremely Large Telescopes (ELT) will provide the data that are required to underpin an analysis of the physical properties of galaxies over the age of the Universe. ELT as envisaged is a critical component of a multi-faceted approach to understanding our Universe. GAIA will provide the astrometric capability that is impossible from the ground, supplying proper motions and distances. ELT complements and thus strengthens the capabilities of ALMA, which focuses on analyses of the dust and gas content of galaxies.

In this document we report a conceptual study of an imaging camera that should fully exploit the sensitivity and the spatial resolution capabilities of an ELT in the near-IR. We first briefly review the issue of the Point Spread Function (PSF) shape vs. the achievable Field of View (FoV) under the general constraint of observations in superb seeing conditions. These will be obtained in the context of Multi Conjugated Adaptive Optics (MCAO) or Ground Layer correction Adaptive Optics (GLAO).

Then we give a preliminary estimation of the expected performances in terms of SNR and limiting magnitude and compare with other smaller ground based and space based future and/or planned possible facilities.

Based on the above constrains we thus present a number of scientific cases that could greatly benefit from the use of such imaging capabilities.

Finally, once the latter are well focused, a preliminary opto-mechanical design with a discussion on the possible range of options one can envisage for such an instrument are sketched out.

4 General considerations

An imaging camera for a telescope is usually considered a general-purpose instrument. In contrast with other kind of more complex instruments, which can be designed following a very specific scientific objective, this kind of instruments is the outcome of a number of iterations between technical capabilities and scientific cases. Being this an instrument that is supposed to be mounted on a telescope of very large aperture, possibly in competition with space observatory James Webb Space Telescope (JWST) and other large (around 30m) aperture class telescopes, the scientific cases used for references cannot be thought as achievable in a comfortable manner. In this document we have tried to stretch capabilities and ambitions of the scientific cases in order to outline a scenario of outstanding technical performance and scientific achievements.

4.1 Background and Statement of Work

The large collecting area of a ground based ELT, together with its high resolving power, can provide unique observations of extremely faint and distant objects. However, in order to reach this goal it is mandatory that the telescope be able to deliver nearly diffraction limit images.

In fact it is only under these circumstances that an ELT can gain significantly with respect to smaller aperture telescopes because of the increased contrast of sources with respect to the underlying background (sky emission).

These constraints led us to a concept of imaging camera that is working at (or it is very close to) the diffraction limit condition. Since the telescope will be operative from the ground this will be possible mainly during the fraction of time when excellent seeing conditions occur. Therefore scientific cases doable with 10 or 20 percentile of the night time are preferably treated and used as driver for the design of the instrument. While the final site, and its detailed atmospheric model, is still unknown there is a large consensus on the typical atmospheric profiles of the best-known sites in the world. Therefore in this work we adopted the typical atmospheric conditions of very good nights in the best known sites. This is further taken into account keeping in mind that the camera, especially in its wavefront sensing part, must be fast enough in order to exploit the superb seeing periods.

The goal of building up a camera that could outperform other similar ground based and space based instruments leads to a rather limited Field of View (FoV).

The FoV size is mainly driven from the optimism in the turbulence structure one can expect in the superb seeing conditions shifts rather than from technical considerations. A camera capable of deliver fully AO corrected images over a FoV of about one arcmin, and hence reaching very faint magnitude limits for point sources, is the only option to be safely ahead of other instrumentation by a significant margin. This FoV size also constraints, to a certain extent, the scientific case classes toward faint and point like sources. As this does not completely exhaust the possible range of scientific interest we conceived an additional channel that can (but not necessarily must) be configured as a piggy back one, basically deployed around the central one where emphasis is given to the covered field rather than to the optical quality. We have foreseen a field of about 3 to 6 arcmin in diameter. We just note here that the latter option could be in some way vignetted as listed in Instrument interface AD1 for FoV larger then 3arcmin.

The technology adopted for the two channels, although very different (in one case the focal length is augmented, in the other is reduced), is aligned with the finest opto-mechanical instrumentation for Astronomy available nowadays. We assumed no, or moderate (up to a factor of two), technological developments in the realms of the available detectors. This makes the overall layout rather compact and comparable in size and weight to the largest 8m class instruments, reinforcing its credibility and manufacturability. Given these conditions we also preliminary sketched a possible implementation in the OWL instrument bay allowing to use such a camera as add-on instrument to a larger one, hence not completely filling one of the six instrument bays foreseen.

4.2 Basic constraints on the imaging camera

While the detailed evaluations of the basic parameters of the camera are left to the following sections it is nevertheless interesting to figure out which is the range of parameters where such figures should lie. Key parameters are, in fact, the pixel size, and the covered Field of View. Because of the willing to achieve as main goal outstanding performances a good sampling of the diffraction limited PSF is mandatory. In the second, wide field channel, the choice can be, on the other hand, much more free. This leads to a pixel size of the order of the milliarcsec (mas) in the central channel and in a much wider range, even allowing big pixel sizes as several ten of arcsec for the outer wide field channel, an option considered here, however, of second priority. This leads to focal ratio in the range of F/10..F/40 for the central channel and

even of some very fast F/1.5…F/2 for the wide field one. The latter can be achieved only through some specific technologies in order to be doable with reasonable costs, if not doable at all. The exact figure also depends upon the choice for the pixel size although current technology leaves not a lot of freedom in this respect. However, a through discussion about detectors is reported in the following sections of the document.

As a rule of thumb for the Field of View one should recall that the adoption of MCAO with two Deformable Mirrors (DM), under a (very unlikely) uniform turbulence column distribution, leads to a corrected Field of View about four times larger than the conventional isoplanatic angle. Given typical values of the order of ten arcsec an achievable fully exploited diffraction limited performances can be thought lying in the range of half to one arcmin in diameter. Superb seeing conditions, the ones assumed for the design of this instrument, and isoplanatic angle are not clearly correlated as this can crucially depends upon the selected site and its atmospheric conditions. It is reasonable, however, to consider that good seeing and superb seeing could differs substantially from different conditions in the boundary layers while than on high altitude atmosphere where generally speaking the conditions are by far more stable, other than seasonal variations. This leads to an isoplanatic patch, and hence to a definition of the maximum achievable Field of View in MCAO mode, that is likely to be not so dependent from the percentile of better seeing one will choose to design this camera, basically confirming the expectations of the figure of 30 to 60 arcsec in diameter above mentioned.

The wide FoV channel is affected by a more difficult analysis. Here we just point out that an upper limit is imposed by the opto-mechanical constraints of the telescope and that such an add-on would be significant only with a minimum diameter allowing for a significantly larger size than the narrow field channel, a constraints placing the minimum diameter in a range of a factor 2 to 3 with respect to the fully diffraction limited channel. As one can see these figures (and the corresponding number of pixels, a factor driving some of the cost of the camera and of the efforts in the storing and data reduction that such a camera poses, an issue not treated here) at the very end can range of more than an order of magnitude depending upon several choices. While in the following we will try to outline the reasons for this or that approach and hence to the final figure we are dealing with, we understand that using an identical approach, a design of a camera with significantly different figures can be traced out. There is, in this respect, some part of arbitrary choices done in a few steps in the design process of which the reader should be aware.

4.3 Scenario for competitions

The James Webb Space Telescope (JWST) is a large, infrared-optimized 6.5m diameter space telescope scheduled for launch in 2011. JWST is designed to study the earliest galaxies and some of the first stars formed after the Big Bang. These early objects have a high redshift from our vantage-point, meaning that the best observations for these objects are available in the infrared.

JWST will be equipped with near-infrared imaging camera (NIRCam) with a FoV of 2.2 × 4.4 arcmin (sampling 0.0317”, 4k×4k array) in the wavelength range 0.6 to 2.3 μm.

Given the location of JWST, permanently in Earth’s shadow at about 1.5 million kilometres away, and the low level of background expected for this telescope, it will deliver images with 0.05” resolution down to K ~ 29 for point like sources.

5 Technical and scientific constraints

5.1 Expected AO performances and PSF simulations

The expected performances of the possible AO corrections can be roughly predicted to a certain extent even without end-to-end simulations by analyzing such a problem from a theoretical point of view and, whenever possible, comparing the ELT case to the 10meter class telescopes case already investigated.

5.1.1 PSF shape vs. FoV and AO mode

Both likely types of AO modes will provide a relatively large field of view (roughly from 1' to 6') for astronomical observations: Multi-Conjugate Adaptive Optics (MCAO) systems and Ground Layer Adaptive Optics (GLAO) systems. While both are using an ensemble of wave-front sensors fed by natural reference stars or Laser Guide Stars (a case not considered here) to measure the volume of turbulence and correcting the same volume with a (small) number of deformable mirrors.

A GLAO system is based on the fact that on the pupil, or at least at low altitudes, the effects of the atmospheric turbulence is essentially invariant (isoplanatic) along a variety of directions. Strictly speaking, given a certain spatial detail on the telescope entrance pupil up to which the correction is going to be performed, a certain slab of turbulence will be corrected approximately in the same manner once different directions will displace one to each other less than such a distance. This imposes some simple constraints on the thickness of the turbulence corrected versus the covered FoV. The larger the FoV the thinner will be the compensated turbulence and less effective will be the correction. Theoretically using a single mirror on the pupil allows then correcting, at least partially, the turbulence in the whole field of view. In practical, a GLAO system, composed of only one mirror on the pupil, allows to obtain a partial correction on a 4'-6' field of view.

A Multiconjugate Adaptive Optics system is based on the correction of the volume of turbulence by a volume of correction, meaning several mirrors, located at different altitudes. As the lower mirror is not *a priori* located on the telescope pupil, the theoretical corrected field of view is limited but as there is one (or more) other mirror located in altitude, it is possible -in principle- to obtain a complete correction of the whole turbulence in such a field of view. Again, the widest correction will allow to compensate only for the turbulence located closer to where the Deformable Mirrors are conjugated, leading to a trade off between the achieved FoV and the quality of the compensation. It is generally considered that an MCAO system, for a 10m class telescope, using 2 or 3 mirrors, can achieve a good correction on a field of view of 1'-3'.

We now review briefly how scaling laws generally adopted for such a kind of systems on 10m class telescopes does no longer apply, or apply in a modified fashion, for a 100m class telescope.

5.1.2 Ten meter class to one hundred meter class telescope AO

The behaviour of the adaptive correction is different going from 10 to 100m, class telescopes: on diameter (D) size larger than the turbulence outer-scale (L_0) it starts to play a role also without any correction, in open loop conditions. Moreover, for a 100m telescope, D/r_0 is extremely large and the size of the halo (λ/r_0) compared to the core (λ/D) becomes huge, and then the surface brightness of the halo is very faint. We notice that a Strehl Ratio of 30% for D = 100m is equivalent to a Strehl Ratio of 99.5% for D=8m. This would suggest that an AO system for an ELT can reach quite easily the Planer Finding regime thanks to the high contrast peak/halo. For ELTs, Ground Layer Adaptive Optics and MCAO are both possible to extend the isoplanatic patch, but the PSFs of both systems are quite different.

If we scale the characteristics of a 10m class MCAO system to a 100m class telescope, there is one of the main elements that remains always unchanged, which is the atmospheric turbulence. Obviously, neither layer altitudes neither atmospheric parameters are changed because of the scaling.

This implies a first immediate consequence on the footprints of the telescope along two directions at different altitudes. Figure 1 presents two footprints for a 10 m telescope and a 100 m telescope at a given altitude and for a given field-of-view. In the 10m-telescope case, the footprints are totally separated and the turbulence is uncorrelated from one footprint to the other. In the 100m-telescope case, the footprints are still overlapping a lot and the correlation is high. This is particularly true for the lower modes of correction that, hence, will be essentially identical for various points over the Field of View.

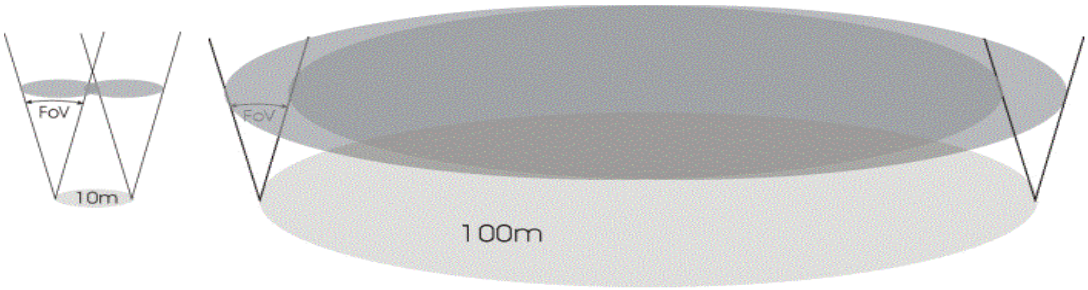

Figure 1: Effect on the telescope footprints of the scaling from a 10 to 100m telescope

The immediate consequence is that, the turbulence contained in the higher layers cannot be seen nor corrected by a single mirror on the pupil plane in the case of the 10m class telescope, while in the 100m telescope case, the higher layers are partially sensed and corrected by the AO system.

In any case this implies a more efficient correction for a 100m class telescope. However GLAO systems performances cannot be scaled directly from 10 to 100m telescopes case, while MCAO systems can, as long as they are not based on the correction of one only layer but all layers.

5.1.3 GLAO case

In this section the analysis of the Point Spread Function for OWL-like telescope is presented. Because of the large difference existing between 60-100m class telescopes and existing 8-10m telescopes it is not possible to scale the performance to such a dimension at least for GLAO case. In fact on these large sizes the overlap of the reference pupils is much larger. Now we define the limit altitude:

$$h_{lim} = D/FoV$$

where D is the diameter of the telescope and FoV is the technical Field of View defined by the direction of the AO reference stars. This altitude h_{lim} corresponds to the height where there is no more overlap between 2 references at opposite FoV limit positions. For the WFS is not possible to sense any frequency of this turbulent layer using the two stars considered

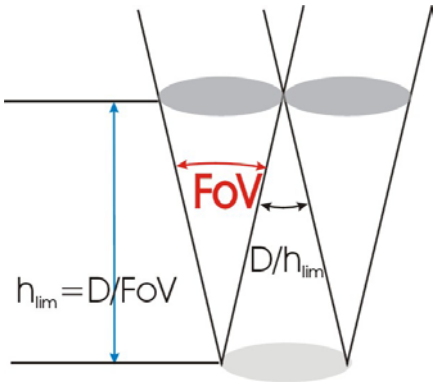

Figure 2: In this picture the h_{lim} is explained. It represents a typical altitude or a characteristics altitude where the layer phase aberration cannot be reconstructed using stars at the limit of the technical FoV used for WFS measurements.

h_{lim}	D=8	D=30	D=60	D=100
FoV=2'	14km	51km	103km	171km
FoV=4'	7km	13km	26km	86km
FoV=6'	5km	17km	34km	57km

Table 1: In this table are listed the characteristic limiting altitude for different telescopes and different telescope diameters. For diameters larger than 30m the limiting altitude is much larger than the uppermost turbulent layers in the atmosphere.

This implies that in adaptive systems with Deformable Mirrors (DM) conjugated at altitudes separated less than the distance $2\times h_{lim}$ all the possible layers are corrected (at least low frequencies) also with GLAO.

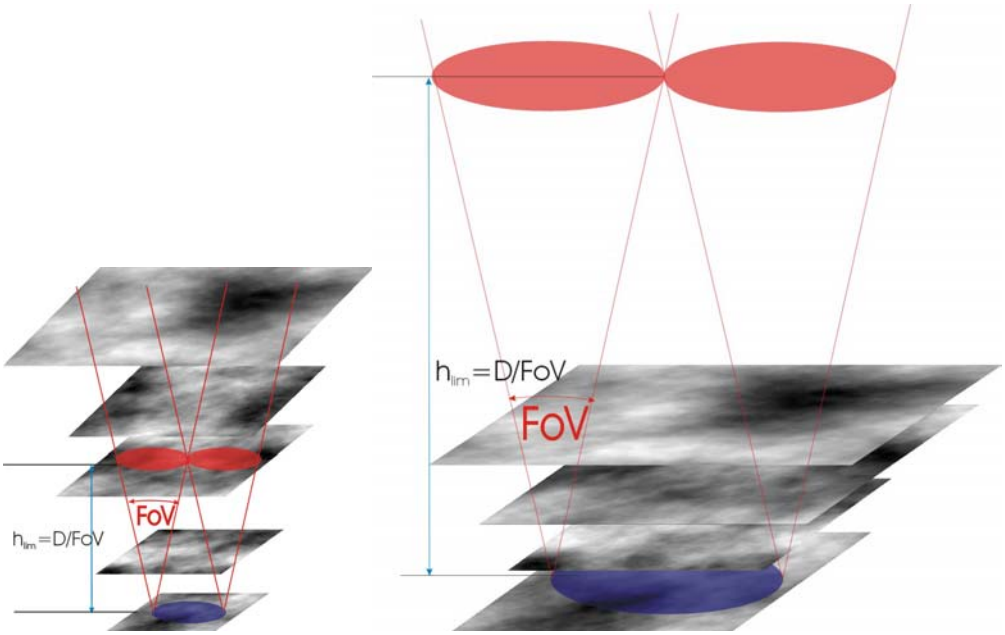

Figure 3: The two images present the GLAO geometry for an 8-10m telescope and a 100m class telescope (respectively on the left and on the right). Using the same technical FoV for the AO references the 100m case has h_{lim} altitude 10 times larger than the 10m case. This changes completely the behaviour of the correction, because in a case the high altitude turbulent layers are above h_{lim}, while in the 100m case they are at altitudes much lower than that one.

Up to 8m diameter h_{lim}<7km, much less than the maximum altitude of several turbulent layers (according to the model this altitude is H_{max} = 15-20km), then high layers (>7km) are unseen and uncorrected. This implies that, while ground layer is corrected the high layers are not corrected at all, and on the corrected PSF they work generating a small seeing disk of the order of $\lambda/r_{0,High}$ ($r_{0,High}$ is the coherence length of the high turbulence). Over 20m diameters the $h_{lim}>H_{max}$ and also high layers are low order corrected: on extra-large telescopes all possible layers are seen by the sensor and corrected by the DM, even if with decreasing accuracy for the higher ones. When $h_{lim}>H_{max}$, the PSF is composed by the diffraction limited spot over a depressed halo-seeing disk. GLAO for ELT moves the energy in the central peak directly without an efficient high-seeing reduction, or energy concentration. GLAO benefits of the ground removal: the high layer seeing disk defines the PSF energy distribution, excepting the diffraction-limited spike, which is not avoidable. Increasing the correction by using smaller sub-aperture for the pupil sampling, or using smaller technical FoV the SR is more and more high, while the seeing halo more and more depressed. In open loop (case without any AO) also small outer-scales behave such as a correction, moving the energy from the seeing halo disk to the diffraction peak (RD5). But this effect becomes important for outer-scales smaller than 15 meters.

In a GLAO system, for a 10m telescope, as the higher layers are not sensed and then they are not correctable: the contribution of the higher layers on the total PSF is like a small seeing disk of $\lambda/r_{0,High}$. On the other hand, for a 100m telescope, the high layers are partially measured and corrected by the system and they contribute to the total PSF generating a depressed halo seeing disk.

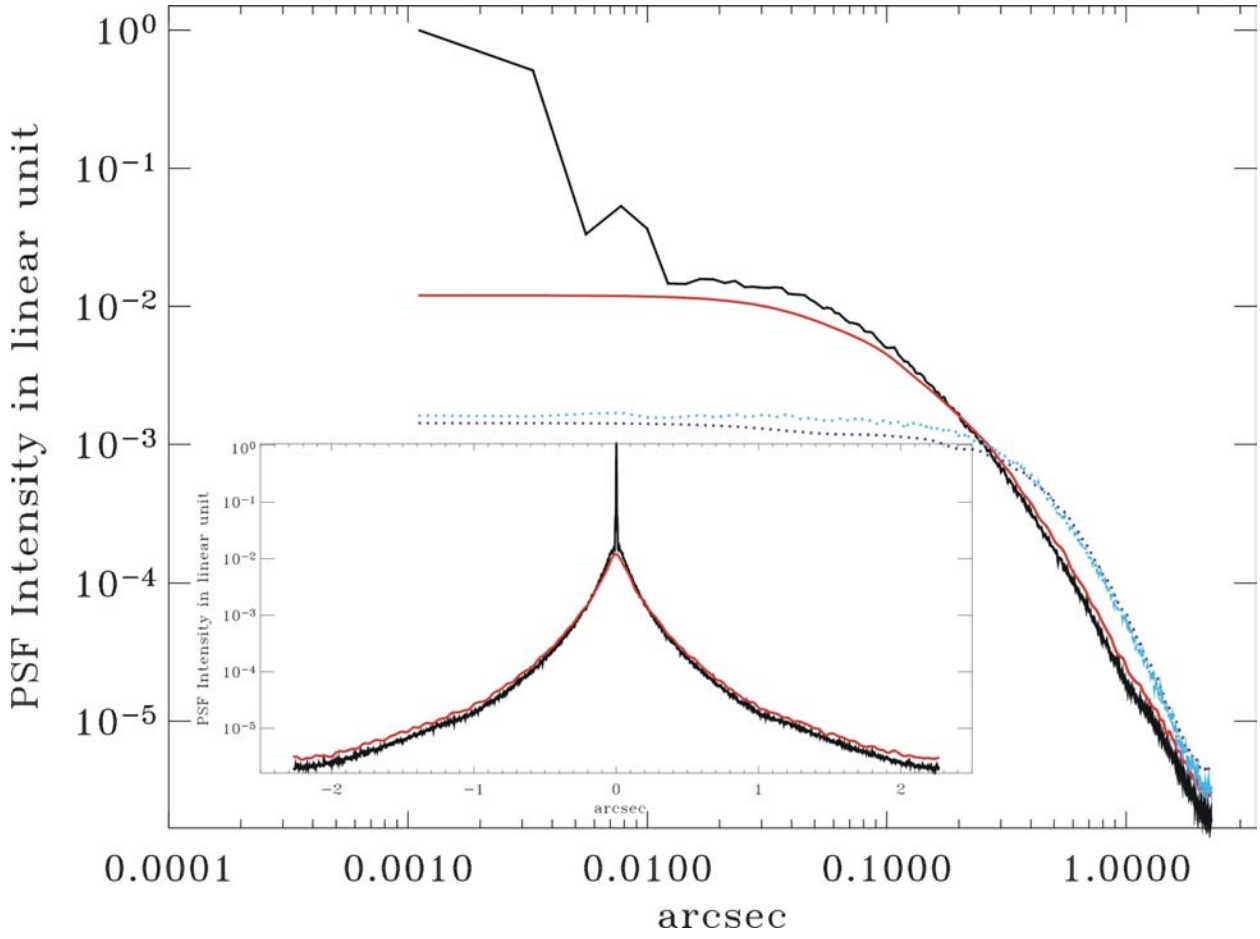

Figure 4: This figure shows the expected PSF profiles for 10 (in red) and 100m telescopes. The plot is in log-scales, while the inset shows the two PSF profiles with arc second linearly plotted. The dotted lines represent the profile of the seeing disk for both 10 and 100 meter telescopes.

On Figure 4 is represented a total PSF for a GLAO system on a 10m class telescope (red) and on a 100m telescope. In both cases the ground layer turbulence is well corrected while the high layers behave in

different manner in the two cases. The little spike at the top of the 100m PSF corresponds to the diffraction-limited core of the partial correction of whole atmosphere and below it, the "seeing" halo due to the uncorrected high altitude layers. The behaviour of the 10m telescope correction follows the 100m down to spatial distance from the center of the PSF of the order of $\lambda/r_{0,High}$, then the two PSFs go differently: the 10m shows a "plateau" (approximately Gaussian function with FWHM $\approx\lambda/r_{0,High}$) while the 100m PSF presents over this the diffraction limited core.

Figure 4 helps to understand that a GLAO system for an ELT does not allow concentrating efficiently the energy on the PSF, even if the Strehl Ratio (SR) computed on the center of the PSF can be good.

In a PSF the dimension of the disk depends strongly on the power in the high spatial frequencies. In 10m GLAO correction the high layers are not corrected at all, introducing their phase disturbances in the observed WF. In 100m the high frequencies of the high layers are corrected by the GLAO system and the resulting PSF given by a diffraction spike due to the partial correction and a "seeing disk" halo due to the high order unseen modes (see Figure 5).

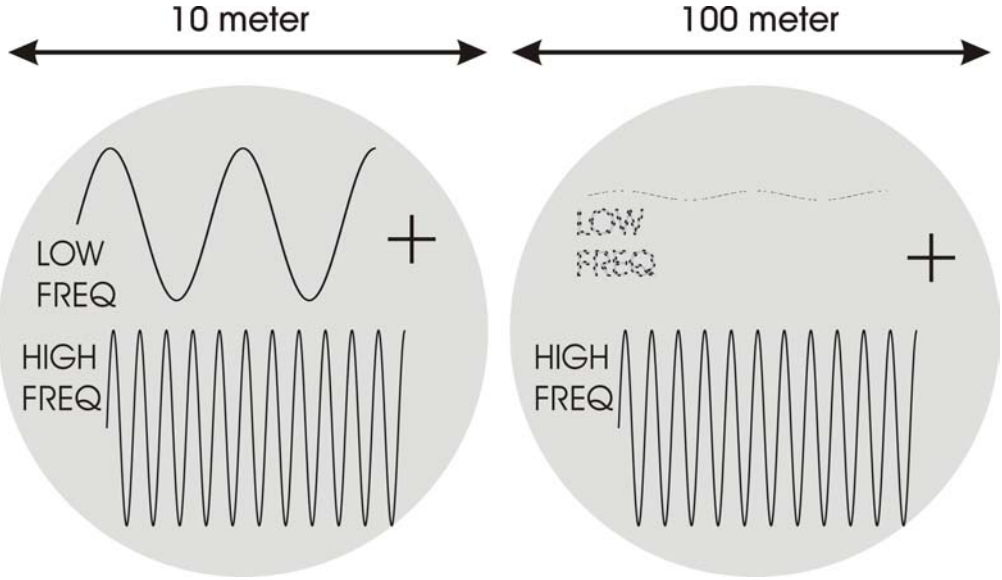

Figure 5: In this figure are graphically presented the components of the phase aberration in the WF observed by 10m (left) and 100m telescope (right), after the GLAO correction. In the 10 meter case all the turbulence relative to high altitude layers introduce WF-aberrations in the whole spatial frequency domain, while in the 100m star WF the all low order modes (high layers too) are corrected by the GLAO system. In both cases the Ground Layer turbulence has been completely corrected.

On the other hand, many astronomical tasks (for example in extragalactic astronomy or cosmology) require more energy concentration than good narrow PSF for signal to noise reasons (background) that requirements that go in the opposite direction, towards the correction of the high frequencies. However the Ground Layer removal retrieves at most PSF large as $\lambda/r_{0,High}$ that, depending on the site, is about 0.3arcsec at the K band, but can be much narrow in very special site as DOME-C (≈0.1arcsec) characterized by very small high layer turbulence.

5.1.4 Full MCAO case

As it requires several mirrors to correct efficiently all altitude layers in any case (10m or 100m telescope), the problem presented for the GLAO case, linked to the partial-correction of higher layers, is inexistent in MCAO and such system performances can be scaled directly from 8m existing systems. Its total PSF is then of the form of Figure 4 without the halo-seeing from uncorrected high altitude layers.

5.2 Do we have to deal with a seeing limited mode?

The limit case for the PSF shape with respect to the efficiency of the AO correction is, of course, when the AO correction is missing at all, because of its inability to deal with the conditions of the atmosphere and/or of the reference stars available, or because of technical down time. In case of single reference star AO, the FoV around the corrected star, moreover, will be of a rather low SR, although, as we discussed before, still significantly better than a pure seeing limited case. These considerations raise the point if the camera should incorporate the ability to deal in a seeing limited mode. From the point of view of peak performances the answer is quite obvious. The gain in limiting magnitude with respect to a 10m class telescope, equally seeing limited, is just a mere 2.5mags, and the comparison with any NIR telescope, because of the background difference, outperform any seeing limited camera in the NIR. In the visible, however, such a difference is much less dramatic, especially considering that competition will be weaker. This could leads to the concept of a wide FoV camera tuned to very good seeing conditions, or to seeing conditions ameliorated by GLAO or MCAO, or even conventional AO on axis, in the NIR, and just seeing limited in the visible. Any of these configurations will not leads to a directly outstanding scientific achievement, unless of a dedicated use to a restricted specific target. This suggests a configuration where, further to a NIR relatively wide field, MCAO assisted camera in the centre of the FoV, a NIR very wide field camera with a pixel sampling a moderate resolution (several diffraction limited core size) around it and a similar camera (even with a coarser pixel size) around a central FoV of, for example, a spectroscopic instrument. It is of course questionable if such piggy-back instruments will really be of big relevance and they are just mentioned here. It will be shown, however, on technical grounds, that such a kind of instrumentation (wide FoV with a proper pixel sampling) although generally believed not to be doable, are in fact at hands, and with a cost that could be a fraction of a more complex 100m class telescope instrument.

6 Evaluation of the magnitude limits

In order to compute the expected limiting magnitudes for the near-IR camera (ONIRICA) we have assumed the following telescope and instrument parameters (see Table 2):

Mirror reflectivity	0.97
Number of reflections	6
Efficiency of the instrument	0.5
Detector efficiency	0.7
RON	1e
Dark	0e
Strehl	30%

Table 2: System Configuration

The AB photometric system is assumed (RD7)

$$K(AB) = -2.5\ \mathrm{Log}(f_\nu) - 48.60$$

where f_ν is the energy flux measured in erg cm^{-2} Hz^{-1}, (Note: 1 Jy = 10^{23} erg sec^{-1} cm^{-2} Hz^{-1})

For reference we report in Table 3 the conversion between AB Mag and Vega Mag.

band	wavelength	photon flux	energy flux	AB Mag	Vega Mag
	μm	$s^{-1}m^{-2}\mu m^{-1}$	μJy		
z	1.00	1000	66.3	19.3	18.7
J	1.25	1000	82.8	19.1	18.1
H	1.65	1000	109.3	18.8	17.4
K	2.20	1000	145.8	18.5	16.6

Table 3: Monochromatic flux conversions in the near infrared

The signal-to-noise ratio (S/N) for a point source is then given by the relation:

$$\frac{S}{N} = \frac{N_{Obj} \cdot \sqrt{N_{DIT}}}{\sqrt{N_{Obj} + 2 \cdot n_{bin} \cdot N_{Sky} + n_{bin} \cdot RON^2 + 2 \cdot n_{bin} \cdot DARK \cdot t_{\exp}}}$$

where N_{Obj} is the total number of counts per coming from the observed object, N_{Sky} is a similar term due to the sky, *RON* is the read out noise of the detector *DARK* is the similar term due to the dark counts, N_{DIT} is the number of individual expositions, $t_{\exp}$ the exposure time and n_{bin} the number of involved pixels.

6.1 Background emission (atmosphere and telescope)

Sky brightness (surface brightness: AB magnitude arcsec^{-2}) are given in Table 4.

Telescope	**J**	**H**	**K**
ELT ground based	17.5	16	15
JWST	22.6	22.8	23

Table 4: In this table are compared the sky brightness (surface brightness: AB magnitude arcsec^{-2}), for OWL-like ELT ground based telescopes and the JWST-like space telescopes.

Telescope and instrument background emission is not considered.

6.2 Magnitude limits for point sources

A point source is assumed to have a PSF with a radial brightness profile as shown in Figure 6. This is obtained by a combination of a Gaussians (to describe the core of the PSF) plus and exponential disk (to describe the wings). Based on the above parameters we have computed the magnitude limits as a function of the exposure time assuming the limiting magnitude is reached at S/N = 5.

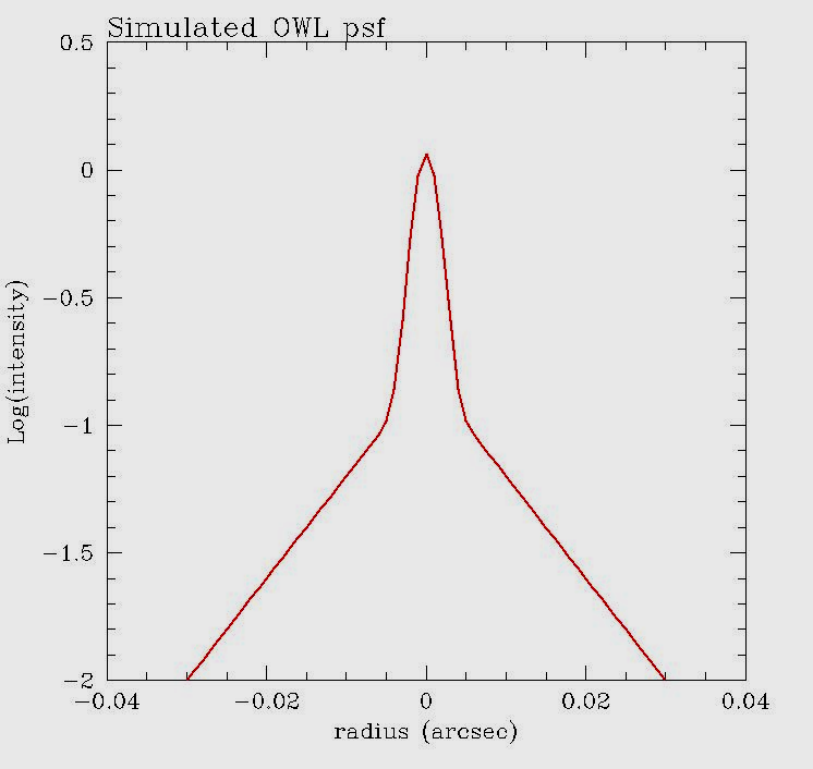

Figure 6: The simulated PSF radial intensity distribution of OWL. The *core* is represented by a Gaussian with FWHM ~ 0.005 arcsec plus an exponential disk to describe the *wings.*

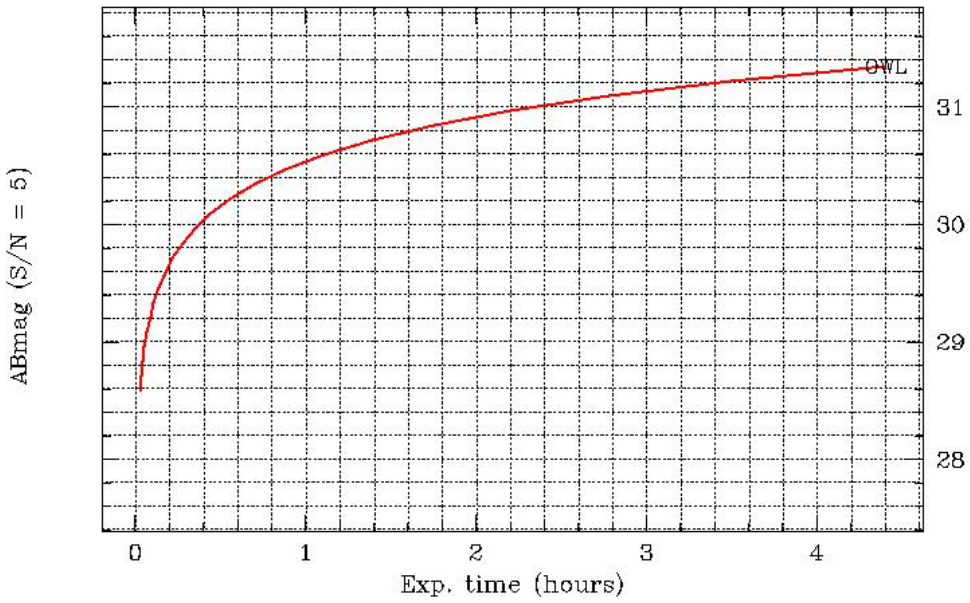

Figure 7: The magnitude AB(K) limit (S/N=5) for a point source as a function of the total integration time. Instrument specifications and parameters of the observation are given in Table 2, Table 3 and Table 4.

6.3 Magnitude limits for extended sources

The typical scale-length for distant galaxies is of the order of 0.1-0.2 arcsec. In order to evaluate the magnitude limits for extended objects (galaxies) we have assumed they have a scale-length of 0.1 arcsec and integrated the signal in an aperture of radius = 2×scale-length.

In Figure 8 we report the estimated magnitude limit assuming the parameters given in Table 2

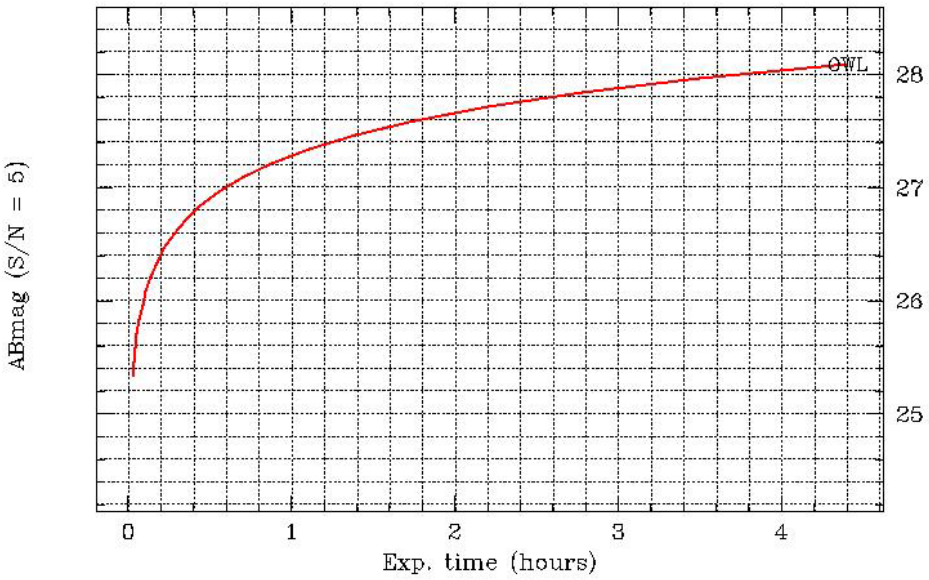

Figure 8: The magnitude AB(K) limit (S/N=5) for an extended source assuming an aperture of 0.2 arcsec radius as a function of the total integration time. Instrument specifications and parameters of the observation are given in Table 2, Table 3 and Table 4.

6.3.1 Simulation of point sources

We have used the Large Binocular Camera Image Simulator (LBCIMSIM) (RD8) to create simulated images of extended objects with the characteristics expected to be found at very high redshift. Observations on deep fields have shown that the size of galaxies, both spirals and ellipticals, decrease with increasing redshift and this effect can help to constrain galaxy formation and evolution models (e.g.RD9). We have thus simulated images of galaxies with 0.1" of half light radius: this is the lower value found in Hubble Ultra Deep Field and so it is expected to be a typical value at the redshifts that will be targeted by OWL and other future telescopes (RD10).

In Figure 9, Figure 10, Figure 11, Figure 12 we show the S/N curves we have obtained analyzing the simulated images with SExtractor software with the flux detected on an aperture of radius three times the half light radius. The images for the OWL ground telescopes have been convolved with a PSF given by a sum of two gaussians: 30% of the light is distributed on a Gaussian with FWHM=0.005, 0.0085, 0.017 arcsec respectively for the 100 meter, 60 meters and 30 meters cases and the remaining 70% on a Gaussian of FWHM= 0.5 arcsec. The images for the Next Generation Space Telescope are diffraction limited. In all cases we have considered the efficiency curves of a typical IR camera, optics, CCD and filters and sky brightness typical of ground-based or space-based observations.

We can see that at lower wavelengths a 100 meters adaptive optics telescope has better performances than a 6 meter space telescope (see Figure 14): for example the time needed to reach S/N=10 for a spiral object of AB magnitude 27 is about 0.3 hours in the J band. OWL 100m needs 3 hours to detect an object of AB Mag 27 in the K band and is considerably better than smaller ground based telescopes (Figure 10) while it

is less performing than a 6m space telescope because of the high sky brightness at 2μm caused by atmospheric emission.

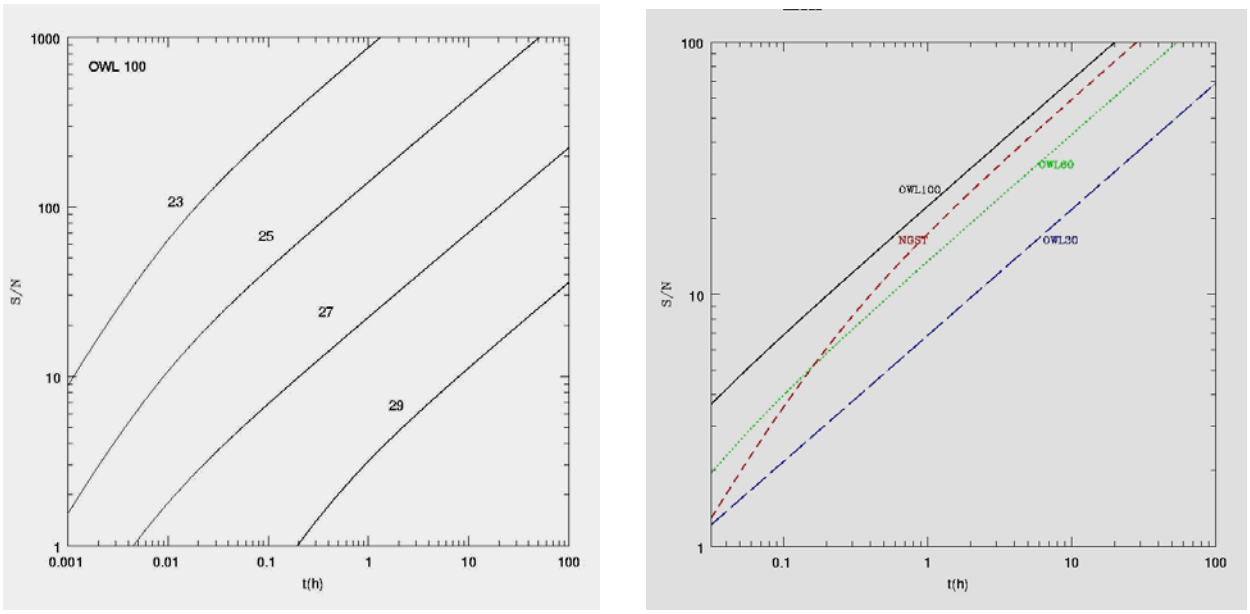

Figure 9 (Left): S/N vs. exposure time for spiral galaxies of different AB magnitudes in the J band observed with the OWL 100 meters telescope. (Right): the S/N curves for an object of AB magnitude 27 observed with OWL100m (continuous line), a 6 meter space telescope (short dashed), OWL60m (dotted line) and OWL30m (long dashed).

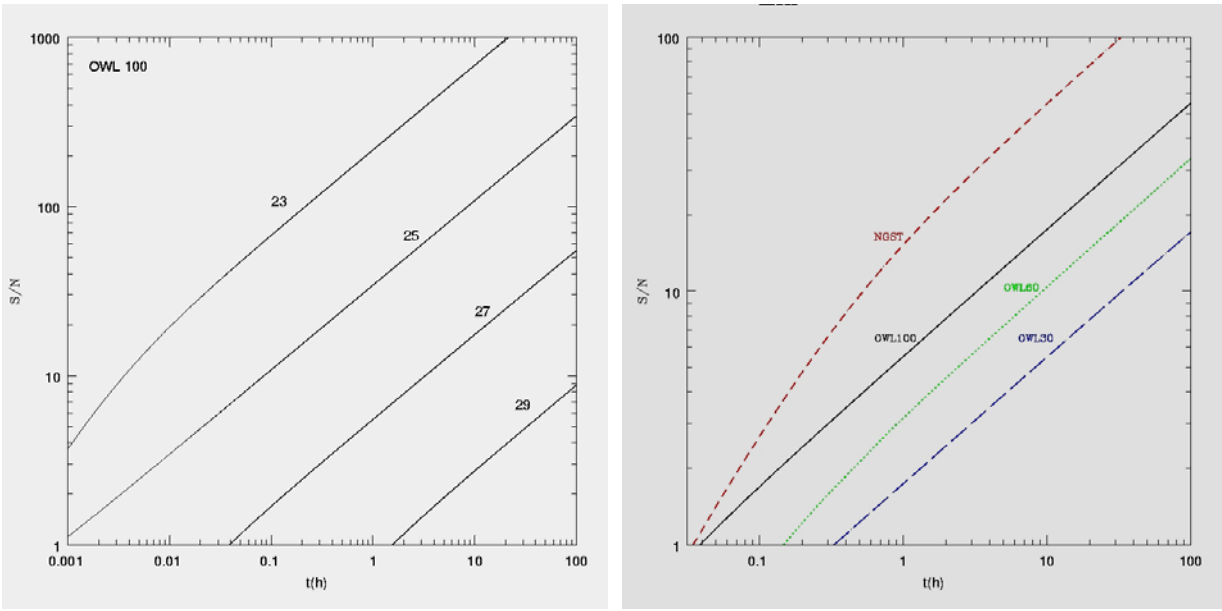

Figure 10: S/N vs. exposure time for spiral galaxies of different AB magnitudes in the K band observed with the OWL 100 meters telescope (up) and (down) the S/N curves for an object of AB magnitude 27 observed with OWL100m (continuous line), a 6 meter space telescope (short dashed), OWL60m (dotted line) and OWL30m (long dashed).

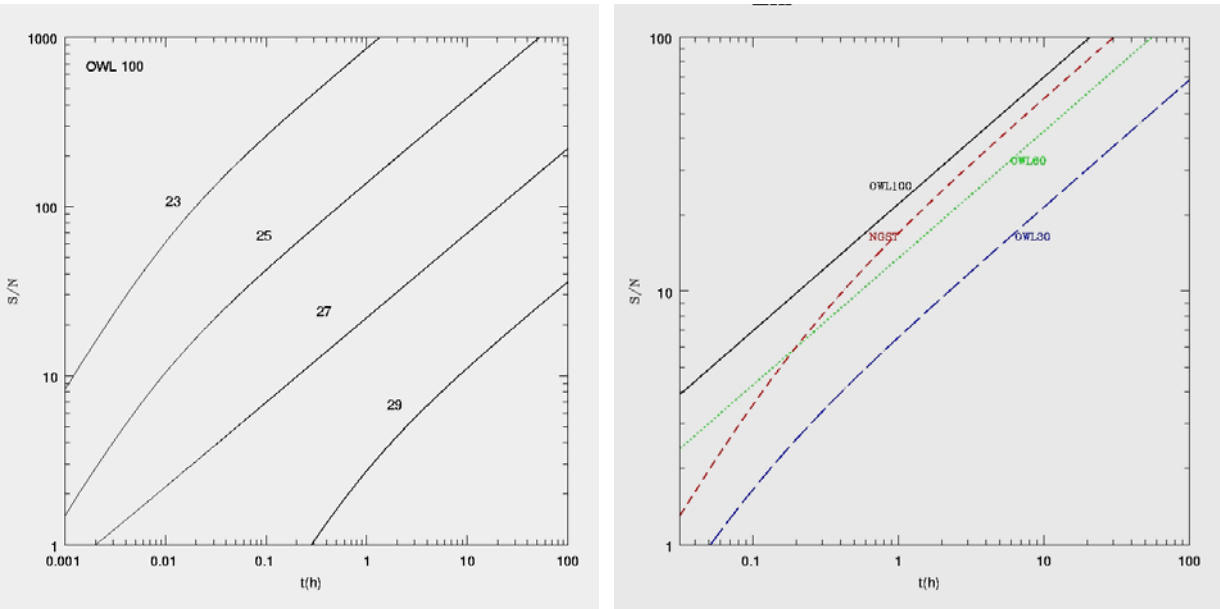

Figure 11: S/N vs. exposure time for elliptical galaxies of different AB magnitudes in the J band observed with the OWL 100 meters telescope (up) and (down) the S/N curves for an object of AB magnitude 27 observed with OWL100m (continuous line), a 6 meter space telescope (short dashed), OWL60m (dotted line) and OWL30m (long dashed)

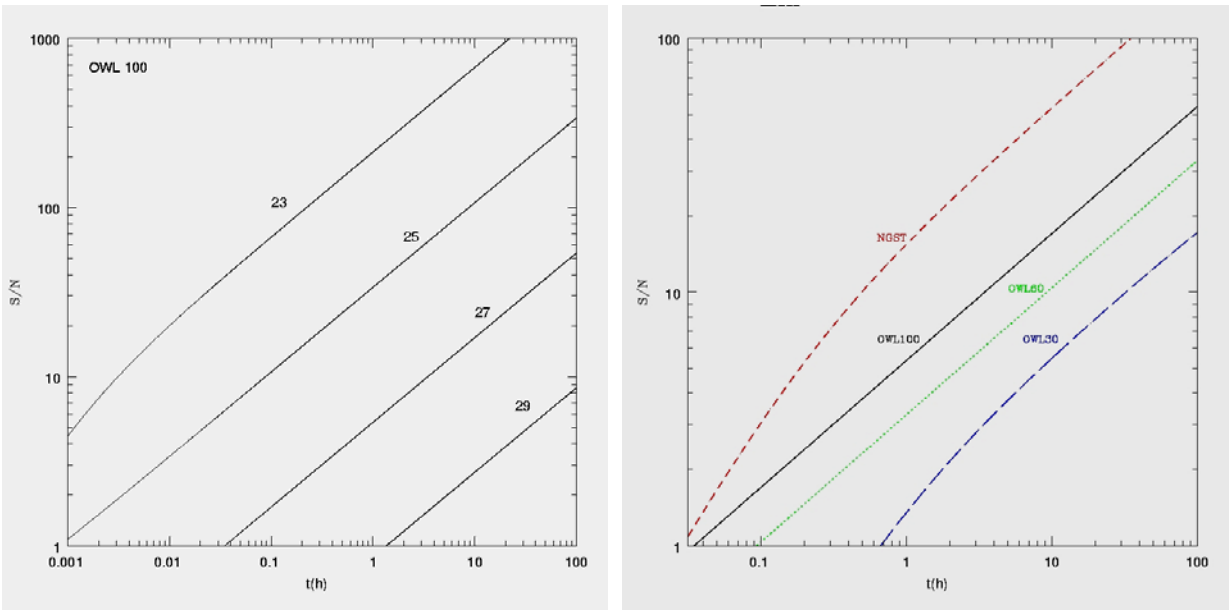

Figure 12: S/N vs. exposure time for elliptical galaxies of different AB magnitudes in the K band observed with the OWL 100 meters telescope (up) and (down) the S/N curves for an object of AB magnitude 27 observed with OWL100m (continuous line), a 6 meter space telescope (short dashed), OWL60m (dotted line) and OWL30m (long dashed).

6.4 Comparison 30m, 60m and 100m aperture ground based telescopes (AO diffraction limit)

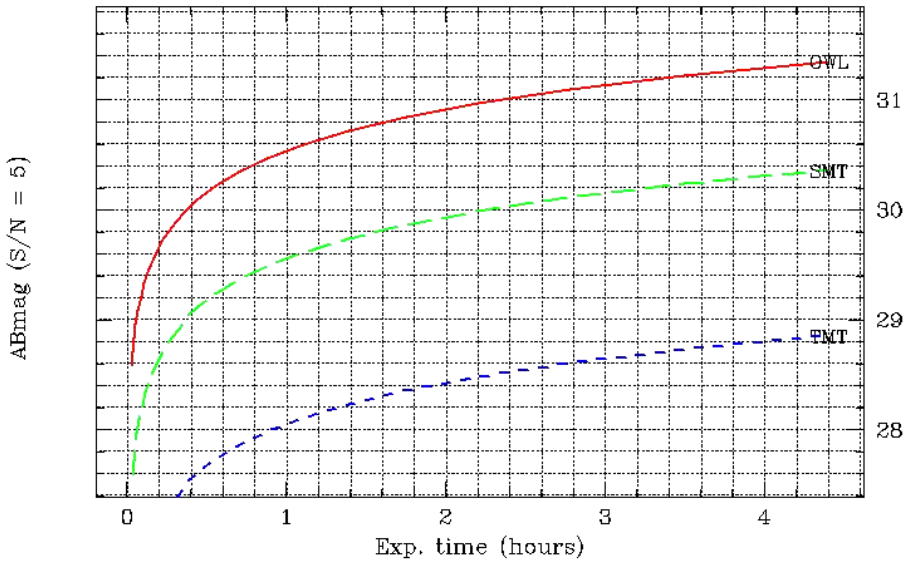

Figure 13: The limiting (S/N=5) magnitude $K_{(AB)}$ for point sources as a function of the exposure time. The ONIRICA case at the 100m (OWL) telescope is compared with the case of a 30m (TMT) and 60m (SMT) telescopes assuming the same efficiencies.

Telescope	Diameter M1 (m)	Mag lim (1 hour, S/N=5)
OWL	100	30.5
SMT	60	29.5
TMT	30	28.0

Table 5: Comparison of magnitude limits (S/N=5) for 1 hour integration time for 100m, 60m and 30m aperture telescopes.

6.5 Comparison between 100m and JWST (6m) telescopes

In Figure 14 and Figure 15 we show the comparison of the limiting magnitude for point source detection (S/N=5) using ONIRICA@OWL and JWST in the NIR bands J and K.

The parameters used for ONIRICA are given in Table 2. Background values used are reported in Table 4.

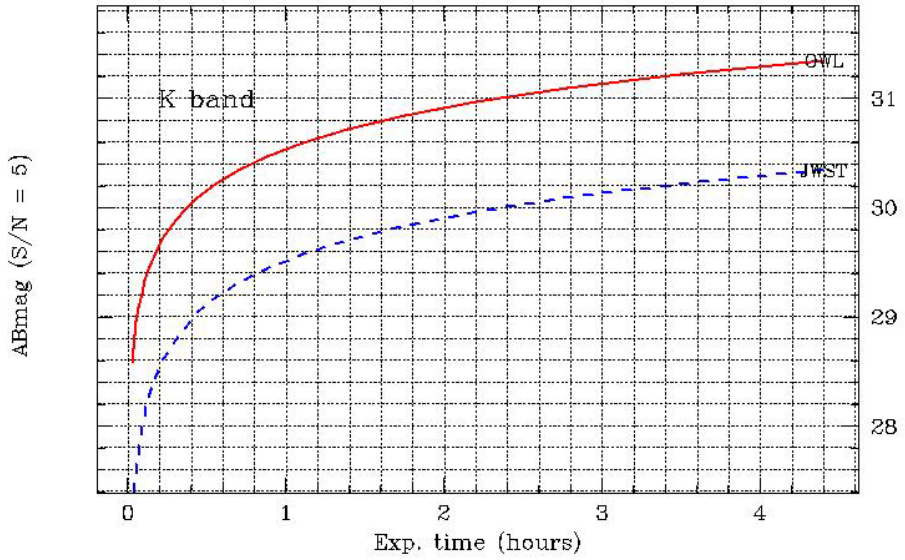

Figure 14: The limiting (S/N=5) magnitude K(AB) for point sources as a function of the exposure time. The case ONIRICA at the 100m (OWL) telescope is compared with the expected capabilities obtained with JWST.

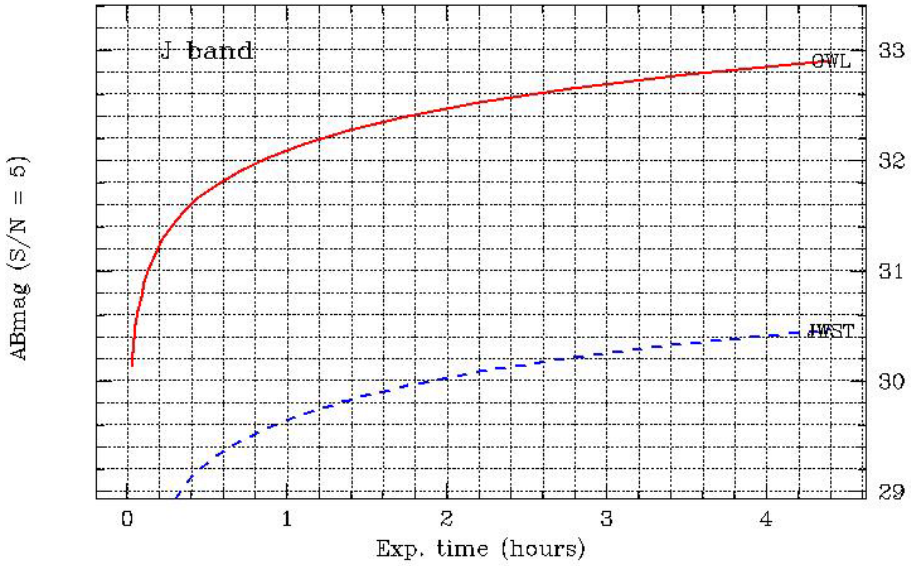

Figure 15: The limiting (S/N=5) magnitude J(AB) for point sources as a function of the exposure time. The ONIRICA case at the 100m (OWL) telescope is compared with the expected capabilities obtained with JWST.

Telescope	**Diameter M1 (m)**	**Mag lim (point sources) (1 hour, S/N=5)**
OWL	100	30.5
JWST	6	29.5

Table 6: Comparison of magnitude limit for ONIRICA@OWL and JWST.

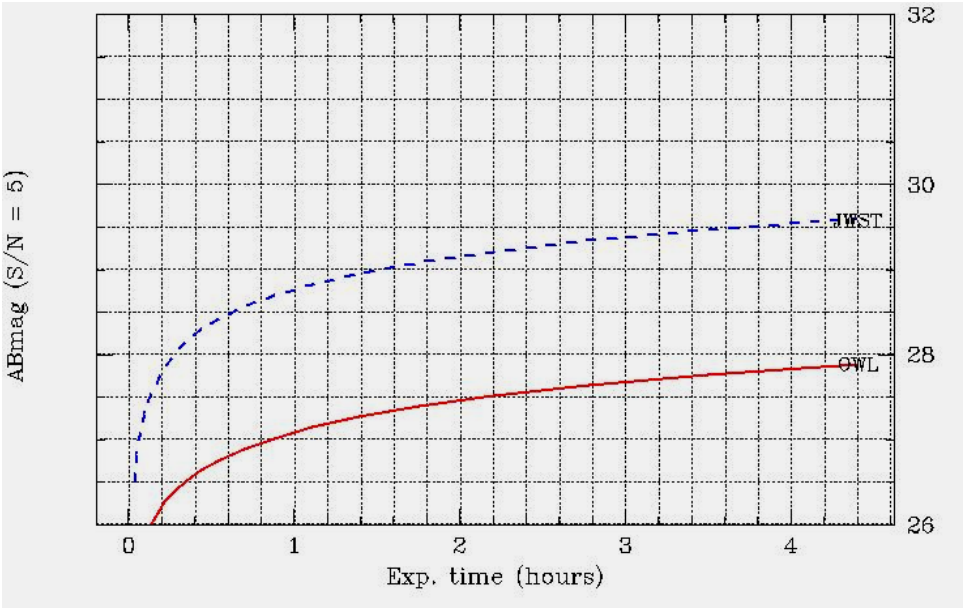

Figure 16: The limiting (S/N=5) magnitude K(AB) for extended sources (assumed scale-length 0.1 arcsec) as a function of the exposure time. The ONIRICA case at the 100m (OWL) telescope is compared with the expected capabilities obtained with JWST.

6.6 Simulated images and measurements

In order to create simulated images with ONIRICA we have used the Large Binocular Camera Image Simulator (LBCIMSIM), a program made to explore the performances of instruments at LBT but designed also to simulate observations with very different instruments (RD8). We created an image in the K band taking into account the instrumental characteristics of OWL (100 m diameter, 0.001"/pixel size and the efficiency curves of a typical IR camera, optics, CCD, filters). The total exposure time of the simulated image is 8×10^4 sec.

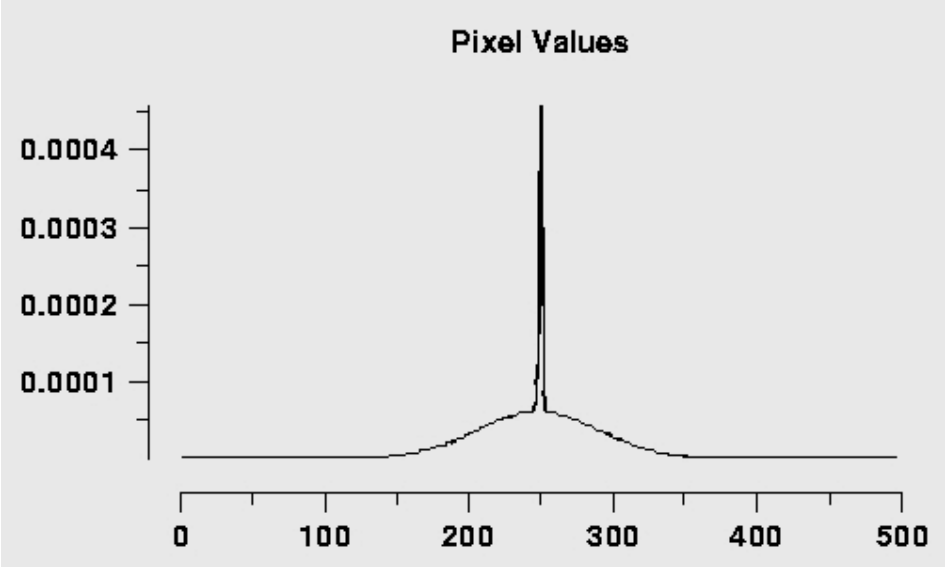

Figure 17: The PSF model used in the simulated images. It is done by the sum of two Gaussians: 30% of the light is distributed on a Gaussian with FWHM=0.005 arcsec and the remaining 70% on a Gaussian of FWHM= 0.5 arcsec.

The PSF is assumed as the sum of two Gaussians: one with FWHM=0.005 arcsec and containing 30% of the light and the remaining 70% on a Gaussian with FWHM= 0.5 arcsec.

In Figure 18 we show a field of 1"× 1". An enlarged section of this field 0.15"× 0.12" is shown in Figure 19. The field is uniformly populated with 5000 stars with AB magnitudes from 25 to 32. The luminosity function is a Salpeter one limited in absolute magnitude between -3 and 4. We have generated the catalogue of stars using IRAF routine STARLIST and then a synthetic FITS image without noise and sky background using IRAF routine MKOBJECTS.

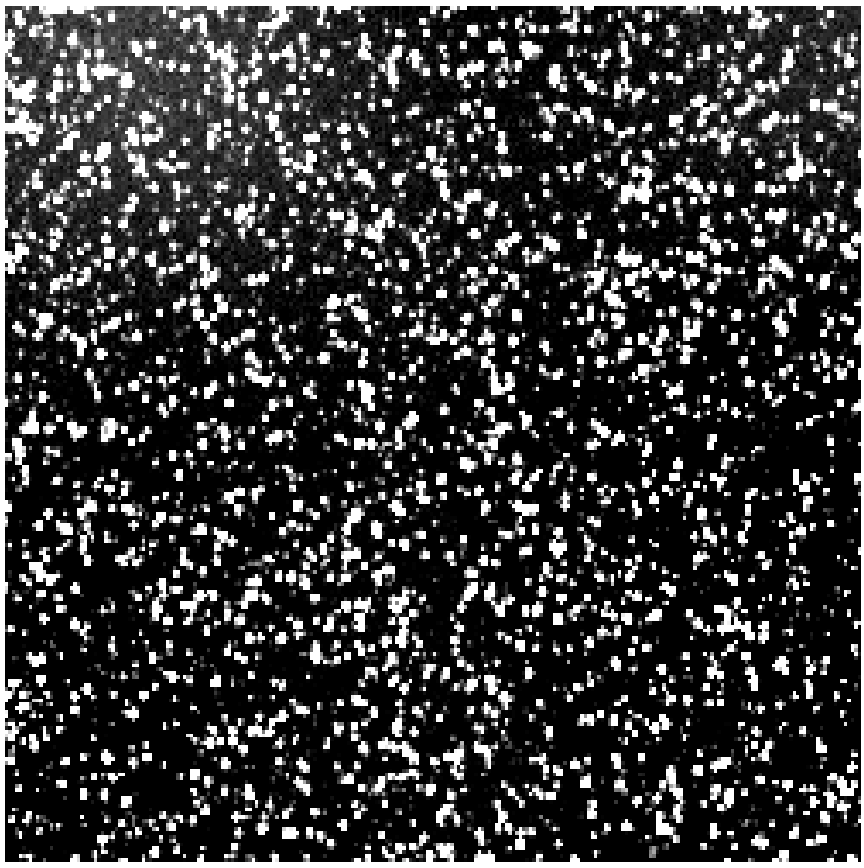

Figure 18: A section (about 1 arcsec FoV) of the simulated image. The field shown is populated with 5000 stars of $K_{(AB)}$ magnitude between 24 and 31 (assuming the luminosity function is a Salpeter limited in absolute magnitude between M_K -3 and +4).The image corresponds to an exposition of 8×10^4 seconds.

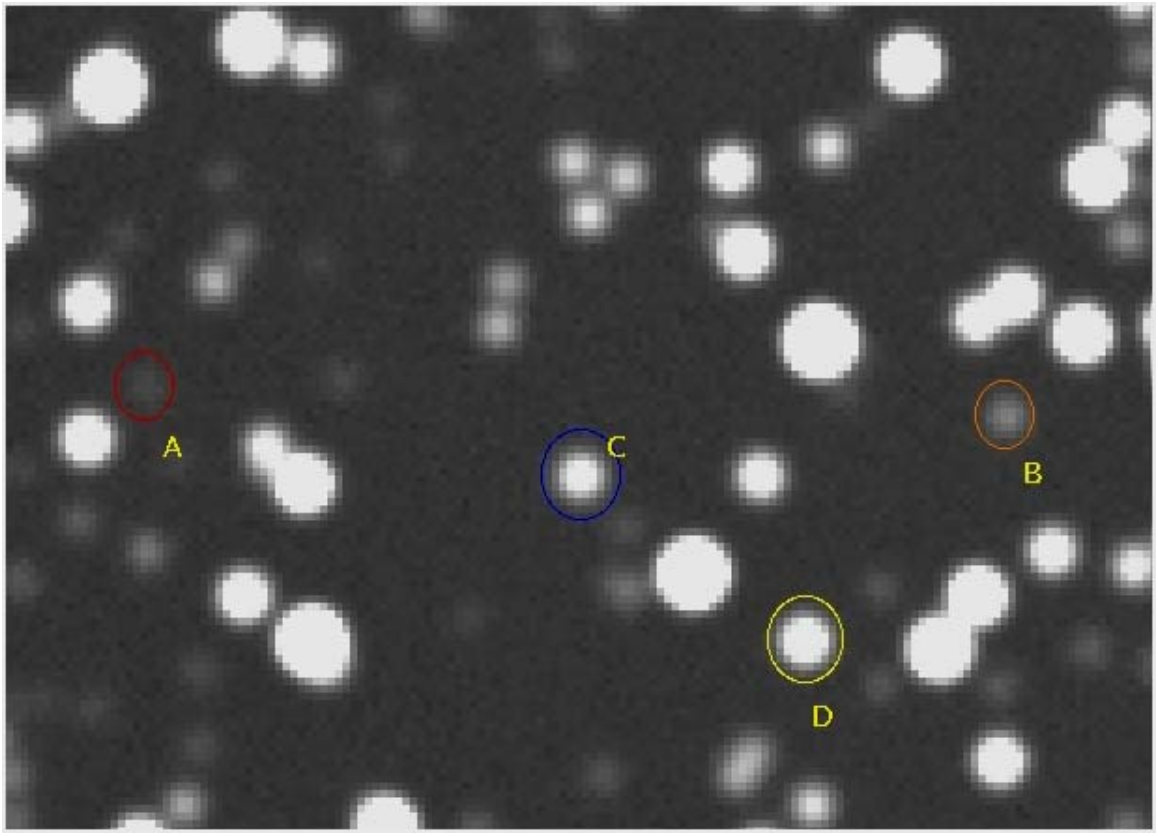

Figure 19: FoV = 0.15"× 0.12" The objects circled have been analysed using SExtractor (Bertin & Arnouts, 1996, A&AS 117, 393). They are: a) Star of K magnitude 30.51 (S/N=12). b) Star of K magnitude 29.18 detected with S/N=45. c) Star of K magnitude 27.74 detected with S/N=168. d) Star of K magnitude 27.22 detected with S/N=271.

6.7 Background in crowded fields

The evaluation of the magnitude limits given above refers to the cases when the background is dominated by the contribution of the sky (and telescope) emission. Because of the very large area covered by the *halo* of the image of an AO corrected point like source with respect to the area containing the *core* of the signal an additional source of background should be considered in the presence of dense fields. In this section we give an estimate of this possible contribution to the background in the case of crowded fields of unresolved objects.

For a 100m telescope the diffraction limit FWHM of a point source has dimension of about $\lambda / D \approx 2$ mas in the NIR-band. If we consider a $\lambda / r_0 \approx 1$" of seeing, the halo light of a star in a partially adaptively corrected image is spread in an enormous number of pixels, N. For instance assuming a pixel size equivalent to the size of the diffraction limited core, we have:

$$N = \left(\frac{D}{\lambda} \frac{\lambda}{r_0} \right)^2 \approx (1/0.002)^2 = 2.5 \times 10^5$$

At a given Strehl Ratio (SR) the average illumination per pixel in the corrected core (I_{core}) is given by:

$$I_{core} = I_{TOT} \times SR$$

The average intensity in a halo pixel (I_{halo}) is then:

$$I_{halo} = (1 - SR) \times \frac{I_{TOT}}{N}$$

Even for a SR = 0.01 the intensity ratio between the central core and the halo is (see also Figure 7):

$$\frac{I_{core}}{I_{halo}} = \frac{0.01 \times N}{0.99} \approx 2.5 \times 10^3$$

Thus, in contrast with the case of a 10m class telescope, the surface brightness of the halo is extremely small with respect to the core one. However, in the case of crowded fields the superposition of several of such faint halos can produce a significant contribution to the background.

Assuming the simple case of a field with a surface density of N* stars per sq. arcsec of magnitude K* then the average contribution of the background (I_{bkg}) due to the halo of the stars is given by the relation:

$$I_{bkg} = N^* \times I^* \times (1 - SR)$$

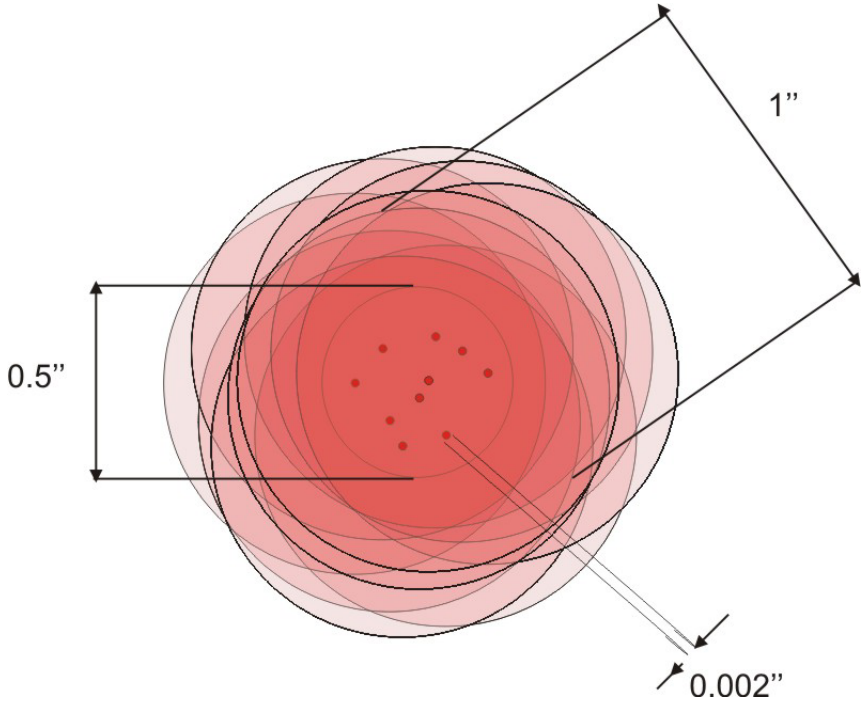

Figure 20: Crowded field of stars. Considering a 1” seeing diameter, the halo of all the stars inside a 0.5” region will be added to the noise. For this reason a crowded star field could affect the SNR in the case where the number of stars is comparable with the number of pixels over which the halo is spread.

In Figure 21 a comparison of I_{bkg} with the natural contribution from the sky is reported.

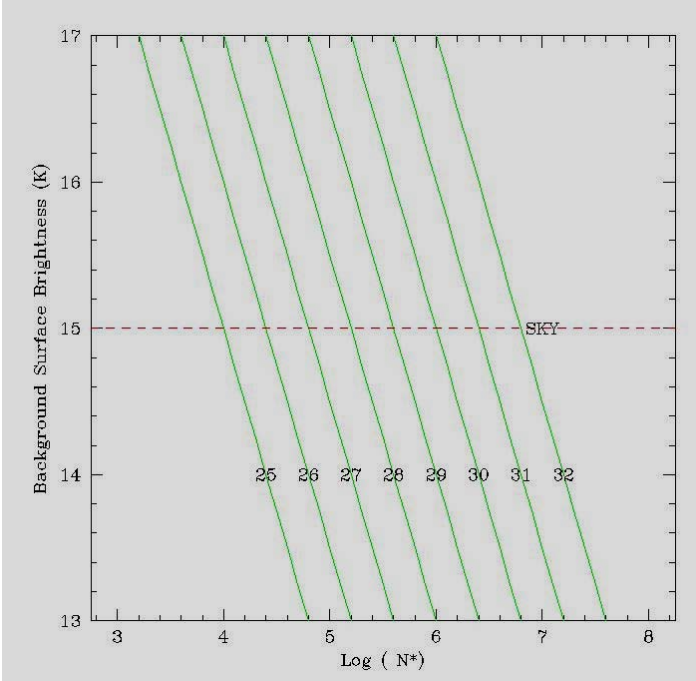

Figure 21: Comparison of the contribution of the background (I_{bkg}) due to the halo of stars in crowded field with the level of sky brightness. The surface density of the star is N* and the magnitude K*.

6.7.1 Example: Dense stellar field

Considering a very dense stellar field, for example an extragalactic globular cluster with a dimension smaller than the seeing halo diameter in which each star image core is affected by the speckle noise of all neighbour stars. In this example the density of stars at a given magnitude follows a Salpeter's like power law and the mass-luminosity ratio M/L is taken equal to 4. The distributions of the stars under these assumptions stars are shown in RD8 where different clusters, having an increasing number of stars, are taken into account.

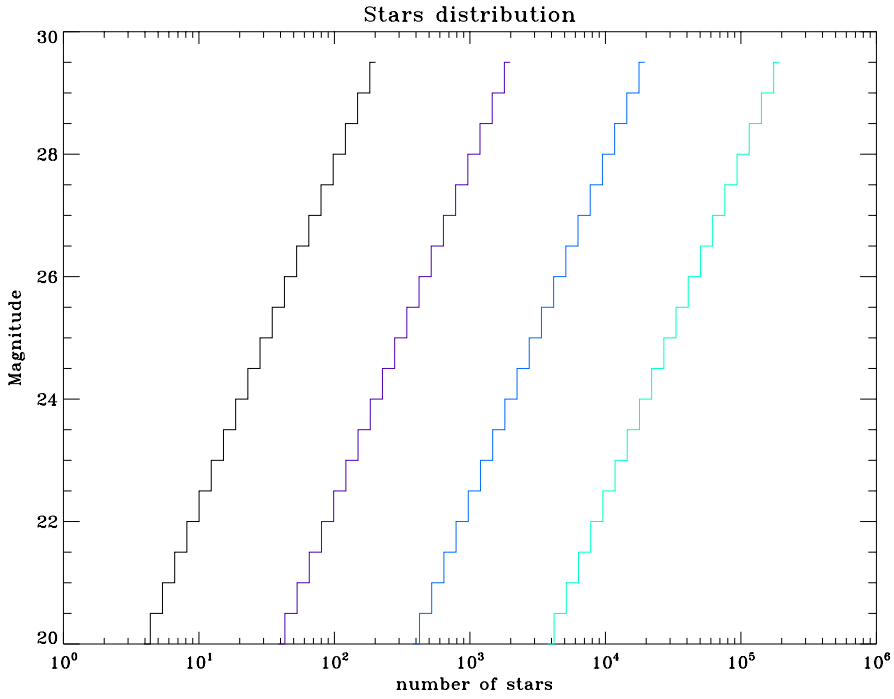

Figure 22: Number of stars respect to the magnitude in the simulated clusters of stars.

The Signal to Noise Ratio (SNR) of a single star light, without detector and other optical noise terms, is given by:

$$SNR = \frac{I_{core}}{\sqrt{I_{core} + I_{BKG} + I_{spk}}}$$

where the speckle noise is negligible with respect to the other noise contributions. The SNR of a single star acquisition in the crowded field changes to

$$SNR = \frac{I_{core}}{\sqrt{I_{core} + I_{BKG} + I_{SPK} + I_{CROW}}}$$

When the number of stars determines a total speckles noise comparable to the sky the SNR must take into account also this term. The total intensity of the speckle noise I_{SPK} is:

$$I_{SPK} = \sum_{i=1}^{n} I_{spk,i} = N \times \overline{I_{spk}}$$

where $\overline{I_{spk}}$ is the mean value of the speckle noise.

The crowding noise is instead formed by the fainter sources that occupy the same pixels of the measured star:

$$I_{CROW} = \frac{\sum_{i=1}^{n} I_{core,i} \times n_i}{N} \quad (mag_i > mag_*)$$

In the Figure 23 the comparison of the SNR values for the cases of a star acquisition in empty field and some crowded ones. It can be seen the crowding affects the limit magnitude value.

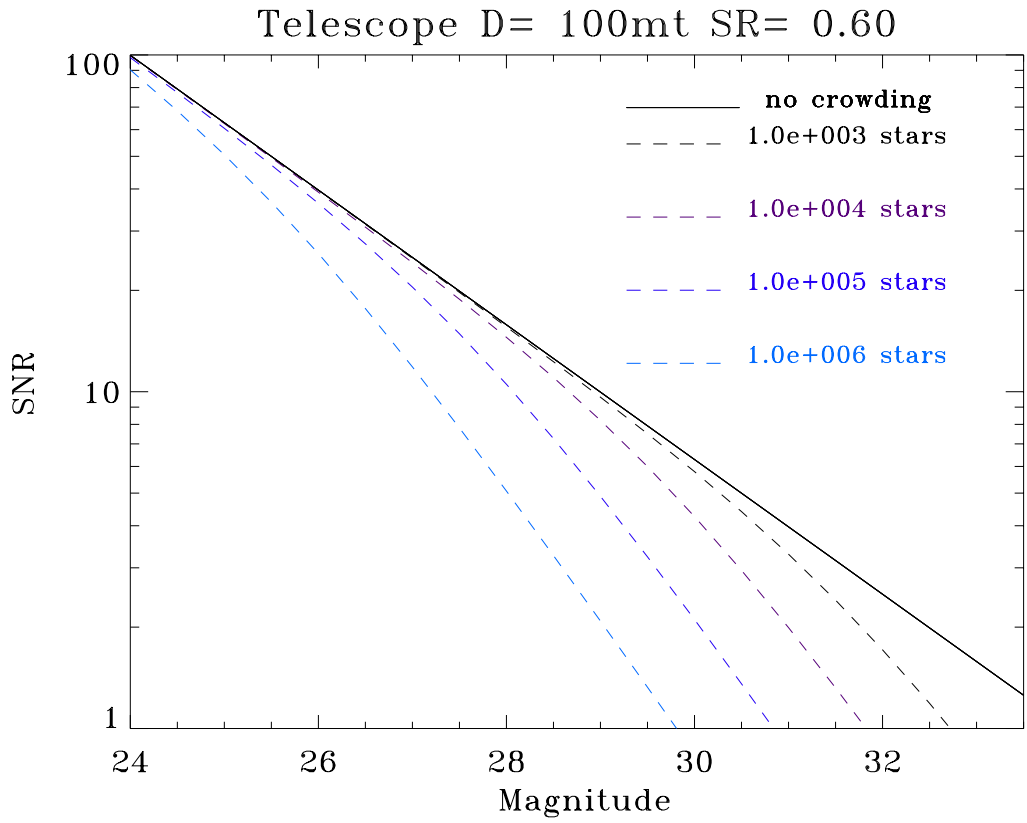

Figure 23: Comparison among the SNR of a star acquisition in a empty field (full line) and four differently crowded fields (dashed lines).

7 Key Science cases

In this section we report two science cases that would exploit the imaging capabilities of ONIRICA in terms of excellent spatial resolution and efficiency when applied to a 100m diameter telescope. These science cases are not intended to cover all possible science that can be investigate with a new generation imaging camera but to emphasize the applications in regimes that are not possible with the presently available telescopes and instrumentation. Most of the science cases discussed in this document are based mainly on observations that can be obtained with ONIRICA. Some of them will get further insight from other instrument complement foreseen for OWL. We also expect that all spectroscopic instruments designed for OWL will take advantages from the near-IR images collected by ONIRICA.

The first science case concerns the study of the stellar population of massive elliptical galaxies performed through the analysis of colour magnitude diagrams. The study in the near-IR is able to combine the superb imagining capabilities of the instrument (in term of resolution and sensitivity) with powerful tools to investigate star formation history of a galaxy from the detailed analysis of the properties of their stars. We show that under the designed instrument specifications (in terms of spatial resolution, efficiency and field of view) it will be possible to carry out a systematic study of stellar populations in galaxies well beyond those in the Local Group. With the expected capabilities it will be easy to *perform a systematic study of the stars in several galaxies in the Virgo cluster and to detect a significant fraction of stars in many galaxies of the more distant and richer Coma cluster.*

The second science case is intended to explore one of the hottest topics in the formation of the first objects and structure: the search for the first generation of stars (Population III). Since these objects are expected to exist at very high redshift ($z > 10$) this topic has been till now investigated only on the theoretical front. Direct detection of stars from the PopIII population could be possible under some conditions (e.g. as pair instability SN). The use of ONIRICA@OWL could provide one of the major results of the ELT adventure: *the detection of the shining of the first stars in the Universe.*

7.1 The stellar population of galaxies in clusters

One of the key issues in modern astronomy concerns the history of Star Formation in the Universe. Indeed, while the development of structures is well understood in terms of hierarchical growth in the framework of the (generally accepted) Cold Dark Matter model (e.g. Navarro, Frenk and White 1995), it is still not clear how to couple the baryonic component to the Dark Matter (DM) component, so as to explain the properties of the observed galaxies. In particular, the description of the processes of baryons collection within the DM potential wells, of the conversion of baryons into stars and the ensuing feed-back, of the Star Formation (SF) events triggered by merging of CDM haloes, is still prone to considerable uncertainty (e.g. Fontana, A. et al. 2004). A firm constraint to the prediction of models which couple the growth of DM haloes to the SF processes comes from the determination of the age distribution of the stars in galaxies. If we could derive a confident picture of how the SF proceeded within a large sample of galaxies through cosmic time we would get important clues on this issue.

For example, the analysis of the spectrophotometric properties of Cluster Galaxies has shown that, different from theoretical expectations, more massive elliptical galaxies host older stellar populations with respect to less massive ones (Kodama et. al. 2004; Treu, Ellis, Liao, and van Dokkum 2005). This fact promoted a revision of the treatment of SF and feedback in semi-analytic models of galaxy formation in a hierarchical universe, leading to a more satisfactory account of the predicted ages of stars in galaxies of different type (De Lucia et al., 2005).

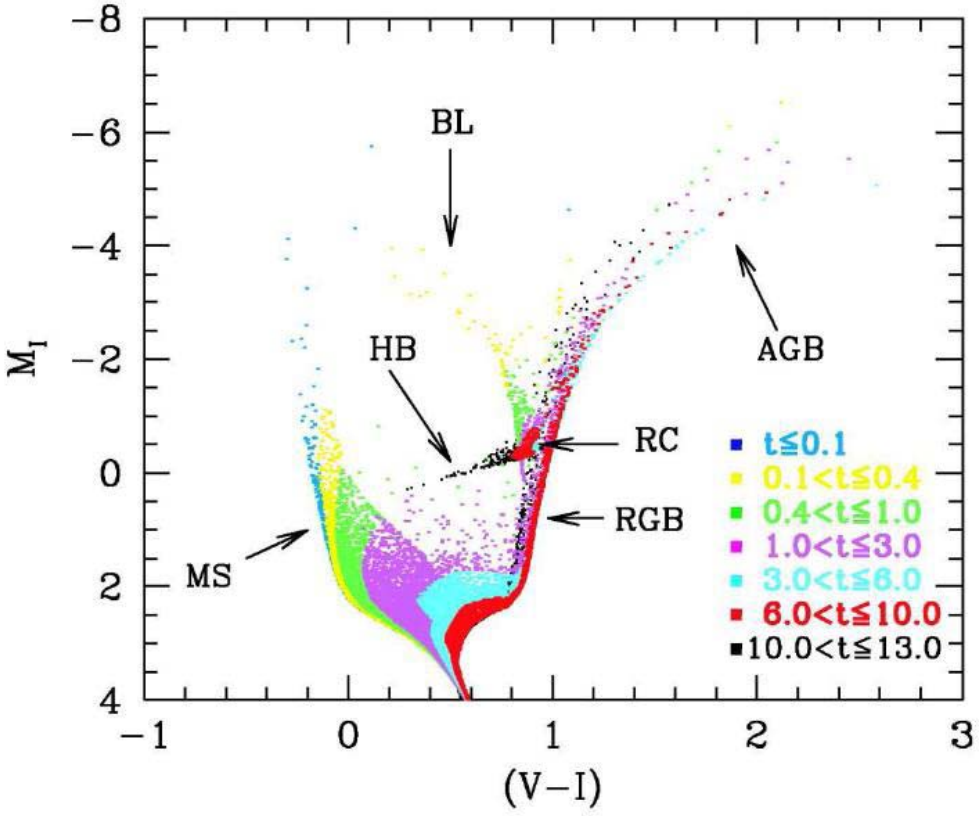

Figure 24: The optical colour - magnitude diagram (CMD) in M_I versus V-I with marked stellar populations of different ages. (From Aparicio & Gallart 2004)

The properties of the stellar populations in distant galaxies can be inferred only interpreting their integrated light. With this kind of studies, however, we can only derive the light averaged age and metallicity of the stars, and not the age distribution. A thorough determination of the SF history in galaxies can be done when the stellar population is resolved into individual stars.

Provided that we can measure the magnitude and colour of an individual star it is possible to accurately place it on a Hertzsprung - Russell diagram (or the observed version, the Colour-Magnitude Diagram). From the position on the H-R diagram an accurate age and thus a place in the evolutionary history of the galaxy (see Figure 24) can be obtained. By the simple counting of stars of different ages in a C-M diagram the rate at which stars are formed throughout time can be directly obtained.

7.1.1 The HR diagram in the JHK bands

The most direct way to derive the Star Formation History (SFH) of galaxies is through the interpretation of the observed Colour-Magnitude Diagram (CMD) of their resolved stars. In fact the analysis of CMDs (that reach at least the bright portion of the red giant branch, or the old Main Sequence turn-offs) yields information about stars born throughout the whole galaxy lifetime, and are indeed the fossil record of its SFH. It is worth to note that different regions of the CMD may sample stars of specific ages, so that from the simple stellar counts across the CMD it is possible to reconstruct the star formation history in the observed stellar population.

In the last decade this method has been successfully applied to a number of nearby galaxies, e.g. the dwarfs closest to the Milky Way (Carina, Sextans A and B, IC 1613, Fornax), Leo A, the halo population of M31 and of the elliptical galaxy Centaurus A, the Blue Compact Galaxies NGC 1569 and NGC 1705,

the dwarf galaxy IZ18, which, with a distance modulus close to 30 is one of the most distant objects analyzed so far (e.g. Skillman et al 2003; Annibali et al 2003; Brown et al 2003). Most of these studies have been conducted in optical bands, where the stellar colours are more sensitive to the effective temperatures, thereby allowing us to better separate the various evolutionary phases.

A few studies have also been performed in the near-IR, where the coolest stars appear bright and the effect of interstellar extinction is significantly smaller (e.g. Schulte-Ladbeck et al 2001; Ostlin et al 2005; Angeretti et al. 2005). In spite of the relatively short colour baseline, the NIR CMD allows us to sketch the SFH of a resolved galaxy by counting stars in specific regions.

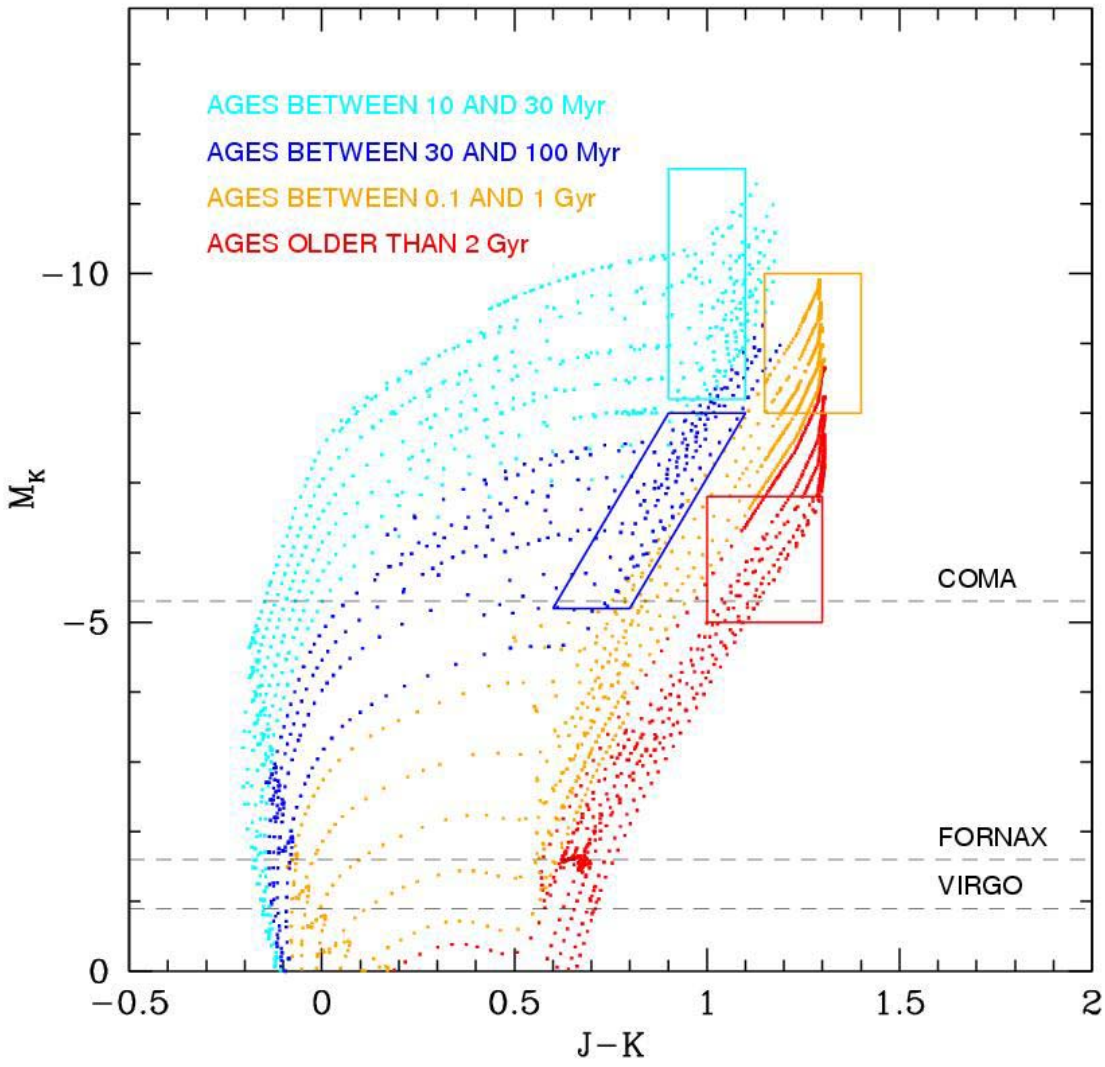

Figure 25: The NIR colour-magnitude diagram. Solar metallicity isochrones from Girardi et al. (2002, A&A 391, 195) in the Johnson, Cousins and Glass system. The colours encode the age range as labelled. The dashed lines show the level corresponding to a limiting magnitude of K=30 for objects in the Coma (mod=35.3), Fornax (mod=31.6) and Virgo (mod=30.9) clusters.

In Figure 25 we show theoretical isochrones from the Padova database in the J and K bands, for stars of solar metallicity. The boxes superimposed on the CMD have been chosen so as to sample different age ranges. Specifically: the bright cyan box samples the youngest stars, in the core Helium burning phase; the blue box is populated with older core Helium burners; the orange box samples bright, intermediate age AGB stars; and the red box targets the upper two magnitudes on the Red Giant Branch (RGB),

populated by stars with ages from 2 Gyr up to the oldest ages. The number of objects in these regions of the CMD is proportional to the mass that has been transformed into stars in the age range sampled by the specific region in the CMD:

$$\Delta N_j = M < \delta n_j > \quad (1)$$

where the $< \delta n_j >$ factors are the average of the specific production of stars in the CMD region *j* from stellar populations with ages such to produce stars in this CMD region. These factors are a robust prediction of the stellar evolution theory, having assumed an initial mass function.

Using this relation one can sketch the average SFH in a galaxy, or a portion of it. More sophisticated computations of synthetic CMDs help to work out more detailed information, and to test the SF modalities like bursting or constant SF rates, the IMF slope and the metallicity effect.

With the current instrumentation these studies are feasible in galaxies up to a distance of 4-5 Mpc (distance modulus ~ 28). With a 100m class telescope it would make them feasible for objects up to 100 Mpc, thus allowing us to reach the members of the nearest rich clusters and to derive the SFH of galaxies of all morphological types, including giant ellipticals, which are noticeably absent in the very nearby volume of the Universe. The horizontal dashed lines in Figure 25 show the magnitude levels corresponding to a limiting magnitude of K=30 for galaxies in the clusters of galaxies: Coma (d=100 Mpc), Fornax (d=21 Mpc) and Virgo (d=15 Mpc).

At 100 Mpc, a field of view of 1' across corresponds to a diameter of ~30 Kpc, comparable to the typical size of a massive galaxy. We would then derive the CMD of a substantial portion of one galaxy with two frames (one per photometric band).

7.1.2 The case study: simulated stellar populations

In order to test this idea we have considered as a case study the derivation of the SFH in galaxies members of a galaxy cluster. This would enable us to study the stellar populations along the entire Hubble Sequence, and to derive clues about the mass assembly history in galaxy clusters. In particular, we have performed simulations aimed at assessing the feasibility of the interpretation of the CMD of galaxies in Coma. We have generated synthetic CMDs with three kinds of SFHs, in order to describe the stellar content of galaxies of different morphological types, from late type spirals to ellipticals. The age distributions of the stars in these three cases are very different, and so is the appearance of the synthetic CMD.

The synthetic Colour-Magnitude diagrams have been calculated using the code ZVAR (Bertelli et al. 1992, Ng et al. 1995, Bertelli et al. 1995). In brief, Monte Carlo extractions of synthetic stars are performed to assign a value of mass, age and metallicity, following adopted functions for the IMF, SF rate and age-metallicity relation. Each synthetic star is placed on a theoretical (luminosity-effective temperature) HR diagram, via interpolation within a grid of stellar tracks. The point on the theoretical HRD is then converted into magnitude and colour using tables of bolometric corrections as function of gravity, temperature and metallicity. The input parameters are then the IMF, the SF rate and the age-metallicity relation. In our simulations we have adopted the Kroupa (2001) IMF which well represents the data for the Milky Way galaxy. The chosen SF rate and the age-metallicity relation are representative of late, intermediate and early type galaxies.

The interpretation of the simulated CMD in terms of SFH is performed using the relationship in equation (1), applied to the selected regions showed in Figure 25. In each box the ratio between the stellar counts and the mass of the parent stellar population is the weighted average of the specific productions, according to the age and metallicity distribution of the stellar population. When applying this method to a real galaxy such distribution is not known a priori; as a first approximation we consider the specific productions averaged over a flat distribution of age and metallicity

For each box we list in Table 7 the sampled age range and the average specific productions used in this exercise. Roughly, we expect to count 5 star in the faint red box per 10^5 M_{sun} of stellar population with age older than 2 Gyr; 2 stars in the bright red box per 10^5 M_{sun} of stellar population with age between 2 and 0.1 Gyr; 6 stars in the bright blue box per 10^5 M_{sun} of stellar population with age younger than 0.04 Gyr; 2 stars in the slanted box per 10^4 M_{sun} of stellar population with age between 0.03 and 0.15Gyr. The detailed description of the applied method is given in the Appendix 10.1.

BOX	AGE RANGE	$< \delta n_j >$	Notes
RSG: bright blue	From 0 to 0.04 Gyr	6×10^{-5}	Average around Z_{sun}
HeB: slanted	From 0.03 to 0.15 Gyr	1.7×10^{-4}	Average around Z_{sun}
AGB: bright red	From 0.1 to 2 Gyr	1.7×10^{-5}	Average over whole Z range
RGB: faint red	From 2 to 12 Gyr	5.4×10^{-5}	Average over whole Z range

Table 7: Average specific productions and sampled age ranges of the four diagnostic boxes (see Figure 25).

7.1.2.1 Young stellar population

For this case we have chosen a constant SF rate between 12 Gyr ago and now, coupled with an age-metallicity relation similar to the one observed for the solar neighbourhood (starting at Z=0.0001, the solar value of Z=0.019 is reached at 5 Gyr, while at 12 Gyr the total metallicity is Z=0.0235). The corresponding stellar population is characterized by a very wide range of ages and metallicities, with comparable contribution from all sub-populations.

The simulated CMD is shown Figure 26 with the colours encoding the age range of the different subpopulations. The stars younger than 6 Gyr are plotted in the left panel, and those older than that are plotted in the right panel so as to clearly picture the contributions of the different age bins. The total CMD corresponds to a total astrated mass of about 4×10^9 M_{sun}.

The four diagnostic boxes are over-plotted on the CMDs in Figure 26 most of the stars falling in the boxes belong to the age ranges reported in Table 7, although in the RGB box there is some contribution from stars younger than 2 Gyr, and in the HeB box we also count some very old stars. Table 8 shows the result of the application of the specific production method to the CMD in Figure 26. Specifically, the first column specifies the diagnostic box; the second column reports the probed age range, as in Table 7; the third column shows the number of stars of the simulation which fall in the box; the fourth column lists the corresponding mass of the stellar population, as derived by applying Eq. (1) with the specific productions in Table 7; the fifth column shows the average star formation rate obtained dividing the derived mass by the probed age range.

BOX	AGE RANGE	ΔN_j	ΔM [M_{sun}]	$\langle dM/dt \rangle$ [M_{sun}/yr]
RSG: bright blue	0 to 0.04 Gyr	1054	1.8×10^7	0.44
HeB: slanted	0.03 to 0.15 Gyr	9937	6×10^7	0.50
AGB: bright red	0.1 to 2 Gyr	8535	4.9×10^8	0.26
RGB: faint red	2 to 12 Gyr	259049	4.7×10^9	0.47

Table 8: Results of the application of the specific production method to the synthetic CMD in Figure 26.

Although we do not recover the exact shape of the SFR adopted for this simulation, i.e. a constant value throughout the whole age range, the average SFR estimated with the specific production method does not show large variations in the four bins. Indeed, it results constant within a factor of 2. By integrating the derived SFR we obtain a total astrated mass of 5.2×10^9 M_{sun}: compared to the total astrated mass of the simulation, we conclude that, in this case of young stellar populations, the specific production method leads to overestimate the total mass by approximately 30%. Both the shape of the SFR and the level seem thus well recovered.

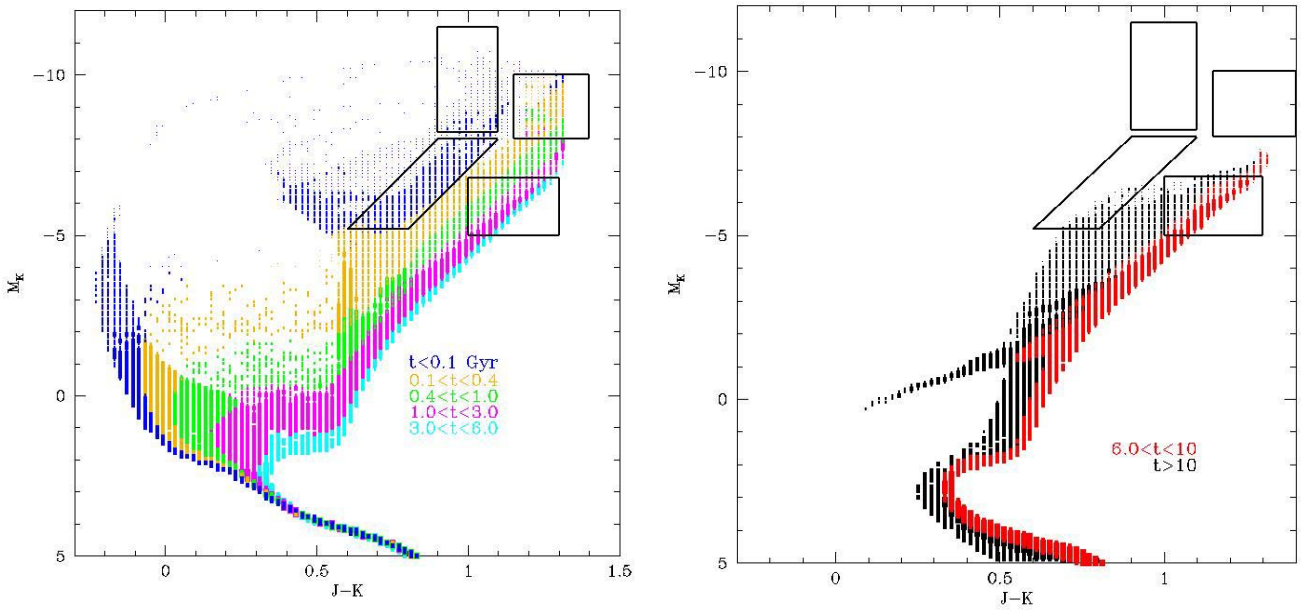

Figure 26: The CMD for a *young* stellar population. Left: objects with age <6 Gyr. Right: objects with age > 6 Gyr.

7.1.2.2 Intermediate age stellar population

Figure 27 shows the synthetic CMD obtained with an exponentially declining SF rate with an e-folding time of 5 Gyr, coupled with a metal enrichment law similar to the previous case (i.e. starting at Z=0.0001, the solar value of Z=0.019 is reached at 5 Gyr, while at 12 Gyr the total metallicity is Z=0.035).

Compared to the CMD in Figure 26, the younger component of the stellar population indeed appears much less prominent since in this case most of the star formation occurs within the first 5 Gyr. Table 9 reports the result of the application of the specific production method to this case. The various entries in the table are the same as in Table 8, with the additional column labelled ΔM_{AST} reporting the actual mass astrated in the simulation within the specific age interval.

BOX	AGE RANGE	ΔN_j	ΔM [M_{sun}]	ΔM_{AST} [M_{sun}]	$\langle dM/dt \rangle$ [M_{sun}/yr]
RSG: bright blue	0 to 0.04 Gyr	21	3.5×10^5	3.6×10^5	0.009
HeB: slanted	0.03 to 0.15 Gyr	746	4.5×10^6	1.1×10^6	0.04
AGB: bright red	0.1 to 2 Gyr	225	1.3×10^7	2.1×10^7	0.007
RGB: faint red	2 to 12 Gyr	22916	4.2×10^8	4.3×10^8	0.04

Table 9: Results from the application of the specific production method to the synthetic CMD shown in Figure 27.

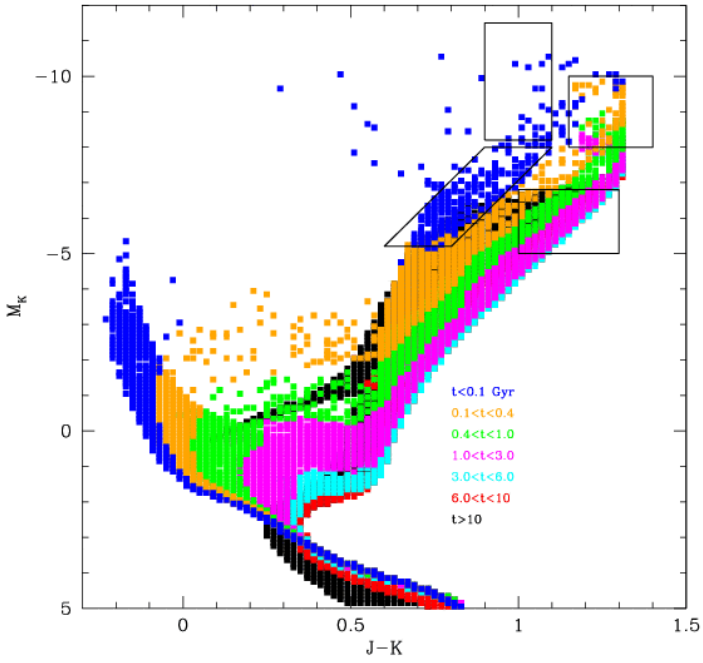

Figure 27: The CMD for a composite stellar population with most of its mass in relatively old stars. A total astrated mass of 4.5×10^8 M_{sun}. The colours encode the age of the synthetic stars as labelled. The four diagnostic boxes are superimposed.

The largest discrepancy between the predicted mass ΔM and the astrated mass occurs for the age range probed by the slanted box. Part of the discrepancy is due to the contribution in this box by very metal poor, old stars on their RGB phase. These objects are erroneously counted as HeB stars, mimicking a higher level of SF rate in the age interval which is assumed to be probed by this box. An additional factor leading to an overestimate of the SF activity in this age range is related to the dependence on the metallicity of the specific production. As specified in Table 7, the average specific production adopted for this box is appropriate for solar metallicity. However, in this particular simulation, stars younger than 5 Gyr have a metallicity well above solar, so that a higher specific production would be more appropriate

(see Appendix). Similarly, the discrepancy between the estimated and actually astrated mass in the AGB box is due to having adopted a specific production larger than what appropriate for super solar metallicity stars. These discrepancies illustrate an intrinsic limitation of the method, which results from the fact that stars with different metallicities and different evolutionary phases can fall on the same region of the Colour-Magnitude diagram. A much better description of the SF history would be achievable with information on the metallicity of the stars.

7.1.2.3 Old stellar population (early type galaxies)

The last case considered consists in a simulation that adopts a single episode of SF started 12 Gyr ago and lasted for 2 Gyr at a constant rate. The metal enrichment law adopted for this case assumes a very rapid rise of the metallicity from Z=0.0001 to Z=0.05 within 2 Gyr. The corresponding CMD is shown in Figure 28; clearly only old stars populate this diagram, with the bright red and the bright blue boxes completely empty of objects. The total mass astrated in this simulation is of 4.9×10^8 M_{sun}; since we count 22711 stars in the RGB box, with the specific production method we infer a mass of $4.2 \times 10^8 M_{sun}$ in stars with ages older than 2 Gyr.

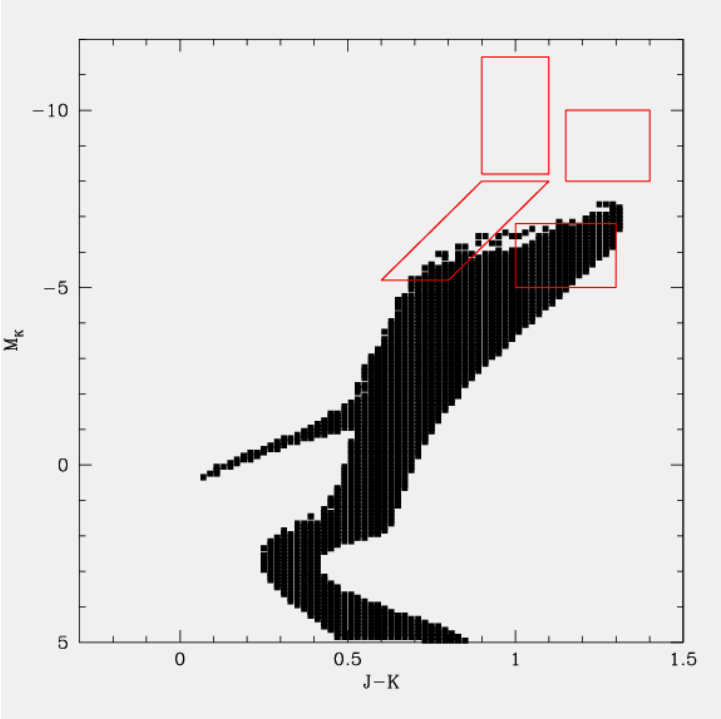

Figure 28: The CMD for an old (>10 Gyr) stellar population with the four diagnostic boxes superimposed.

Thus the specific production method tends to underestimate the stellar mass by 15%. Actually the RGB diagnostic box does not sample the low metallicity component of the stellar population which is distributed at bluer colours. On the other hand, if the observed CMD only shows an old stellar component, like in this case, the RGB box can be easily re-designed to include the wide RGB which reflects a wide metallicity spread.

7.1.3 Simulated K band images of the galaxies in Virgo, Fornax, Coma (crowding, detection limits and photometry)

Having assessed the capability of using CMD to reconstruct the SF history of galaxies of different types, we pass now to examine up to which distance the method can be applied. The diagnostic boxes have been chosen as bright as possible, in order to maximize the distance at which this kind of study can be done. We need now to test the possibility of obtaining stellar photometry for the objects falling in the 4 selected boxes.

In Table 10 we report the main properties of a number of representative nearby galaxies and group or clusters of galaxies. While the stellar content of the nearest objects can be (and are) observed by present generation of telescope and instruments, the most distant are not feasible. For this exercise we consider in detail the case of galaxies in the Coma cluster.

Object	$(m-M)_0$	θ(1 pc)	Ra(J2000)	Dec
LMC	18.5	4"	05 23	–69 45
M31	24.3	0.3"	00 43	+41 16
Sculptor Group	26.5	0.11"	00 23	–38 00
M81/82	27.8	0.06"	09 55	+69 40
Cen A	28.5	0.04"	13 25	–43 00
NGC3115	30.2	0.02"	10 05	–07 42
Virgo Cluster	30.9	14 mas	12 26	+12 43
Antennae Galaxy	31.5	10 mas	12 00	–18 53
50Mpc	33.5	4 mas	…	…
Arp220	34.5	2 mas	15 34	+23 30
Perseus Cluster	34.5	2 mas	03 18	+41 31
Stephan's Quintet	35.0	2 mas	22 36	+33 57
Coma Cluster	35.0	2 mas	13 00	+28 00
Redshift z~0.1	38.5	…		…
Redshift z~0.3	41	…		…

Table 10: The nearby galaxies and group, or clusters, of galaxies.

Coma cluster

The Coma Cluster (see Figure 29 and Figure 30) is an ideal subject for observation. Less than five percent of Abell clusters contain as many galaxies as Coma does, and none are as close to the MW. Because Coma is not obscured by the dust clouds of the Milky Way, it can be seen without interference.

We have considered a massive (10^{11} Msun) elliptical galaxy (Re=10 Kpc) at the distance of the Coma cluster (see example in Figure 30). Assuming its brightness profile is described by a de Vaucoulers law it has an effective radius of 25 arcsec. We have simulated the density of stars in a field of 1 arcsec squared at the angular distance of 20 arcsec from the center of the galaxy. See also enlarged view (white box) given in Figure 30.

Here the sampled luminosity (in 1 $arcsec^2$) is about 10^{-4} that of the whole galaxy. Assuming the stars follow the luminosity function given in Figure 32 we find in this location there should be on average $7x10^3$ stars per $arcsec^{-2}$ with $M_K < -4$. This remains valid also if a LF of a purely old stellar population is assumed since the contribution of luminous stars is negligible in the very small FoV shown. The stars fainter than M_K=-4 will be mostly unresolved and will contribute to the background light of the image. In this case the additional background, due to the unresolved objects, corresponds to half the total light from the stars observed in the frame. These simulations indicate that the proposed observation is feasible under the conditions described above.

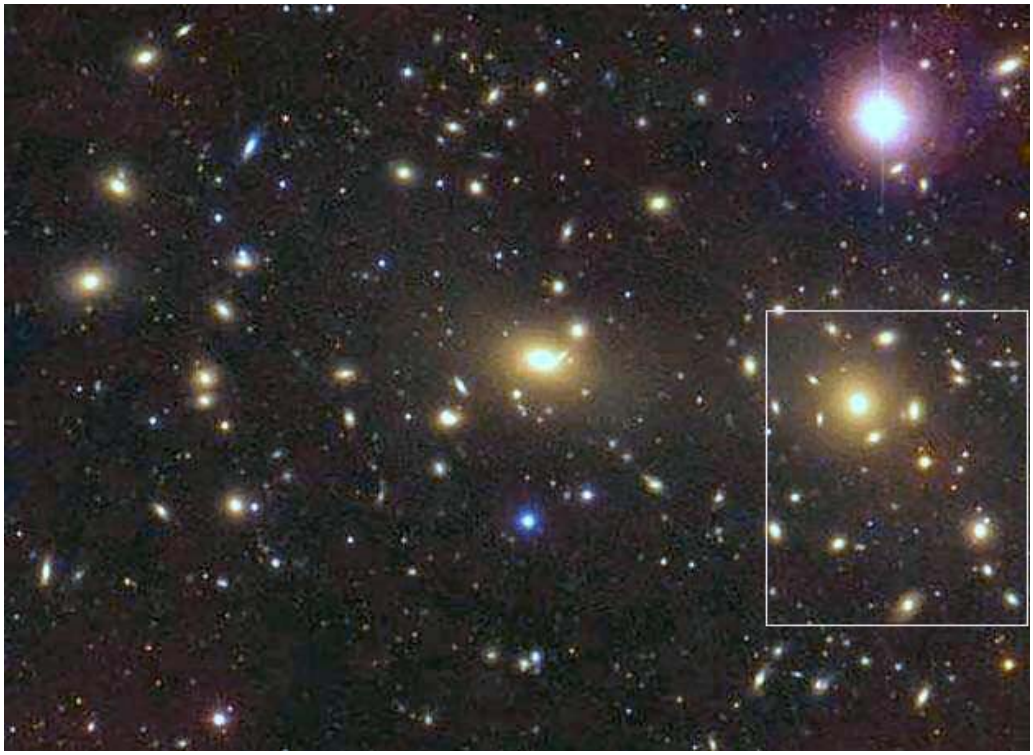

Figure 29: A colour picture of the Coma cluster of galaxies.

Figure 30: A region in the Coma cluster of galaxies (left), and an enlargement of the white box with example of a massive galaxy in the Coma cluster (right).

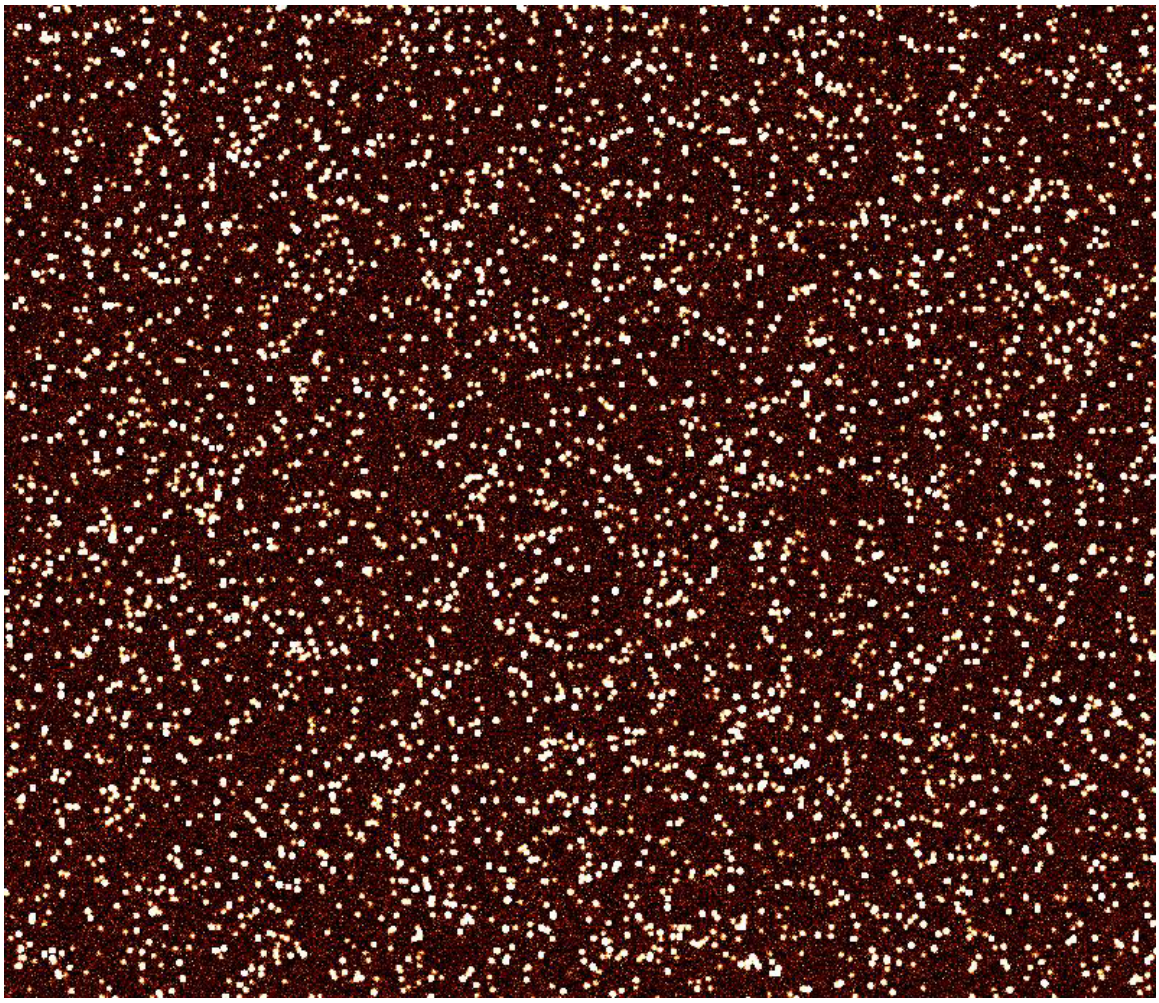

Figure 31: Simulated image: FoV 1 arcsec; 7700 stars with $M_K < -4$ following the LF of objects given in Figure 32. The background level includes the light from unresolved stars ($M_K > -4$).

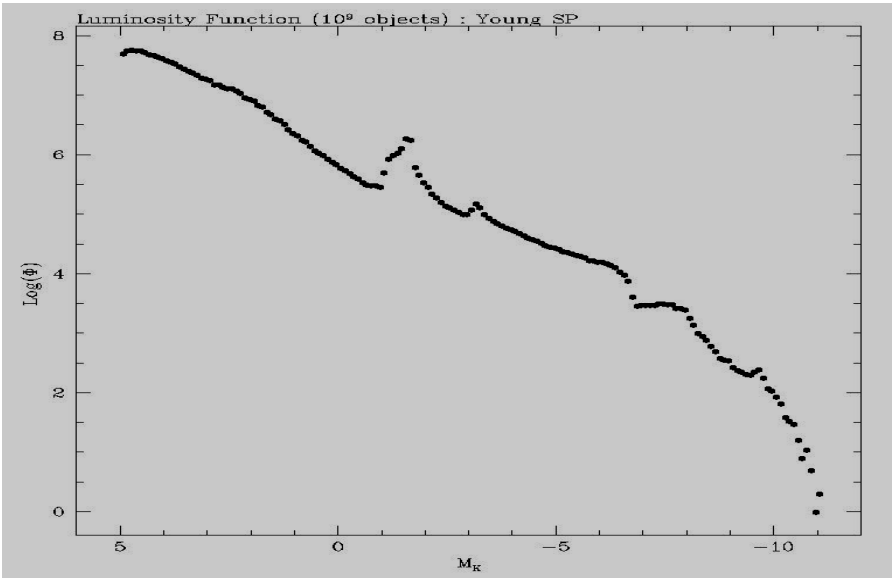

Figure 32: The integrated Luminosity Function for the *young* stellar population (10^9 stars).

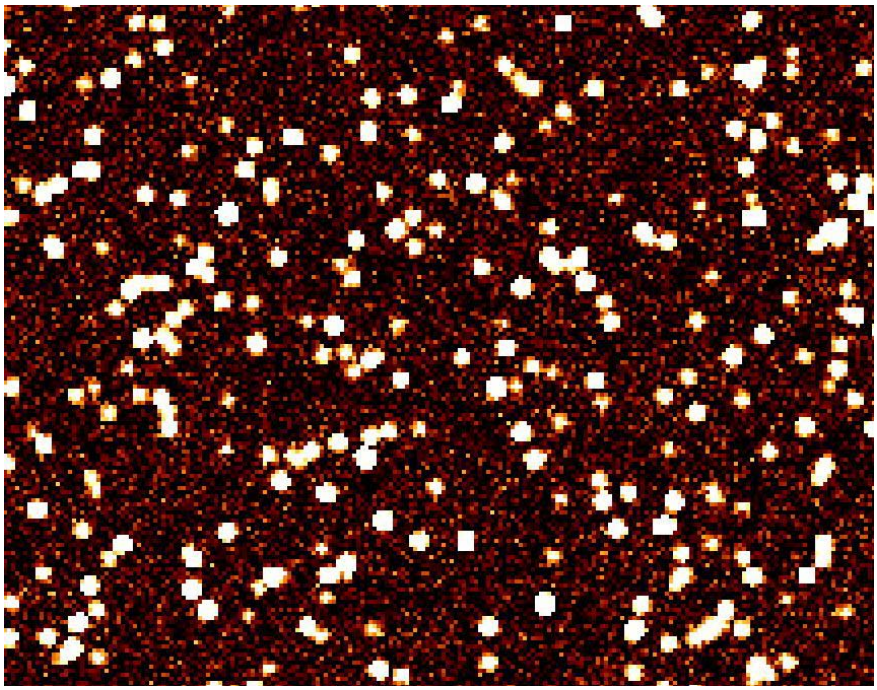

Figure 33: Enlarged section of the simulated image shown in Figure 31

References

- Annibali, F., Greggio, L., Tosi, M., Aloisi, A., & Leitherer, C. 2003, AJ, 126, 2752
- Angeretti, L., Tosi, M., Greggio, L., et al. 2005, AJ 129
- Aparicio, A. and Gallart, C, 2004, AJ, 128 1465
- Bertelli,G.,Mateo, M., Chiosi,C., Bressan, A.1992, ApJ,388,400
- Bertelli, G, Bressan A, Chiosi C. Ng Y. Ortonali S. 1995 A&A 301 381
- Brown, T.M., Ferguson, H.C., Smith, E., et al. 2003, ApJ 592, L17
- De Lucia et al G., Sprinkel, V., White, S.D.M., Croton, D., Kauffman, G. 2005, MNRAS, submitted, astro-ph/0509725
- Fontana, A. et al. 2004, A&A 424, 23
- Kodama,T. et. al. 2004, MNRAS 350, 1005
- Kroupa, P. 2001 MNRAS 322, 231
- Navarro, J.F., Frenk, C.S., White, S.D.M. 1995, MNRAS 275, 56
- Ng,Y.,Bertelli,G.,Bressan, A., Chiosi, C.,Lub,J.,1995, A&A,295,655
- Ostlin, G., & Mouhcine, M. 2005, AA 433, 7970;
- Schulte-Ladbeck, R.E., Hopp, U., Greggio, L., et al 2001, ApJ 121, 3007;
- Skillman, E.D., Tolstoy, E., Cole, A.A., et al. 2003, ApJ 596, 253;
- Treu, T., Ellis, R.S.,Liao, T.X., van Dokkum, P.G. 2005, ApJ 622, L5

7.2 "Fiat lux:" hunting for Pop III stars

7.2.1 Introduction: first lights in the primordial Universe

Why is the quest for first light important? There are now overwhelming evidences that we live in a hierarchical Universe: the analysis of the CMB anisotropies, combined with the SDSS and 2dF survey data, the study of high redshift supernovae and galaxy clusters all converge to indicate that we live in a critical universe dominated by a cosmological constant (i.e. such that $\Omega_\Lambda = 0.73 \pm 0.04$) and by weakly interacting dark matter particles with a small fraction of baryons (such that $\Omega_M = 0.27 \pm 0.04$ and $\Omega_b =$

0.044 ± 0.04). In such a universe the formation of structures is hierarchical, i.e. follows a bottom-up sequence, where small objects are formed first, and thereafter grow by merging events. The first objects that can host star formation are dark matter minihalos of masses 10^6 M_{sun}, which will later continue to accrete gas and/or merge to build up present-day galaxies. In such mini-halos the first sources of light form out of an unmagnetized gas of primordial composition, i.e. composed only of the light elements (H, D, He, Li). This first generation of stars emerging from the "dark ages" are called Pop III stars.

Unfortunately, this scenario is so far entirely speculative, since all the searches for galaxies at the highest redshifts have so far detected only relatively mature systems, where metal enrichment has already proceeded for a significant time. The direct detection of a genuine PopIII population would therefore be a fundamental milestone in modern Astrophysics, to validate and better constrain this scenario. The importance of this achievement cannot be underestimated, not only for is overall cultural value but also for the large number of physical processes that are connected to the emergence of the PopIII stars, like the physics of star-formation, the explanation of the gap between early and present metal abundances, the metal contamination of the intergalactic medium, as inferred from metallic lines in the Ly_α forest, the existence of massive black holes at high redshift and the reionization of the high-z universe.

Are PopIII stars observables?

Current estimates of the reionization epoch based on the CMB analysis and the existence of mature AGN and galaxies up to z~6.5 suggest that the first stars started shining at z>15, embedded in an optically thick diffuse medium (named IGM, InterGalactic Medium) of primordial composition. This IGM will absorb all the emitted radiation at λ<1215 Å. At such a high redshift, the observable PopIII emission is therefore redshifted at IR wavelentghs (from the H or K bands on), and will be extremely faint, because of the enourmous distance (the distance modulus at z~15 is 51). For these reasons, they are definitely beyond the detection capability of present-day instrumentation and are considered as a prime target for future instruments like OWL or JWST. Even for these facilities, however, the feasibility of dedicated surveys is to be careful evaluated, since it is not obvious that even the collecting power and sensitivity of OWL or JWST is sufficient to detect them.

The direct detection of the PopIII population is made possible by thee different conditions, namely:

1. the IMF in metal free gas clouds is expected to be dominated by high mass stars ("top-hat IMF"), that are very luminous and rapidly explode as SN;
2. the typical scale at which a gas cloud in the primordial Universe is expected to cool, collapse and fragment (and hence to start star-formation) is of the order of 10^6 M_{sun}. PopIII stars could be grouped in clusters of 10^5-10^6 M_{sun} if they form in protogalaxies of at least 10^{11} M_{sun} (quite abundant in the early universe).
3. Metal-free stars are extremely hot and luminous, both in the continuum as well as in the Lyα and HeII emission lines, whose simultaneous detection is an excellent diagnostic to validate the PopIII candidates.

These favourable conditions conspire to make PopIII stars observable with OWL (or JWST), either directly (PopIII star clusters of 10^6 M_{sun} at z~15 are predicted at about m_K=31) or via the SN explosion of the more massive stars therein, that may reach m_K=26-27 for about one month in the observer frame.

In this section, we will better describe these science cases and outline an OWL survey designed to detect and study for the first time these early objects.

7.2.2 The Explosions of PopIII stars

The SuperNovae originated by the explosions of PopIII very massive stars have been studied so far only theoretically, and are therefore still subject to significant uncertainties. These studies, however, all suggest the following picture, as a function of the progenitor mass, that is peculiar of metal-free stars: a)

the few stars with $M < 10\ M_{sun}$ would end their life as white dwarfs; b) for masses between 10 M_{sun} and 30 M_{sun} the SN explosion would leave a neutron star as a remnant while if 30 $M_{sun} < M < 100\ M_{sun}$ there would remain a black hole. However, stars with 40 $M_{sun} < M < 100\ M_{sun}$ probably produce directly a black hole or a GRB without a SN; c) Analogously, stars with 100 $M_{sun} < M < 140\ M_{sun}$ probably encounter the same fate after the ejection of their outer layers caused by pulses of pair instability. d) In our context, the more interesting objects are those originated by the most massive stars, which explode as Pair Instability SN: when they reach carbon burning, their high helium core masses encounter the electron-positron pair instability, collapse and ignite oxygen and silicon burning explosively.

The result is that PopIII stars convert most or all of their mass directly into radiation, thereby becoming among the brightest sources of the Universe. These objects are by far the best candidates for the direct detection of PopIII supernovae, and in the following we will focus on this class only. As discussed above, because of the redshift due to the expansion of the Universe, the light from these objects will be redshifted to near IR luminosity, where we can detect the rest-frame UV emission from these explosions: our considerations in the following will therefore focus on the UV properties of these objects.

7.2.2.1 The expected luminosity of PopIII-PISN

The PI-SN release energies ranging from $3 \times 10^{51} erg/s$, for a star of mass $140 M_{sun}$ in the zero age main sequence (corresponding to an He core of 64 M_{sun}), up to almost $100 \times 10^{51} erg/s$ for a 260 M_{sun} star.

According to detailed theoretical models, the most massive PISN (those with $M > 200\ M_{sun}$) should be easily detectable, as we can see in Figure 34, where it is shown the predicted peak brightness of a 250 M_{sun} PISN at the observed wavelength corresponding to the Lyα (Weinmann & Lilly 2005). The predicted peak magnitudes, albeit fainter than what is achievable by present day telescopes, are easily within reach of OWL-grade instruments.

According to Wise & Abel (2004) (Fig 3) the mass-luminosity relation for PISN is so steep that it is more efficient to attempt the detection of the brighter objects near the upper mass cut-off in the largest possible area of the sky rather than to try to probe further down the mass function in fewer fields.

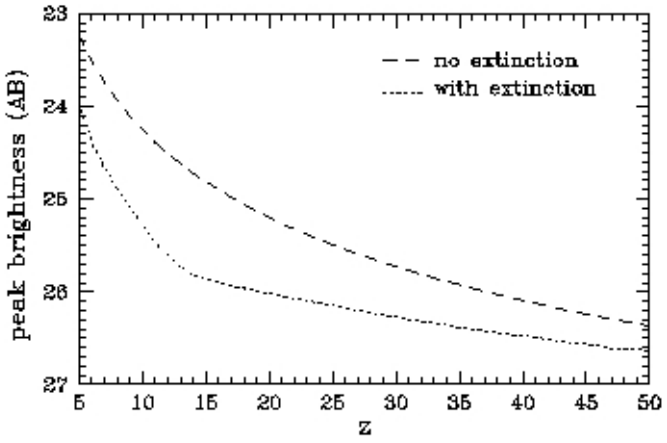

Figure 34: Peak observed brightness as a function of redshift, of a 250 M_{sun} PISN in the region around redshifted Lyα, assuming both no significant extinction and a "worst case" extinction (from Weinmann & Lilly, 2005)

7.2.2.2 The PopIII-PISN light curve

The second key feature of a SN explosion is its light curve. In the case of PopIII-PISN, the typical timescale in the emitter rest frame (defined here as the time required dimming of one magnitude) is of a few days at the Lyα wavelength, and fastly increase with the wavelength. This can be appreciated in Figure 35. Because of the redshift, however, this timescale typically exceeds one month in the observer frame, making these searches practically feasible. This can be deduced from Figure 36, where it is shown the expected observed light curve as a function of time for different wavelengths and stellar masses.

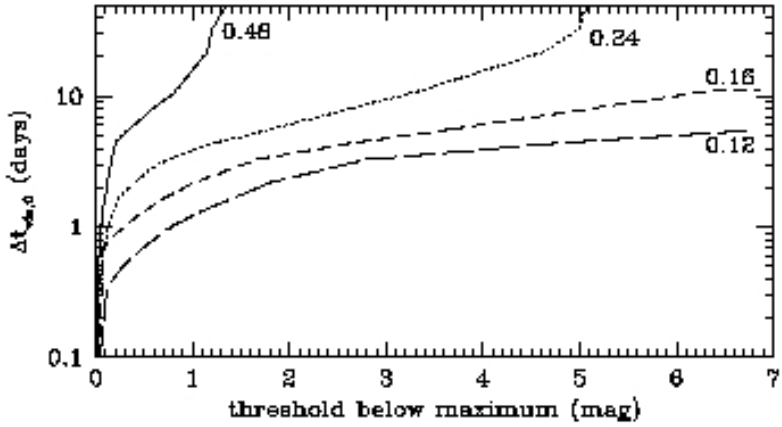

Figure 35: The variation of rest-frame visibility time with the detection threshold at different rest-wavelenghts (from Weinmann & Lilly, 2005).

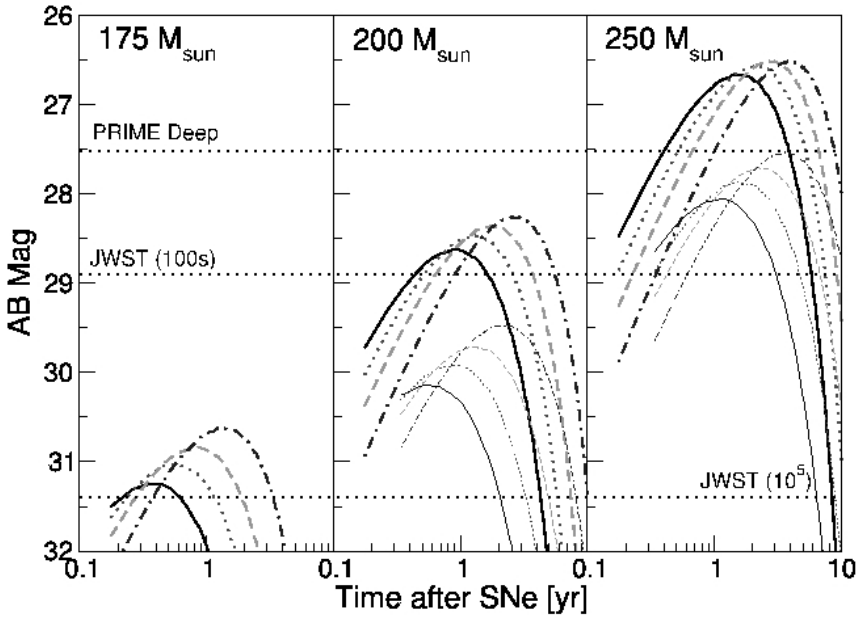

Figure 36: Observed magnitudes and light curves for PISN of different masses at z=15 (heavy-top) and z=30 (light-bottom). The solid, dotted, dashed and dash-dotted are for Spitzer wavebands centered at (3.56, 4.51, 5.69, 7.96) μm (from Wise & Abel, 2004).

7.2.2.3 The rate of PISN explosions

This is likely one of the most debated and uncertain figures, as emphasized by the recent compilation of Weinmann & Lilly 2005. It depends on physical values that have not been clearly determined yet: the star formation rate, that itself depends on the fraction of baryon converted in stars, and on the fraction of supernova producing stars which is obviously related to the initial mass function of PopIII.

Published PISN rates display a broad range of values, that are summarized in the table below (Table 11) adapted from Weinmann & Lilly (2005). In the same paper the authors claim that some values are affected by errors and should be changed: the alternative value proposed for Heger & Woosley (2002) estimate is $0.3 yr^{-1} deg^{-2}$ and for Cen (2003) is $11 yr^{-1} deg^{-2}$. We have to consider that some of these are only crude estimates.

Authors	Redshift range	Rate (yr^{-1} deg^{-2})	f
Mackey et al.	z >15	50	10
Heger et al.	z ~ 20	120	22
Cen	z >13	580	116
Wise & Abel	Cumulative (M ~200 M_{sun})	0.34	0.07
Weinmann & Lilly	Z>15 (M>200M_{sun})	~ 4	1
Weinmann & Lilly	Z>25	~ 0.2	0.04

Table 11: PISN rates according to the studies published so far (adapted from Weinmann & Lilly, 2005).

7.2.2.4 Detecting PopIII-with ONIRICA

In the case of a ground based Extremeley Large Telescope we have to restrict our search to the near infra-red bands like Johnson's J, H, K because of the enormous drop in sensitivity at higher wavelenghts caused by sky brightness and detector and instrumental termal noise. The resulting strategy is to aim at the detection of PISN in as many fields as possible **imaging in the K band with exposures no longer than those required to reach 27 AB magnitude**: that is approximately one magnitude fainter than the peak brightness of a PISN at z ~ 15 - 17 considering the worst case of extinction but is reasonable to expect PISN as brighter as magnitude 26. We restrict our search at redshift less than 17 because at higher z the rest frame wavelenghts probed by the K band are those shorter than Lyα and we aim at the more mossive PISN because of the drop in luminosity shown at lower masses (Wise & Abel 2004). According to our simulations we can reach S/N=15 for a point-like object of AB mag 26 in K band in about 2×10^{-3} hours, (and with the same exposure we reach S/N=5 for AB mag 27). The SN rates presented by Weinmann & Lilly (2005) show that we have to image approximately 4.5 deg^2 to detect one PISN at those redshifts, but we can also consider more optimistic estimates that range up to rates ten times higher (see Mackey (2003) and the table in the previous paragraphs).

We can compute the following required time t_{exp} to reasonably achieve the detection of our first high redshift PopIII Supernova with ONIRICA if we have to image as much as 4.5 deg^2:

$$t_{\exp} \sim \frac{1.2 \times 10^{s}}{FoV^{2} \times f}$$

where FOV is the field of view in arcminutes and f is a factor ranging from 1 to 10 depending on the estimate of PISN rates (1 is for the value of Weinmann & Lilly (2005) and 10 approximately for that of (Mackey, 2003)).

In the case of ONIRICA (1 arcmin^2 of FoV), and comparing the cases $f=1$ and $f=10$, this amounts to 34 hs $f=1$ or 3.4 hs $f=10$.

For reference JWST, imaging PISN of 27 mag at 3.5-4.5 μm, would require from 11 to 110 hours for each PISN (S/N =10, Weinmann & Lilly, 2005)

7.2.2.5 The strategy for searching PopIII-PISN

Putting all together, PopIII-PISN are expected to be relatively bright (at the OWL scale!) objects of m_{AB}=26-27, slowly declining (Δm=1 on timescales > 1 month) and very rare objects (in the worst expected case, one over about 4.5 square degrees). They are expected to be more numerous and more easily observable in the redshift range z =13-17, where they can still be detected in the K band. Although going to longer wavelength bands could increase their detectability, their search is feasible with OWL instrumentation and could provide one of the major results of the ELT adventure.

Because of the many uncertainties about the very existence and the nature of these objects, first studies should maximize the likelihood of detecting them, rather them studying in detail their properties. As a consequence, the most successful strategy should be aimed at looking for the brightest objects in the largest possible area of the sky.

A possible strategy would be made of:

1. For each field, two observations of about 10 seconds in the K band, separated by approximately one month, to reach K=26 with S/N= 15 (and K=27 with S/N=5, that is one magnitude fainter than the expected peak of a M=250 M_{sun} SN)
2. A (nearly) simultaneous observation in J or H band, of both epochs.
3. The selection of high-z SN candidates will be based on the combined presence of three signatures: *a)* the point-like nature of the source, with the absence of any underlying extended galaxy; *b)* the observed variation (of about 1 mag) in the brightness of the point source; and *c)* the absence of any detection (in both epoch) in the shorter wavelength (J or H) that is a unique signature of the extremely high z nature of the source: in the J band we need 10^{-3} hours for each field S/N=5 at mag 27 (and 1σ detection of object of 28.7 mag).
4. Despite the application of these three criteria, the large number of variable sources in the Universe and the expected rarity of PopIII SN strongly advice the immediate follow-up of the selected candidates with a IR spectrograph at OWL, to confirm their nature and accurately measure the redshift.
5. The same strategy should be repeated over 3×10^4 fields (i.e. 8 deg^2) in order to reach the probable detection of at least few candidates in the case of the worst PISN rate or provide a better statistics in the case of a better one.

The grand total observing time is: 172 hs (58 hs in K band, 28 hs in J band for each epoch).

7.2.2.6 Summary

We have shown that a survey for the detection of PopIII SuperNovae is feasible with ONIRICA@OWL and could provide one of the major results of the ELT adventure. Such a survey is very ambitious, as it is based on a large area survey (close to 10 square degree), resulting from a large number of independent ONIRICA points (of the order of 3×10^4 fields). We have however shown that this is a challenging task, that no other planned facility can hope to reach.

We remark that ONIRICA@OWL would outperform the future JWST in this search: even if it can probe longer wavelenghts (3.5-4.5 μm) and so a deeper redshift range and a greater time of visibility for each SN explosion (Figure 35), with a wider FoV, its lower sensitivity at point sources would imply a time more than three times longer for the execution of an equivalent survey, or a smaller final area surveyed.

7.2.3 PopIII during their lifetime: observation of clusters

According to most of current simulations, PopIII stars have formed in clusters of 10^5-10^6 *Msun*, and should therefore be detectable during their main-sequence. The details of radiation emission depend on the mass of the star and, for composite cluster populations, on the chosen IMF. A few values of observable fluxes have been presented in literature according to the numerical solutions of stellar structure equations in the special case of metal-free or metal-poor objects, considering also the effect of nebular emission. For a cluster of 10^6 M_{sun} of metallicity $Z=10^{-3}$ Z_{sun} at z=15, the observed flux at $\lambda \sim 2\mu m$, has been calculated by and would be around m_{AB}=30-31 (Panagia 2004).

However we focus here on a key feature of PopIII stars: their strong Lyα and HeII line. In particular, the latter is significantly stronger in PopIII stars rather than in more metal rich stars.

For a Salpeter IMF and a cluster of 10^6 M_{sun} Tumlinson Schull & Aparna (2003) find that the HeII line at λ = 1640Å have a flux of ~ 10^{-21} *erg* cm^{-2} s^{-1} at z ~15 in the case of continuous burst (SFR=40 M_{sun} yr^{-1}) and of ~ 10^{-19} *erg* cm^{-2} s^{-1} for an instantaneous burst. Thus the detection of these HII regions would be possible with spectroscopy or narrow-band imaging of HeII line at λ = 1640Å.

7.2.3.1 Observational strategy for PopIII clusters with ONIRICA

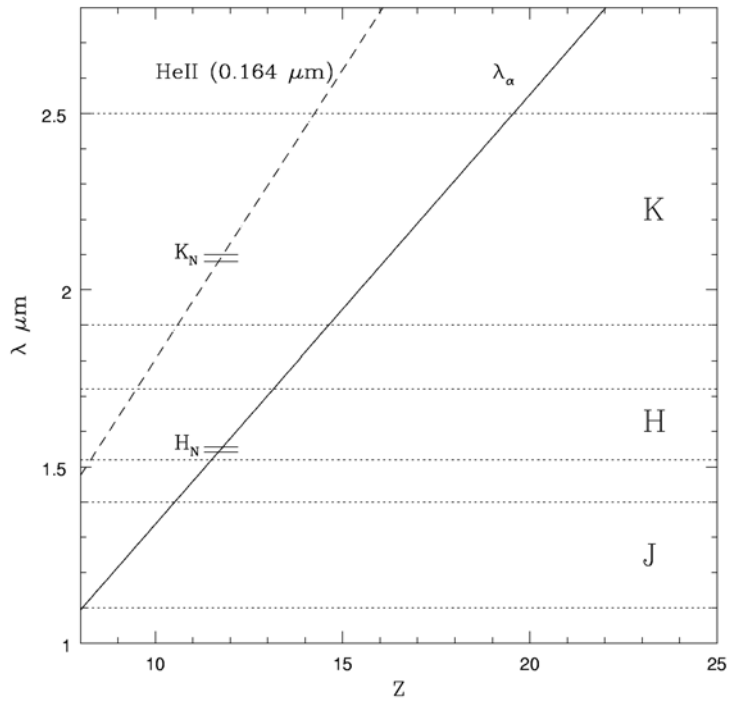

Figure 37: The observed wavelength of Lyα and HeII line at 0.164 μm in function of redshift and the width at half maximum of J, H, H_N, K and K_N filters.

We propose to search for genuine PopIII clusters using a Narrow-Band search in two filters, carefully designed in order to sample both Lyα and HeII lines at the same redshift, hence preventing the false detections due to the much larger number of lower redshift interlopers.

For example, we have considered the case of two narrow band filters, that we name H_N and K_N, respectively, in the intervals 1.542-1.557 μm and 2.080-2.100 μm (this second one is already in use at ESO ISAAC) in which there are not strong atmospheric OH emission lines (Rousselot et al. 2000). The first would detect Lyα emission of a cluster between z=11.68 and z=11.81 and the second the HeII line at 1640Å rest frame at the same redshift.

Using the standard selection criteria for Narrow-Band searches, we need to image the same field with the wide band filters H and K to select the emission line objects, as should be in the case of a PopIII cluster.

We estimated the time necessary to reach the magnitude expected for the Ly-α (~25 AB) and the HeII line (~26.7 in the case of continuos SFR as in Tumlinson et al. 2003) in these filters adopting the tools described in the previous sections. We find that these magnitudes can be reached in a modest amount of time for a 100m OWL: 100sec for H_N and 4hs in K_N.

With respect to standard search technique, the volume sampled by Narrow Band searches is however rather small. In this narrow redshift interval, indeed, the volume sampled in 1 arcmin^2 is about 180 Mpc^3. Unfortunately, the space density of PopIII star clusters has not yet been estimated so it is not possible to determine the exact number of fields to be imaged. Santoro & Thomas (2003), considering 3σ fluctuations on the scale of a root halo of total mass 10^{11} M_{sun}, suggest that these cradles of the first stars should have a comoving density similar to that of group of galaxies (about $3\times10^{-3}h^3$ Mpc^{-3}). In the case of the ONIRICA FOV**, this should imply that we might expect about 0.5 clusters of PoIII stars for each pointing.**

Of course such a detection will imply the existence of an object emitting both on Ly-α and HeII at a certain redshift and does not necessarily imply that this is solely a cluster of PopIII stars. However QSOs, a possible source of confusion, are rather rare compared, at least, with the here adopted estimates of PopIII clusters. Nevertheless it is obvious that only a spectroscopic follow up will convalidate the discovery of such elusive cluster.

However it is important to underline once again that the theoretical work on the subject of existence, formation and abundance of primordial clusters is so poor up to now that we are not allowed to make safe predictions. For this reason, we propose a wide area survey, designed to assess the actual number density of these objects at z around 15.

For instance, a survey of 100 arcmin^2 up to magnitude 25 in H and H_N and up to magnitude 27 in K and K_N would detect around 50 PopIII clusters, if the above estimates are correct, or set stringent limit to their number density, if it is significantly lower. Based on the estimated performances of a 100m OWL, we expect that such a survey can be executed in about 50 h, mostly devoted to the Narrow Band filters (most notably the K_N, for a grand total of 40 h).

References

- Abel T., Bryan G.L. & Norman M. L., 2002, Sci 295, 93
- Bahcall N.A. & Fan X., 1998, ApJ 504, 1
- Bertin & Arnouts, 1996, A&AS 117, 393
- Bromm V., 2004, PASP 116, 103
- Bromm V. & Clarke C. J., 2002, ApJ 566, L1
- Bromm V., Coppi P.S. & Larson R., 1999, ApJ 527L, 5

- Bromm V., Coppi P.S. & Larson R., 2002, ApJ 564, 23
- Bromm V., Kudritzki R.P. & Loeb A., 2001, ApJ 552, 464
- Ciardi B. & Ferrara A., 2004, astro-ph/0409018
- Cen R., 2003, ApJ 591, 12
- Grazian A. et al., 2004, PASP 116, 750
- Heger A. & Woosley S.E., 2002, ApJ 567, 532
- Heger A. et al., 2001, astro-ph/0112059
- Hoekstra H. et al., 2001, ApJ 548, L5
- Mackey J., Bromm V. & Hernquist L., 2003, ApJ 586, 1
- Marigo P. et al., 2001, A&A 371, 152
- Marigo P., Chiosi C., & Kudritzki R.P., 2003, A&A 399, 617
- Nakamura F. & Umemura M., 2001, ApJ 548, 19
- Panagia N., 2004, astro-ph/0410235
- Percival W.J. et al., 2001 , MNRAS 327, 1297
- Perlmutter S. et al., 1999, ApJ 517, 565
- Pope A.C. et al., 2004 , ApJ 607, 655
- Ripamonti E. et al., 2002, MNRAS 334, 401
- Rousselot et al., 2000, A&A 354, 1134
- Santoro F. & Thomas P. A., 2003, MNRAS 340, 1240
- Sokasian A., et al., 2004, MNRAS 350, 47
- Spergel D. N., 2003, ApJs 148, 175
- Stanway et al., 2003, MNRAS 342, 439
- Steidel, 1996, AJ 112, 352
- Tumlinson J., Shull M., Aparna V., 2003, ApJ 584, 608
- Weinmann S.M. & Lilly S.J., 2005, ApJ 624, 526
- Wise J.H. & Abel T., 2004, astro-ph/0411558

7.3 Other possible science cases

The two science cases considered above do not certainly exhaust the possible science applications of the proposed instrument. They are mainly meant to emphasize the possible science outcome that result from the foreseen capabilities of ONIRICA.

Indeed, as expected for a general purpose imaging camera, ONIRICA may be used for several other scientific observations. In the following section we describe in some detail two other possible science cases that would benefit of the capabilities of ONIRICA.

In the first case we consider application of the camera that exploits the astrometric capabilities of the instrument to investigate the baryonic distribution of matter. Infact the dramatic improvement in

sensitivity for near-diffraction limited imagery on a 60-100m telescope are opening the possibility of applying micro-lensing techniques to the problem of establishing a complete inventory of massive galaxies. This includes the possible detection of extra solar planets in elliptical galaxies, detect the effects of dark matter, and probe the dark massive objects at the centres of galaxies.

Another interesting field of application concerns the study of the effects that regulate the star formation process. These included the interaction of a stellar wind with the circumstellar disk and ambient cloud where the proto-star is formed. ONIRICA will be able to provide an unprecedented opportunity to study these fundamental processes at angular scales corresponding to less than 1 AU at the nearest star forming regions.

7.3.1 A Complete Inventory of Massive Galaxies

What are galaxies made of? Our view of other galaxies is dominated by bright, atypical stars, either young, recently-formed objects (at blue wavelengths) or evolved giants (at red and near infrared wavelengths). As a result, performing a complete visual census of stellar, sub-stellar, and planetary mass objects in external galaxies is impossible, due to the low luminosity of the very objects which make up the majority of the population. Even a 100m telescope, aimed at a massive nearby galaxy, such as M87, cannot make a conventional stellar census.

Nevertheless, the low mass stars (<1 M_o), brown-dwarfs and planets, which dominate the mass in normal stellar populations, are compact enough to gravitationally focus the light of background objects, and hence be detected. The phenomenon of *gravitational micro-lensing* has been discussed and pursued for a decade as a means of revealing unseen mass, particularly in our own galaxy. The sensitivity gains with near-diffraction limited imagery on a 60-100m telescope are dramatic, scaling as D_{ap}^4, opening the possibility of applying micro-lensing techniques to the problem of establishing a complete inventory of massive galaxies.

7.3.1.1 Gravitational Micro-lensing

If a light source happens to lie behind a mass concentration (the lens), as seen from an observer, then gravitational focussing may create multiple images, separated by a characteristic angle on the sky, the Einstein ring radius, θ_E:

$$\theta_E = \sqrt{\frac{4GM}{c^2}\frac{D_{LS}}{D_S D_L}},$$

where M is the mass of the lens and $D_{L,S}$ are the distances from the observer to the source and lens, and D_{LS} is the lens-source distance. Figure 38 illustrates the geometry of the lensing process.

If the Einstein angle, θ_E, is resolved, then the phenomenon is called “strong lensing”. If it is unresolved, the effect can still be detected if the relative positions of the lens and source change (bottom half of Figure 1). For example, if the source moves behind the lens, the total magnification (sum of all images) changes, producing a characteristic variation in brightness. Such light curves have been well established by observations of the Magellanic Cloud and the Milky Way’s bulge (e.g. Alcock et al 1997; Udalski et al 1994).

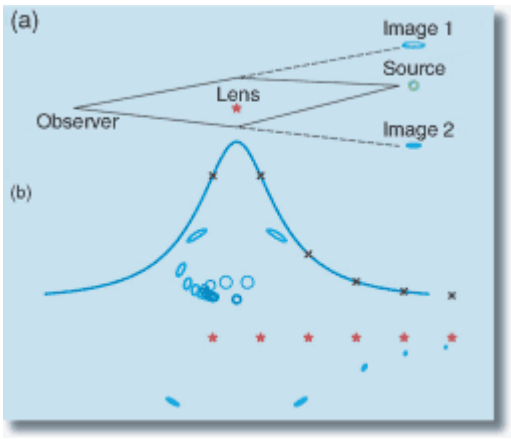

Figure 38: Schematic overview of gravitational micro-lensing: as the relative source-lens positions change on the sky, e.g. through the motions of stars within a galaxy, the degree of magnification of the background *source* by the foreground *lens* changes as a funtion of time, resulting in the characteristic micro-lensing light-curve (blue solid line).

In micro-lensing the only observable is the characteristic shape of the light curve resulting from the time-dependent magnification. The peak amplification relates to the minimal source-lens alignment (in units of the Einstein ring radius), while the characteristic width of the light curve corresponds to the "Einstein ring crossing-time", which in turn depends on both the relative angular speed of the lens and source and on the mass of the lens, (which sets θ_E).

The Complete (Sub-)Stellar Mass Function in M87

Simple estimates (e.g. Rix 1998) show that with ONIRICA's imaging capability, the optical depth to "self-lensing", by and of stars within M87 is enormous: at any given time, the central 1'×1' of M87 (Figure 39) would have ~100 micro-lensing events that would be detectable with the resolution and sensitivity of a moderate aperture space telescope, such as JWST. In such an event, a lensing magnification of giant stars within M87 is caused by mirco-lensing of a (usually) low-mass "foreground" star still within M87. For JWST observations of self-lensing in galaxies such as M87 the main limitation source confusion noise, i.e. a light-curva variation must be detected against the fluctuating background of partially resolved stellar populations. This effect is reduced by $(D_{JWST}/D_{OWL})^2$ in the diffraction limit. Observations with ONIRICA will also be confusion limited for

$$\mu_{M87}(R) < \mu_{sky,K} + 2.5\ \mathrm{Log}(S/N_{\text{"sky-in-K"(resolution-element)}}) \sim 19\ \mathrm{mag/arcsec}^2$$

For M87 this holds to R>60", and the light-curve detection is limited by the photometric accuracy of clump and giant stars in M87, appearing at m_K~26. Scaling from can expect ~500 micro-lensed giant stars (by >20%) in a 1'×1' FOV at the center of M87.Given typical velocities, and the size and distance of M87, the duration of such micro-lensing events are $t \sim 1 Month \left[M_{Lens} / M_{\odot} \right]^{1/2}$, i.e. weeks for stellar mass lenses, ½ day for Jupiter mass lenses and 1 hour for earth mass lenses. The relative incidence of lensing events by "high-mass" (~0.5M_o) to low-mass (planet) events, scales linearly with their contribution to the (sub-)stellar mass density in M87, for single objects. For planets bound to lensing stars, the cross section is much higher (Gould and Loeb, 1992).

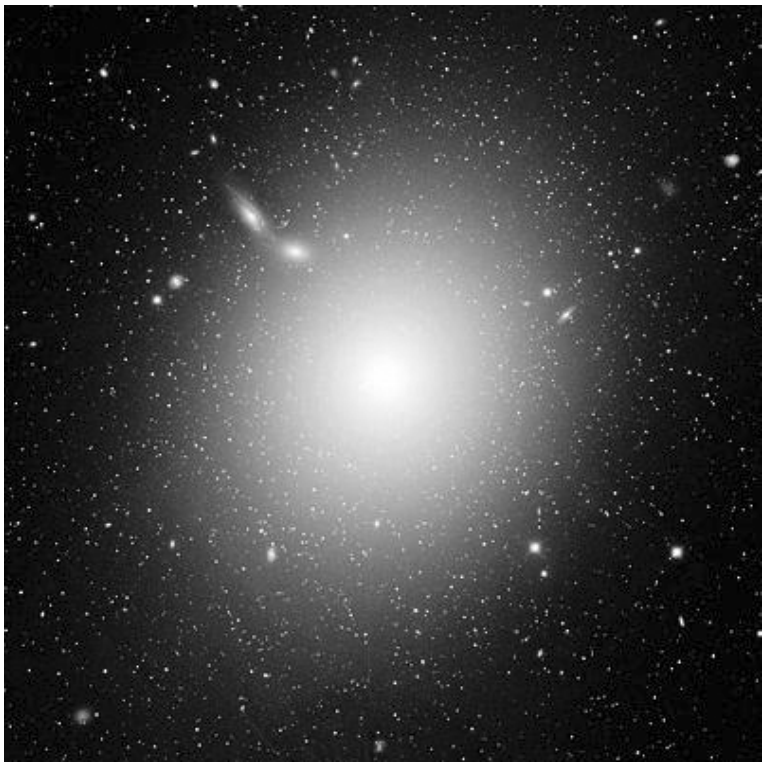

Figure 39: M87, the giant elliptical galaxy in Virgo.

The high rate of events allows us to solve several important problems in the astrophysics of galaxy-scale stellar systems. For example, in a collisionless system, such as a giant elliptical, the kinematics of the low-mass objects mirror the (measurable) kinematics of the giant stars, and their spatial distribution will be similar. Hence, the micro-lensing event amplitude/duration distribution will immediately translate into a lens-mass distribution, which corresponds to the mass distribution of discrete sources in the galaxy. By imaging at the center of M87 and 1'- 4' away from the core, we can trace in detail the radial gradients of the stellar population. With ONIRICA on OWL, similar studies can be carried out for any giant galaxy within ~20 Mpc. The power of this instrument combination comes from the reduction in crowding or confusion noise, which scales as the 4^{th} power of the FWHM of the PSF core.

7.3.1.2 Ancient Worlds: Hunting for Planets in Elliptical Galaxies

Direct searches for extrasolar planets are concentrating on the youngest and hence brightest objects in the nearby universe. Shedding light on the first generation and hence oldest planets may seem beyond the scope of foreseeable observations. However, searching for planets in the most ancient stellar populations in the local Universe is quite feasible with ONIRICA: such populations may be found in the heart of the oldest local galaxies, giant ellipticals. Micro-lensing observations with ONIRICA should allow detection of planets in M87. It is known from the Milky Way that the cross-section for lensing is one hundred times lower for planets than for stars. Nevertheless, with thousands of stellar lensing detections, we can anticipate dozens of planet events.

7.3.1.3 What the Universe is made of: Dark Matter Detection

While the MACHO and OGLE experiments have shown that compact low-mass objects are not an important part of the dark matter mass budget of our galaxy, non-luminous and pervasively distributed objects are expected in the early phases of the universe. For example, if some Population III stars either formed black holes or held on to their mini-halos, they could still be detectable. If there is a mass

component in the Virgo cluster which is concentrated in discrete, compact form, micro-lensing experiments with ONIRICA can establish limits on their contribution down to 0.001 of Ω_{baryon} (Rix 1998). Distinguishing between "self-lensing" and possible MACHO events is straightforward on the basis of timescales and optical depth (the self-lensing optical depth scales as the surface density of stars squared).

7.3.1.4 The Centers of Globular Clusters and Galaxies, Including the Milky Way

The centers of galaxies have proven to be enigmatic and complex, and recent evidence suggests (Sazonov et al, 2005) that through feed-back from the black hole, the core may regulate the formation of the overall galaxy. Our own Milky Way's center has taught us a simple lesson: the cores of galaxies have become more fascinating and important as a fundamental laboratory of physics (e.g. Genzel et al 2003).

ONIRICA opens up three crucial areas of research with its combination of high angular resolution and sensitivity: (1) we can see stars in the "back" of a galaxy being lensed by the central black hole; (2) we can resolve other galaxy nuclei into stars and observe their proper motions; and (3) we can study the (young) stellar populations of other galaxy centers, and hence understand the interplay of star-formation and the feeding of black-holes.

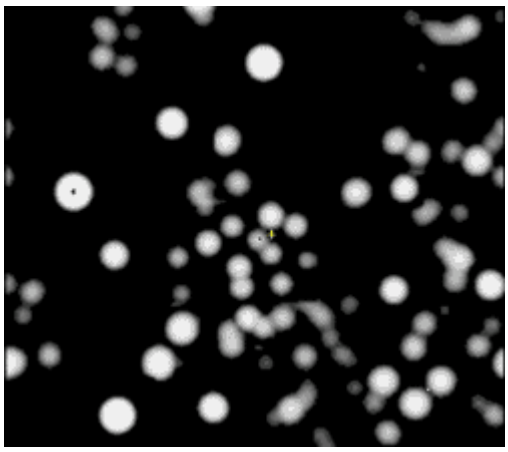

Figure 40: ONIRICA will be able to see the nucleus of M31 at nearly the same resolution as HST can see the center of our own Milky Way.

7.3.1.5 Dynamics from Proper Motions

Most studies of galaxy center dynamics are based on measurements of the line-of-sight velocities of tracer particles, either stars or gas. This approach, in isolation, leaves 2 (of 3) velocity components unmeasured and the physics of the problem requires that the missing information be "invented," usually by artificial constraints on the geometry of the problem, such as sphericity or isotropy. However, the few examples where precision proper motion measurements have been made have lead to some of the most spectacular results: the Galactic center (Genzel et al 2003; Ghez et al 2003); NGC4258 (Myoshi et al 1995); and the globular ΩCen(van Leeuwen et al 2000, D'Souza and Rix 2005).

The Milky Way studies in particular have demonstrated the power of relative in-field astrometry using diffraction-limited observations at near-infrared wavelengths. As outlined in e.g. Weinberg et al (2005), observing the lowest order relativistic effects (prograde procession) will require ~200 μas precision and 10-year time-scales, while frame-dragging will require a precision of 50μas. The power of a 100m

telescope enters not only as the D^2 gain in positional precision for a given star and given exposure time, but also through the increased number of stars accessible, due to the fainter flux limit.

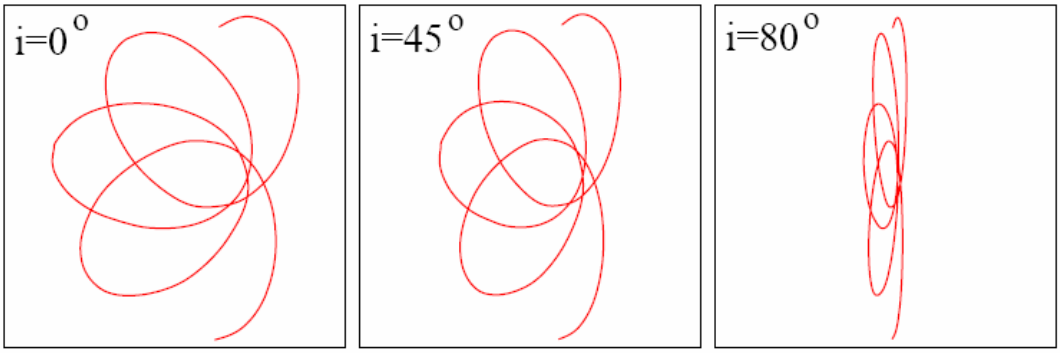

Figure 41: From Rubilar and Eckart (2001), showing the pericenter precession for an "S2-like" star at the galactic center.

7.3.1.6 Proper Motion Studies in Galactic Centers

The science objectives of proper-motion studies in our Galactic Center will be two-fold: (1) it will improve by two orders of magnitude the precision and power to probe relativistic effects, and hence test fundamental physics; and (2) it will us for the first time to probe scales within 10^{15} cm of the black hole, were stellar disruption may occur.

In external galaxies, a 100m telescope equipped with a near-infrared diffraction-limited camera will open up for the first time studies of individual extragalactic stars. Specifically, M31 can be studied in this way. The diffraction limit of a 100m telescope at the distance of M31 (0.01pc) basically corresponds to the same resolution that HST NICMOS can achieve at our Galactic Center. M31's nucleus is dynamically very different from ours, and consists of either a *double nucleus* or an eccentric disk (Tremaine 1995). Assessing the variety of galactic nuclei dynamics on milli-parcsec scales is a key ingredient in understanding black hole growth.

7.3.1.7 Proper Motion Studies in Globular Clusters

We do not know whether globular clusters harbor black holes with masses in excess of those expected for stellar remnants (~$10M_o$), yet this is a central question in understanding how massive black holes in large galaxies were "seeded." If the M_{BH}-M_{star} relation (e.g. Haering and Rix, 2004) holds down to globular cluster masses, then black holes of 100-1000 Mo are expected. These cannot be found with radial velocity studies on 10-20m telescopes, due to the finite number of tracers and confusion effects.

With the sensitivity and spatial resolution of ONIRICA, we should be able to achieve a velocity precision of 1km/s at 5kpc for stars of m_K=25, and the minimum separation from the black hole that can be resolved is 10μpc, where the velocities are expected to be in the neighborhood of 500km/s.

References

- Alcock, C. et al 199, ApJ 486, 607
- D'Souza, R. and Rix, H.-W. 2005, ApJ submitted (astro-ph/0503299)
- Genzel, R. et al 2003, Nature 425 934
- Ghez, A et al 2003 ApJ 586 L127

- Gould, A, and Loeb, A, 1992, ApJ 396, 104.
- Haering, N. and Rix, H.-W. 2004, ApJL 604 89
- Miyoshi, M. et al 1995, Nature, 373, 127.
- Rix, H.-W. 1998, «NNGST Design Reference Mission », http://www.stsci.edu/jwst/science/drm/pdf/drm5.pdf
- Rubilar, G. and Eckart, A 2001 A&A 374 95
- Sazonov et al, 2005, MNRAS 358 168
- Tremaine, S. 1995 AJ 110 628
- Udalski et al 1994, AcA, 44, 165
- van Leeuwen, F. et al 2000 A&A 360 472
- Weinberg, N. et al 2005 ApJ 622 878

7.3.2 Star formation regions at high angular resolution

7.3.2.1 Wind – Disk – Environment Interactions

The "standard model" of star formation postulates that a collapsing molecular cloud forms a deeply-embedded protostar that grows by radial infall. Primordial angular momentum forms a disk around the growing star, and this disk allows further collapse by either directly producing or mediating a wind, which carries away angular momentum. The wind in turn eventually breaks out of the stellar cocoon and deposits energy in the ambient molecular cloud, stirring up and dispersing it, thereby preventing further collapse events.

Thus, the interaction of a stellar wind with the circumstellar disk and ambient cloud both catalyzes and regulates the star formation process. Unfortunately, the small angular scales and the presence of obscuring dust have severely limited our ability to probe the regions where these important interactions take place. The near stellar environment remains one in which our observational understanding lags behind theoretical developments.

A diffraction-limited near-infrared imager on OWL will provide an unprecedented opportunity to study these fundamental processes at angular scales corresponding to less than 1 AU at the nearest star forming regions.

Such studies are now in their infancy using the VLTI and other facilities, which offer the necessary spatial resolution. Unfortunately, it appears that the interactions zones are very complex on all angular scales (Figure 42), and long baseline optical/IR interferometry is not suitable for imaging complex phenomena. The rule of thumb is that one observation is needed per degree of freedom in the source distribution model. In addition, many diagnostic spectral features are faint, but they must be accurately measured in the presence of an extremely bright continuum source (Figure 42). Understanding these phenomena requires true imagery, high dynamic range, and good sensitivity.

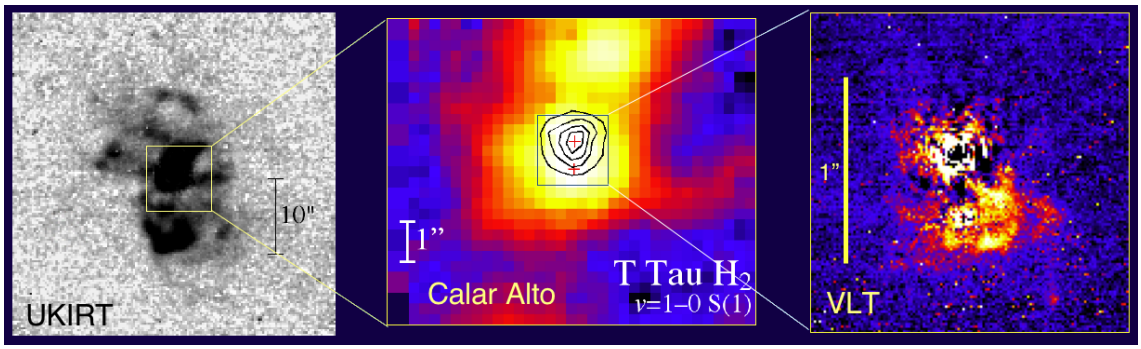

Figure 42: Star formation is complex at all angular scales. This sequence of images zooms into the core of the prototypical young stellar object, T Tau. With the spatial resolution afforded by a 100 meter telescope, we will finally be able to unravel the mysteries of the star and planet formation process at scales smaller than the Earth's orbit in the nearest star-forming regions.

Potential key science programs for studying the wind-disk-environment interactions include:

1. Direct imaging of the near stellar environment to analyze the interaction of the wind with the disk and surrounding material, including asymmetries, condensations, and wavelength--dependent properties (scattering versus thermal emission).

2. A monitoring program of circumstellar emission, coupled with high resolution spectroscopy, can give the full, three-dimensional motions of the gas in the near stellar environment. This can constrain the energy injection into the molecular cloud. Note that with the OWL infrared imager, a shock front travelling at 25 km/s in Taurus will move noticeably from one observing night to the next.

3. Imaging spectroscopy with narrow band filters to study the interaction of the wind with the disk and ambient medium. These measurements can reveal the temperature structures of shock fronts, energy deposition rates, and possibly isolate the wind collimation mechanism through spectral features diagnostic of interactions.

4. Related programs with other instruments: High spectral resolution NIR spectroscopy to reveal the velocity field in the wind (using recombination lines), circumstellar disk (via CO and other species), and ambient medium (H_2, forbidden transitions). Other spectroscopic programs may include isolation of infall and outflow regions, kinematics and turbulence in the ambient cloud, and transport of mass, energy and angular momentum within the disk and to the surrounding cloud.

7.3.2.2 Structure of Circumstellar Disks

As mentioned before, circumstellar disks have an important influence on molecular cloud collapse, by either generating or mediating stellar winds. Disks are also of fundamental importance in planet formation, since they act as both a source of raw material and as a shielding envelope to allow the accumulation of the gas and refractory elements which eventually become a planet. Through accretion and resonant scattering, the planet eventually clears a gap in the disk, inexorably altering its structure and dynamics.

Direct imaging of thermal emission from hot dust grains would be the best means of studying these processes. Such grain temperatures occur only in the inner disk, within a few tenths of an AU of the central star. At the distance of the nearest star forming regions, this corresponds to a spatial scale of a few milli-arcseconds, within reach of the proposed near infrared imager for OWL. Such an instrument can of course also search for evidence of these processes in scattered light at larger distances. As with the stellar wind interactions, true, panoramic, high dynamic range imagery is essential.

Note also that, given the great distance to the nearest protostars, the spatial resolution afforded by a 100-meter class telescope is essential to unraveling disk evolution and planet formation process on scales comparable to the Earth's orbit.

Potential key science programs for studying the structure of circumstellar disks include:

1. Searching for and imaging circumstellar disks in thermal emission and scattered light. Indirect signatures of planet formation include gaps, resonances, and asymmetries in the disk light distribution.

2. Characterizing the size, dust distribution, and viewing geometry of circumstellar disks. These disks are expected to flatten with increasing age during the transition from protostellar to protoplanetary phase, a process that we hope to follow with a survey. In addition, there is increasing interest in the structure, dynamics, and evolution of circumbinary disks. Sensitive, high dynamic range imagery may prove essential in understanding these systems.

3. Related programs with other instruments: These programs will have a natural synergy with those proposed for EPICS.

8 The opto-mechanical concept

In the following sections we will describe several concepts concerning the opto-mechanics both of the scientific camera and of the adaptive optics wavefront sensor. A class of possible solutions is presented, and we try to identify for each of them the advantages and disadvantages. Anyway, whenever possible, we have focussed our attention to a restricted number of opto-mechanical solutions that we think can represent a good compromise between scientific constraints, technology availability and opto-mechanical complexity. We tried to minimise the amount of technological developments needed for the camera, following the philosophy that in principle even with components available today the instrument might be realised, but we also presented some solutions which are taking into account a moderate development of technology, for example in the detectors RON. In the end, some possible opto-mechanical arrangements in one of the six OWL focal stations are finally presented.

8.1 The Camera opto-mechanical concept

Given the expected size of the pixel (around 18μm) of a NIR array, one needs focal ratios of the order of a few times more than the input focal ratio at the input of ONIRICA (a Nyquist sampling in J band requires an F/24, four times larger than the F/6 OWL input focal plane). Using buttable CCD arrays one could conceive a big focal enlarger with lenses in the diameter range of the order of 500mm or more. While this is doable for conventional glasses in the optical domain, although with lengthy procurement times and still not being free from troubles in terms of quality of the glass melt and coating durations, it is extremely demanding for NIR glasses (even the most common ones). Clearly one could speculate that in the time this camera would turn into reality the situation could be greatly improved. However, given the constraint we posed to ourselves about the feasibility of the camera, we preferred not to rely on the buttability condition and to split the optics of ONIRICA in a number of replicas of the same optical train, each covering a fraction of the FoV to be imaged. We hence conceived a modular optical concept in which the FoV is split into four quadrants by means of a reflective pyramid with 90 degrees vertex angle. This translates into a subdivision of the covered FoV into four patches each half the size of the original one. Further, hierarchical, subdivision will allow for subdivision into 16, 64… patches, each with a size of 1/4, 1/16… of the original one. The optical design is basically unchanged for each of these elements of the "tree" as the physical size of the lenses is basically unchanged. In fact the FoV is reduced by a factor two but the focal length is about doubled, given the final choice for the focal ratio. The optical quality of

this optical train is dominated by the first elements, as the focal ratio increases in the following arms of the tree.

As already mentioned, there are various options regarding the final F/# (and the corresponding enlarging factor to be applied in ONIRICA), which are dependent also on the detector size, the choice of which represents a compromise between the system performance, its complexity and its final cost. For this reason, we analyze different cases that will be useful for the evaluation of the final choice of the detector design. In Table 12, different cases of detector sizes are listed, taking into account the two or three hierarchization options (see Figure 43) and a FoV of 30" and 60". The focal ratio of the F/6 beam coming from the telescope is doubled before every ramification in order to halve the plate scale and to leave unchanged the beam dimension. The final choice will depend of course also on the detector availability. As already said, we consider reasonable that, in a few years, detectors 4k × 4k with 12μm pixel size should be easily available. We also point out that, when considering the system complexity, a fundamental role will be played by the presence of the cryogenic cooling systems, especially for the three-level configuration shown in Figure 43, which is pushing in the direction of having less detectors, accepting a compromise in having poorer spatial sampling or smaller FoV.

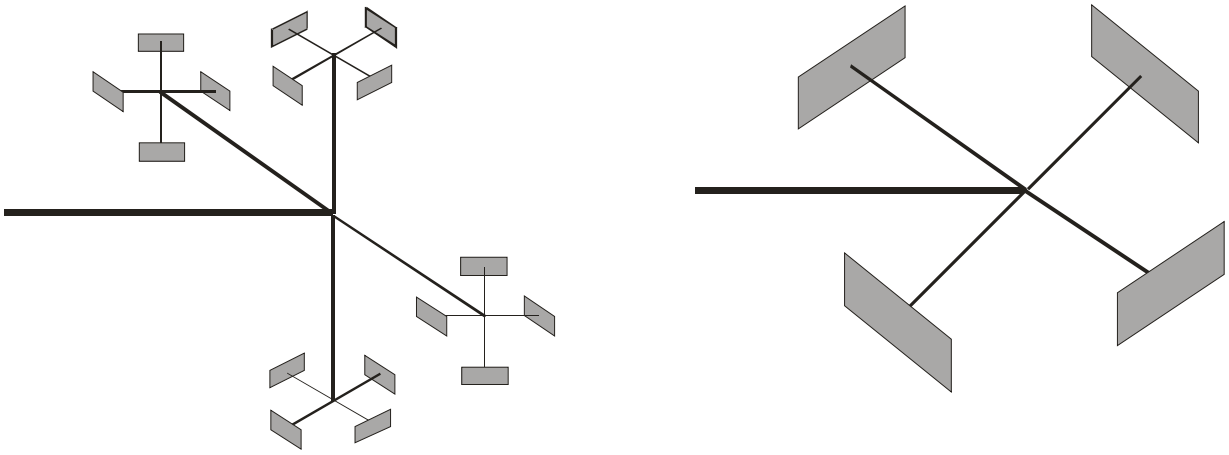

Figure 43: The left part of the figure shows a three levels case for the NIR-camera composed by 16 detectors while the right part shows a two levels case, having four detectors. A pyramidal beam splitter divides the beam in every ramification; the four beams are collected by four focal enlargers which double the focal ratio, causing the plate scale to be reduced respectively by a factor of 4 and 2.

FoV	2 levels ramification				3 levels ramification			
	Split FoV	F/#	Pixel size		Split FoV	F/#	Pixel size	
			12μm	18μm			12μm	18μm
			Detector no. and format				Detector no. and format	
30"	15"	12	4× 4k×4k	9× 2k×2k	7.5"	24	4× 4k×4k	9× 2k×2k
60"	30"	12	16× 4k×4k	9× 4k×4k	15"	24	16× 4k×4k	9× 4k×4k

Table 12: In this table are listed possible choices to cover 0.5 and 1 arcmin FoV. The reported numbers of a given format arrays refer to a single sub-field. For instance, covering 1×1 arcmin in a two-levels camera with 12μm pixel dimension requests, for each of the four sub-fields, to use four 4k × 4k detectors, likely easily available in the next future.

In Table 12 possible detector array choices are listed. Two different FoVs and hierarchical levels are considered. The choices presented in the table are based on the assumption that the focal plane mosaics are realized using 4k×4k or 2k×2k detectors.

In the following we will present two possible camera designs, the first considering a scientific FoV of the order of at most 60", the second having an additional external annular FoV (from 1' to 6') characterised by a coarser sampling, which is interesting in the view of having a real wide field partially corrected scientific FoV.

8.1.1 A preliminary optical solution

The basic unit of this system is represented by the focal enlarger shown in Figure 44, whose purpose is to magnify the OWL focal plane by a factor of 2. The input focal plane for this unit corresponds to an angular field of 1 arcmin on the sky; the linear diameter of this focal plane at F/6 is D ≈ 180 mm. The optical design of the focal enlarger has been optimized taking into account the OWL design and in the wavelength range 1.0μm – 2.35μm. The focal enlarger is basically composed by a 3-lens collimator and a 4-lens objective. The lenses are designed using materials with high transmission in the near infrared (SILICA, CaF2, IRG2, IRG9, IRG11); all lens surfaces are spherical and fully air-spaced to avoid trouble into glued or contact lenses. However the optical quality of this basic design is not acceptable. In order to achieve the diffraction-limit, an attempt has been made to insert additional lenses in the collimator and/or objective. However the number of additional lenses is not compatible with the requirement to minimize the reflection losses and the total infrared emission. A much more effective solution has been the insertion of an aspheric plate in the intermediate pupil plane between the collimator and the objective; in this way, with a single additional refractive element, it is possible to achieve the diffraction limit. Of course a cold stop may be placed in this intermediate pupil plane. The optical design is shown in Figure 44 and in Table 13.

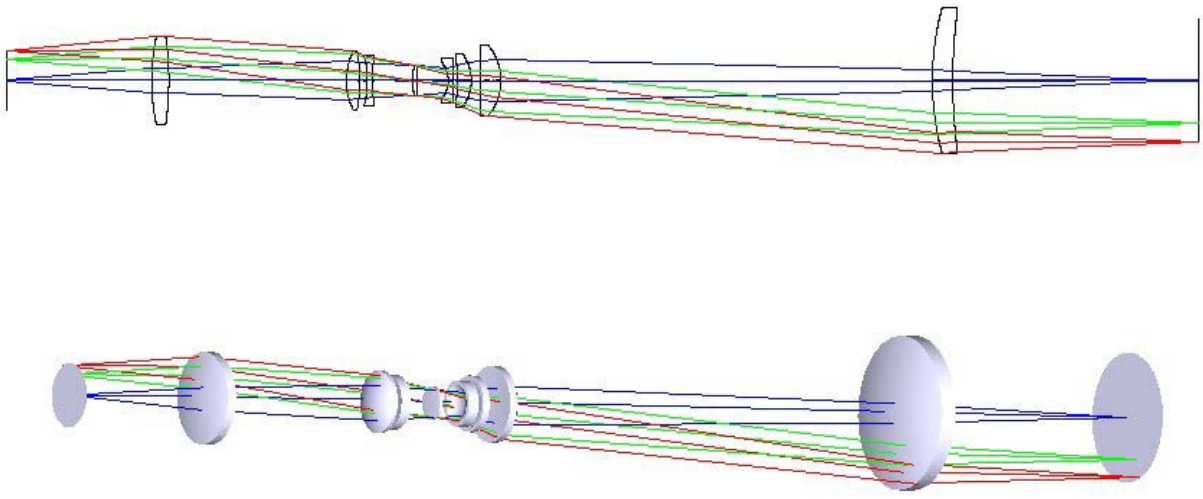

Figure 44: optical layout of the focal enlarger for the central 1 arcmin FoV. Above: 2D layout. Below: shaded model (the first and last circles represent the input and output focal planes). Different colours correspond to different field angles

A possible location for the filters is between the last lens of the collimator and the aspheric plate, i.e. close to the pupil plane. The distance between these two optical elements (nominally 120 mm) should be enough to insert one or two filter wheels for instance. Given the constraints on the total length of the focal enlarger (and hence on the ratio of focal lengths between the objective and the collimator), the maximum incidence angle on the filters is of the order of $\theta \approx 10°$ for a source at the edge of the FoV. This value should be taken into account when designing filters with interference films, in order to minimize the variations of spectral transmission across the FoV.

Comment	Radius	Thickness	Glass	Diameter
F/6 OWL focus	Infinity	427.581		177.1
L1	634.238	50.000	IRG9	255.7
	-914.604	521.111		255.7
L2	192.480	40.000	IRG9	173.1
	-425.331	21.383		173.1
L3	-291.733	15.000	SILICA	151.1
	475.651	120.000		139.5
Even Asphere (*)	Infinity	10.000	CAF2	91.4
	Infinity	92.793		91.4
L4	-85.275	15.000	IRG11	104.1
	2347.980	12.890		127.0
L5	-362.094	40.000	CAF2	134.7
	-131.703	27.240		155.7
L6	-1773.893	60.000	CAF2	197.4
	-159.164	1265.932		211.0
L7	801.180	60.000	IRG2	425.3
	1585.346	721.072		417.7
F/12 focus	Infinity			358.6

Table 13: optical prescription data of the focal enlarger. All dimensions are mm.
(*) Even Asphere coefficients: r^2= 0.00057275808, r^4= 1.52092e-007, r^6= -1.7562133e-010, r^8= 1.3744823e-013, r^{10}= -5.2127506e-017, r^{12}= 7.7809608e-021.

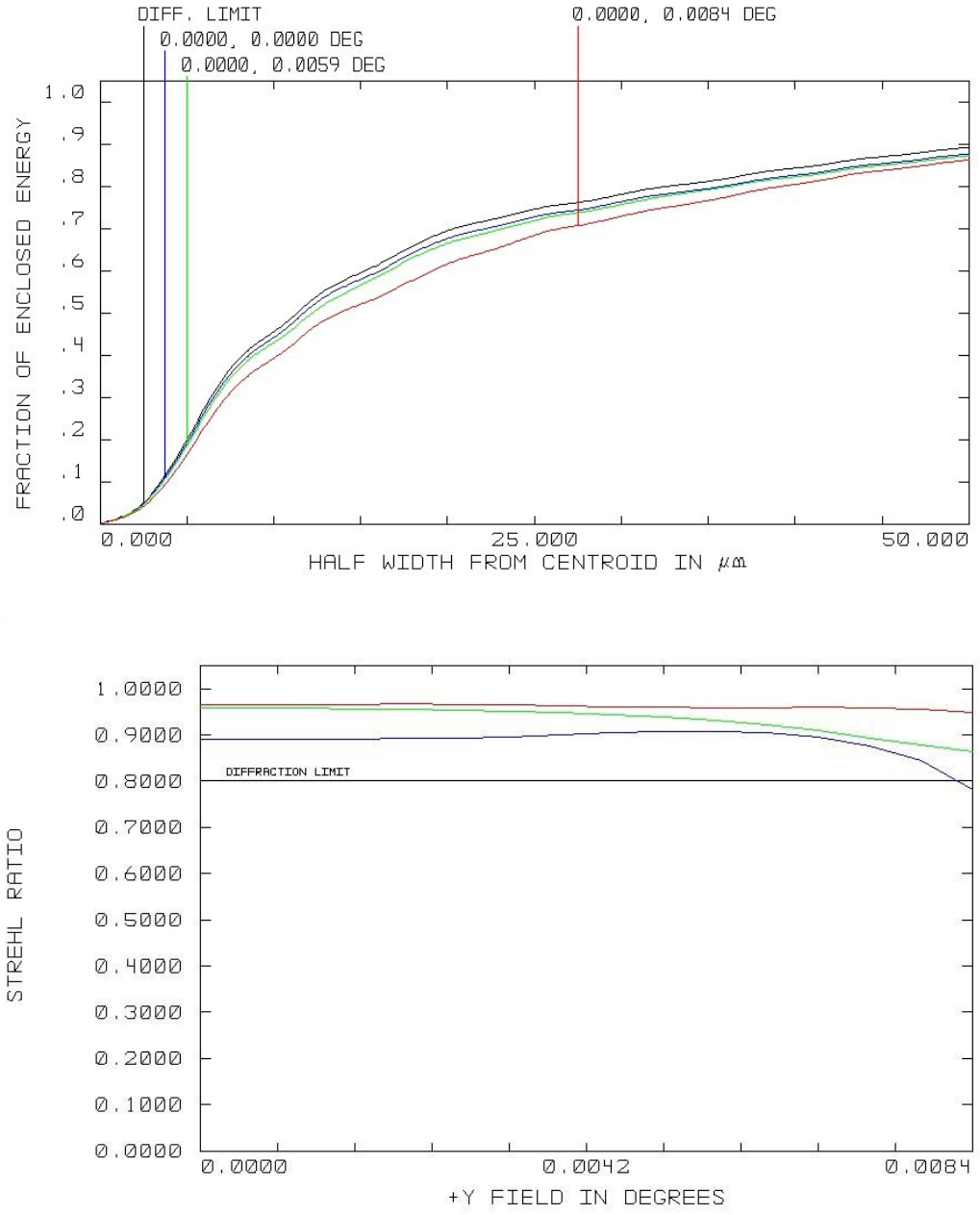

Figure 45: Optical performance of the focal enlarger. Above: polychromatic diffraction ensquared energy for different field angles (colours correspond to field angles). Below: Strehl ratio across the FoV (colours correspond to wavelengths)

As shown in Figure 45, the optical quality of the focal enlarger is substantially diffraction-limited. The geometric distortion is very small: at the edge of the field the percentage distortion is of the order of 0.003%, corresponding to approximately 6 μm linear displacement between the actual and the "ideal" (i.e. undistorted) image position.

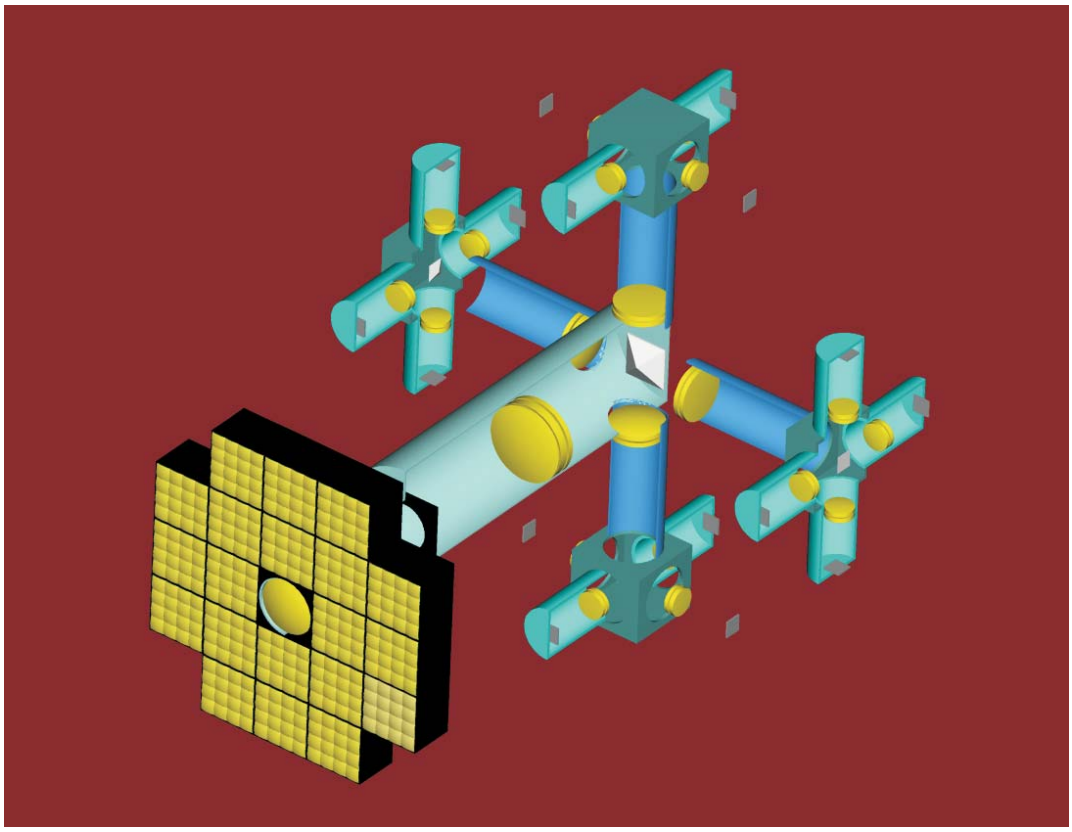

Figure 46: A possible optical arrangement of the infrared camera for OWL

8.1.2 The Wide Field option

As mentioned in the previous chapter, while the main science objectives focus onto the high angular resolution one arcmin camera described above, there is a somehow easy option to have an add-on for a true Wide Field option, with limited correction, and hence with a coarser pixel size, around the main channel. A possible optical arrangement for the wide field camera for OWL is shown in Figure 46, where one can note on the left side of the drawing what is known as a Smart Fast Camera (SFC) array covering a annular FoV from 1' to 6', working with a spatial sampling matching a low order correction, of the order of several times the diffraction-limited FWHM image size. This part of the camera is essentially a focal reducer with a relatively large plate scale, based on the concept to split the considered FoV in smaller portions, each imaged by a lenslet array on a dedicated detector.

This choice is driven by the demanding amount of detectors that would be needed to sample the complete FoV in diffraction limited way. In fact, considering an F/6 input beam and a pixel dimension of 18 μm, the F-ratio of the beam must be increased of a factor 3 to obtain the correct scale on the focal plane in J-band, meaning in this case 1 pixel corresponding to the FWHM of a diffraction limited star. This translates in a required number of conventional 2k × 2k detectors of the order of 10000 to cover the complete 6' FoV. Even assuming a reasonable technological development in the next years that will provide off-the-shelf 4k × 4k detectors, the gain will become only of a factor of four. Furthermore, considering a Nyquist sampling, all this numbers shall be multiplied by a factor 2. Thus the reasonable choice is to have two different areas sampled in different ways, which of course impacts also the performance of the MCAO system coupled to the camera. In fact, such a system requires of course a high order correction in the central part and a low order correction in the outer part of the scientific FoV. A possible layout to accomplish this correction is to consider a real MCAO system (with 2-3 DMs conjugated to different altitudes) acting in the central 30"-60" FoV, while on the annular region up to 6' a GLAO is required.

8.1.3 The annular part of the FoV: a Smart Fast Camera

The concept of the Smart Fast Camera is the following: the image formed in the focal plane is segmented by an array of lenslets of the dimension of about 15 arcsec to 1 arcmin. In the pupil plane an array of aberration correctors is placed in order to correct the approximately constant aberrations in the FoV of each lenslet system. At the end an array of camera lenses produces an array of images detected by the scientific arrays, with the requested plate scale. Figure 47 shows the optical sketch of one unit of the array. The incoming beam is collected by a field lens which produces a pupil image, where an aberration corrector is placed. Then a short focal ratio lens focuses the image onto the CCD.

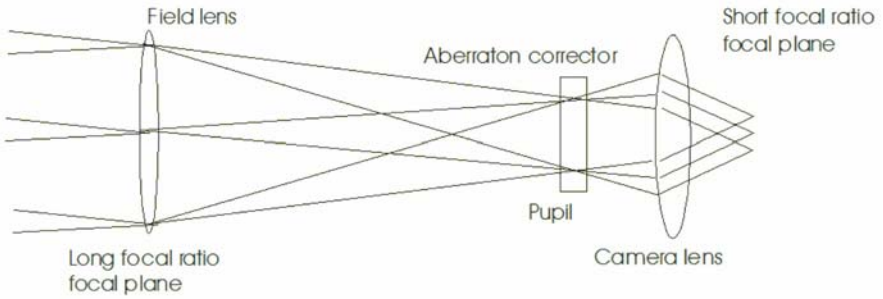

Figure 47: Sketch of a single unit of a Smart Fast Camera.

The "optical units" shown in Figure 47 may be grouped into SFC modules, each covering approximately a 1' FoV and containing as many units as detector arrays listed in Table 14. In order to re-image the whole 6' annular FoV, a matrix of SFC modules (Figure 48) will be used; the total number of detector arrays will be approximately 30 times larger than the numbers listed in Table 14.

The focal ratio of the input F/6 beam can be reduced by the SFC in a way to have different samplings on the science arrays. In Table 14 some options that take into account the pixel size and the final focal ratio are listed, considering a FoV of 1 arcmin. The final choice will also depend on a trade-off between complexity and cost. Anyway the SFC offers the possibility to cover a wide FoV for a 100m class telescope using a modular approach in which all the components are based on off-the-shelf technology.

F/#	Pixel size=12μm		Pixel size=18μm	
	Plate scale (milliarcsec/pixel)	Detectors array (over 1' FoV)	Plate scale (milliarcsec/pixel)	Detectors array (over 1' FoV)
3.3	7.5	4 × 4k×4k	11.3	9 × 2k×2k
2.5	10	9 × 2k×2k	15	1 × 4k×4k
1.5	16	1 × 4k×4k	24	1 × 2k×2k

Table 14: Detectors requested for a 1' FoV module in the Smart Fast Camera, for various combinations of focal ratio and pixel size. Note that the reported numbers must be multiplied by approximately a factor 30 to cover a 6' FoV.

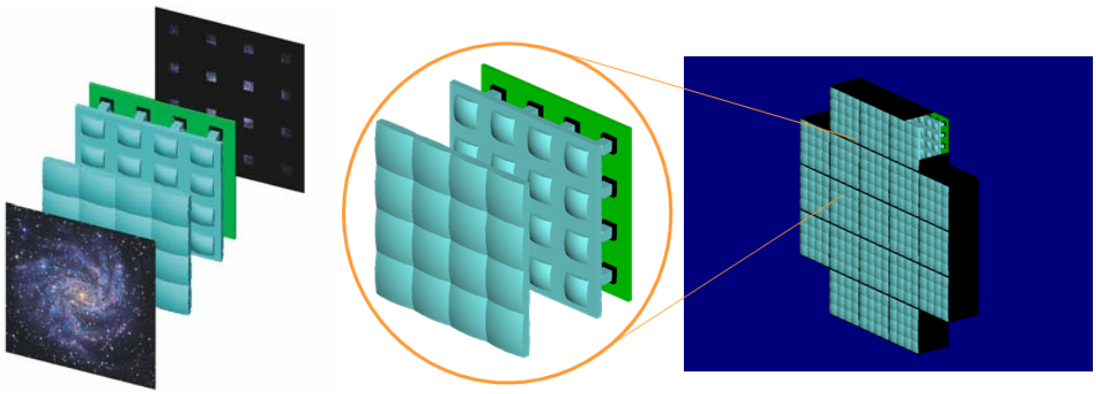

Figure 48: The picture on the left illustrates the SFC concept in which the light of a wide FoV is divided by a lenslet array. Each science array can be a 2k × 2k or a next generation 4k × 4k one and the total number of detectors depends on the chosen pixel scale. The figure on the right shows the modular approach in which a matrix of SFCs, each of them covering about a 1' FoV, re-images the whole 6' FoV, taking advantage of the similarity of the various modules to simplify the construction complexity.

8.1.4 Tolerances

In this section only the more relevant optical tolerances for the diffraction limited 1'arcmin FoV are presented. For the external FoV we only point out that the tolerances are much more relaxed according to the pixelsize, which will be finally adopted.

The optical tolerances of the focal enlarger are reported in Table 15. They correspond to a tolerable SR>0.8 (averaged over wavelengths and across the FoV). The Table reports the manufacturing tolerances on each lens and the alignment tolerances, which are the input for the mechanical design.

Element	Radius	Thickness	Wedge	Irregularity	Distance to next	Decenter	Tilt
L1	0.08%,0.18%	0.20 mm	27"	1.2λ, 1.2λ	0.20 mm	0.074 mm	32"
L2	0.02%,0.02%	0.08 mm	6"	0.4λ, 0.3λ	0.02 mm	0.008 mm	9"
L3	0.02%,0.08%	0.18 mm	6"	0.3λ, 0.3λ	0.20 mm	0.009 mm	6"
Aspheric	N/A	0.10 mm	30"	0.2λ, 0.2λ	0.07 mm	0.013 mm	78"
L4	0.02%,0.23%	0.04 mm	5"	0.2λ, 0.2λ	0.01 mm	0.004 mm	8"
L5	0.13%,0.02%	0.02 mm	19"	0.4λ, 0.5λ	0.02 mm	0.014 mm	15"
L6	0.22%,0.01%	0.02 mm	6"	0.5λ, 0.6λ	0.20 mm	0.005 mm	39"
L7	0.11%,0.23%	0.20 mm	36"	2.0λ, 2.0λ	N/A	0.200 mm	700"

Table 15: Optical tolerances. The two values reported for the radius of curvature and surface irregularity of each lens refer to the two surfaces. The surface irregularity is expressed as peak-to-valley at the wavelength λ = 1 μm. The last three columns report the positioning and alignment tolerances

All the so-called "axial" tolerances (curvature radii, lens thickness and air spacers) have been computed assuming as a compensator the back-focal distance of the focal enlarger, although this might not be the only choice. The wedge, irregularity, decenter and tilt tolerances have been computed assuming no compensator at all. It should be stressed that the decenter and tilt tolerances shall be fulfilled in every load and temperature condition. The tight alignment tolerances, related to the diffraction-limited optical

quality, actually impose the implementation of adjustment mechanisms for the alignment, otherwise it would be practically impossible to align the lenses just by mechanical precision. In order to keep the lenses properly aligned in every condition (without further adjustment), it shall be necessary to foresee some suitable mounting scheme. The simple differential thermal expansion or contraction between the lens materials and their mounts (assumed here to be aluminium) is enough to introduce unacceptable mis-alignment errors in most cases (except for L7 and, depending on the allowed temperature range, maybe on L1). A possible solution is the insertion between the lens edge and its mount of some pads of hard plastic material (e.g. 3 radial pads at 120°) with very high thermal expansion coefficient, which, despite their small thickness, compensate the differential expansion or contraction. For Delrin plastic (CTE$\approx 10^{-4}$), for instance, the optimal thickness of the pads ranges from a minimum of approximately 3.5 mm for the aspheric plate to a maximum of 46 mm for L7.

8.1.5 Feasibility of the optical elements

The materials adopted in the optical design of the focal enlarger for the 1 arcinn FoV camera are standard infrared materials, so their availability should not be an issue. The manufacturing tolerances on the curvature radii (and also some thickness and wedge) of the lenses are in general rather tight, but this is a consequence of the required diffraction-limited performance. A possible way to proceed in these cases is to manufacture the lenses, measure their curvature radii and thickness and re-optimize the optical design using as compensators not only the back-focal distance (or the position of the focal enlarger with respect to the input focal plane), but also some additional air spacers between the lenses: this will certainly allow the achievement of the required optical performance even with larger manufacturing errors than those reported in the tolerance Table 15. Those tolerances should be intended more as measurement errors on the final lenses: these errors, in fact, shall be compensated only by refocusing. Also some wedge tolerance may become more relaxed when the decenter and tilt adjustments (mentioned before for the alignment) are taken into account. Finally, the aspheric plate is an even asphere type surface with a maximum sag $\Delta z \approx 1.5$ mm and a reasonable size. Based on the experience of past design studies, where plates with similar aspheric surface but twice as big were designed, this plate should not represent an issue.

8.2 Wavefront sensing concepts

The concept that we depict here is a MCAO wavefront sensor which is capable to perform a mechanical derotation using a bearing (that, in some of the proposed possibilities, could be the rotator adapter which is in every OWL focal station) and able to use several reference stars to perform the correction. We mostly concentrate in solutions exploiting only ground layer partial correction (GLAO), even if possible designs for full MCAO correction are also envisaged. In fact, as already discussed in Sec. 5.1.2, due to the huge pupil superimposition for a 100m class telescope even at high altitudes, the partial correction of a GLAO system (but with ideas for extension to full MCAO) is particularly attractive because of the high contrast peak/halo anyway reached for such big diameters.

We distinguish between basically two classes of solutions, both based on a GLAO system using Pyramid wavefront sensors and Layer Oriented technique, but differing for the way the light co-addition is performed:

1. A system where the usable FoV is split into 6 or 7 portions, each of them feeding a MAD-like wavefront sensor where the co-add of the light is performed in an optical way (in the following Split LO-WFS);
2. A system in which the co-addition of the light coming from the references is performed numerically (in the following Numerical LO-WFS).

We analyse in the following the two proposed solutions, trying to identify advantages and disadvantages of both of them.

8.2.1 Split LO-WFS solution

As the FoV available for wavefront sensing is much larger than the isoplanatic patch, even in the most optimistic case, there are indications that, by grouping reference stars into areas of about such a size (from 20" to 40") would allow for novel algorithms to improve the MCAO performances. Moreover, this option still allows the conventional use of wavefront sensing in MCAO.

In such an opto-mechanical layout, hence, the field of view is divided into six radial coronal segments, each of them sending the light of the FoV to feed six MAD-like (optical co-addition of the light) or numerically coadded WFS, each having the possibility to use up to 8 reference stars. In the following we will describe the system based on the optical coaddition of the light.

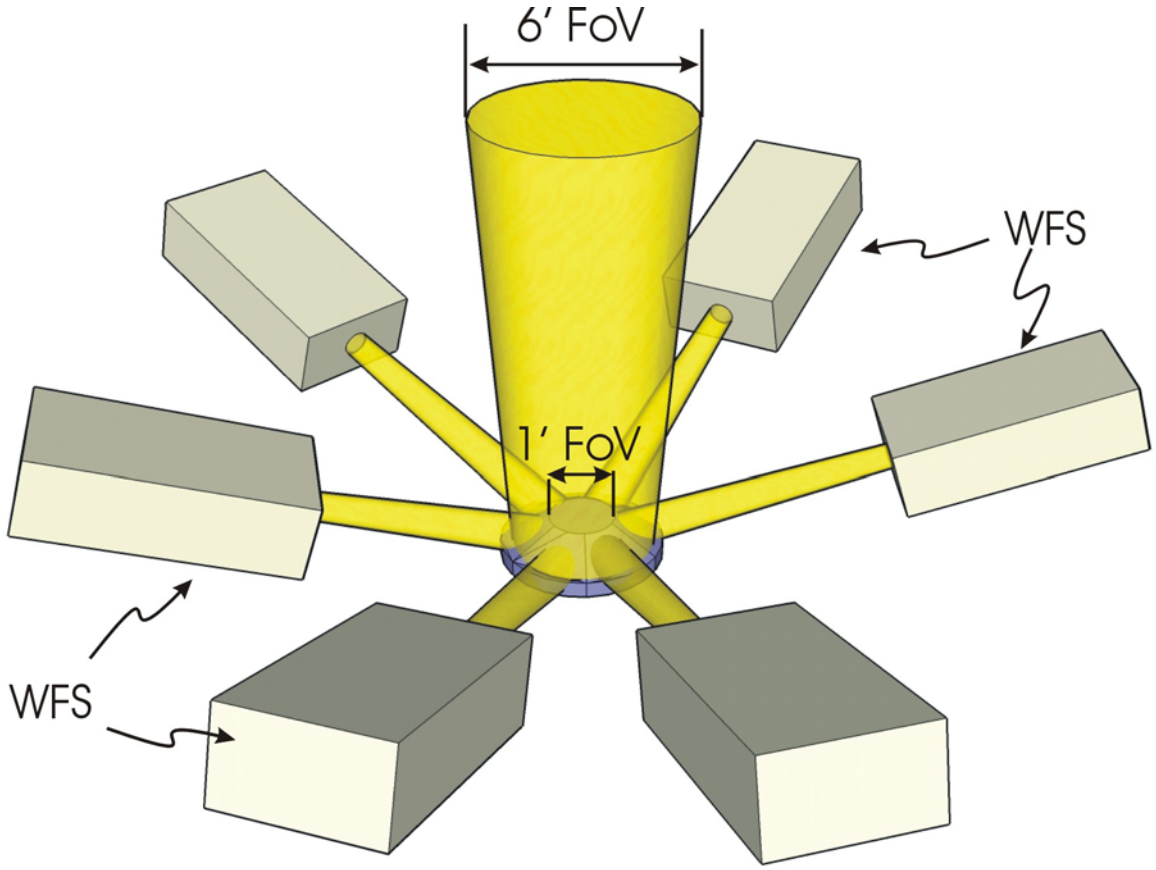

Figure 49: The figure sketch the split LO-WFS solution. A 6 faces prism reflects the entering circular 6arcmin FoV in to 6 coronal segments. Then each FoV portion is sensed by a MAD-like LOWFS (the boxes). In this solution the WFS take advantage of the same rotator adapter used for the scientific camera. The central 1arcmin is left unvignetted to reach the scientific camera in a solution where the wide field option is not implemented.

The split can be operated by using 6-faces reflecting Pyramid placed before the focal plane, which is in this way sending each portion of the FoV to a dedicated WFS, as shown in Figure 49. Each of the box shown in the drawing is a MAD-like WFS, with a maximum of eight star enlargers (RD3) moving in that

portion of the FoV to select the references. The star enlargers are composed by two lenses which have the task of increasing, individually for each reference, the focal ratio (and consequently the image size) of the incoming beam in front of the pyramids. This is done in order to reduce the dimensions of the pupils imaged on the WFS detectors, reducing the need to use huge and at the same time fast detectors (Figure 50).

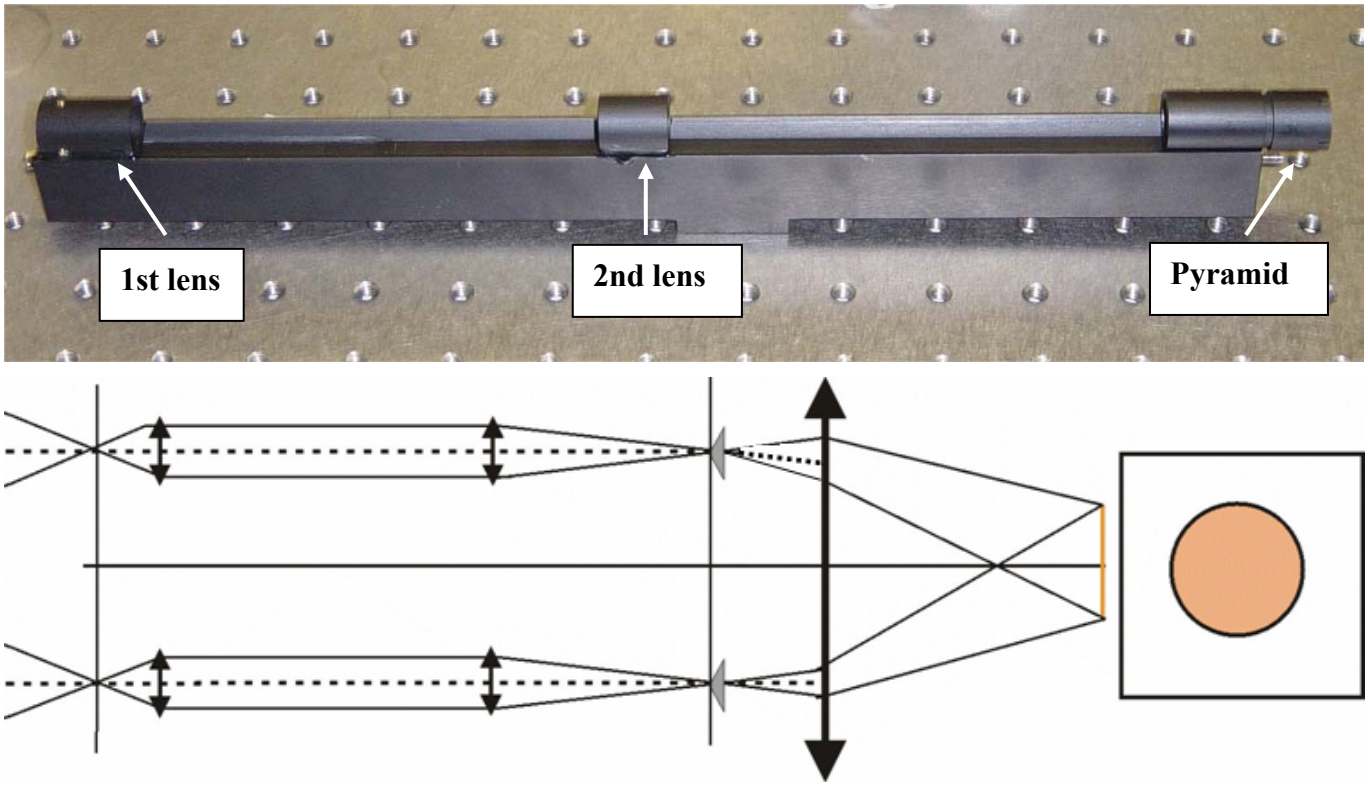

Figure 50: The star enlarger concept.

The movement of the star enlargers in the field for the references selection is performed by using 16 linear stages coupled in XY configuration, and the light collected by the star enlargers is re-imaged on the detectors by using two groups of pupil re-imagers. In Figure 51 the MAD system is described: in this case a beam splitter is needed to divide the light between two detectors, one conjugated to the ground layer and one conjugated to a certain altitude (8.5km in the MAD case) chosen in a way to minimise the residual of the turbulence coming from the upper layers.

We just note that, in the case of ground layer correction, only the detector conjugated to the ground is needed, simplifying the system shown in Figure 51 since there is no need of the beam splitter, of the pupil re-imager and of the detector conjugated to the high altitude layer. Each star enlarger produces, by the means of the pyramids, 4 images of the pupil on the detector. The six groups of four pupils coming from the 6 MAD-like wavefront sensors are finally numerically co-added in order to obtain the signal on the whole FoV to drive the ground layer DM.

An advantadge of this solution with respect to a common full optical coaddition stays in the possibility to treat numerically the 6-signals coming from the WFSs for the overall signal computation. In fact this solution leaves the opportunity to give ad-hoc weights to the different components of the overall signal according to the integrated brightness of the reference stars in each WFS, or to prevent anisoplanatism of the correction due to the lack of stars (or poor SNR) in one of the WFS. In this way the magnitude range for the reference stars limitation for stars selection is overcome, increasing the sky coverage.

We note that, in Figure 49, the pyramid which is operating the split of the light between the 6 wavefront sensors, in the central part (dimensioned in a suitable way) is flat and not aluminized, behaving in this way like an optical window which is transmitting the light of the central 1' of the FoV to the scientific camera (of course considering the case of the single narrow channel). This opens interesting possibilities to avoid using big dichroics sending the infrared light to the wavefront sensor, otherwise needed.

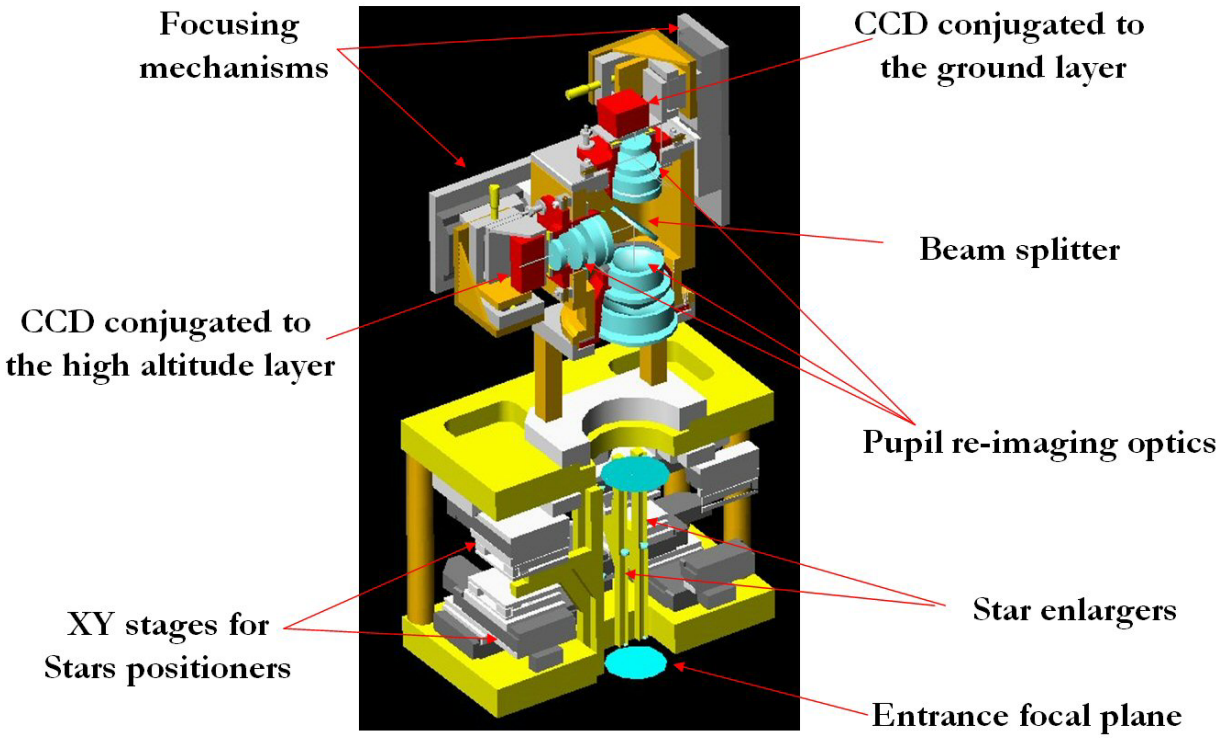

Figure 51: The Layer Oriented WFS for MAD. Similar WFS could be used to compose the optical split LOWFS option.

We also note that, in the proposed case, the WFS could use the full wavelength range. This possibility leads to the usage of an infrared detector, taking full advantage of the pyramid gain (RD1) or could anyway, by using proper detectors and achromatic design, increase the amount of light collected by the wavefront sensors.

Eventually, we present in Figure 52 an alternative opto-mechanical layout more compact for the same solution, i.e. the 6 MAD-like wavefront sensors scanning the external annular FoV while the central 1' is sent to the scientific camera. This solution simply differs for the direction of the beams folded to the 6 wavefront sensors, in this case oriented on the same side of the camera, having an overall final layout more compact. This can be accomplished by using the pyramid operating the light splitting in transmission instead of reflection. If chromatic effects will turn out to be a problem, an only reflecting light splitting can of course also be accomplished, as for example shown in in Figure 52 on the right side, where a reflecting pyramid is sending the light to a system of 6 mirrors which are then folding the light in the wished direction. Of course, the central part is flat (an optical window) in a way to transmit the light of the central 1' to the scientific camera.

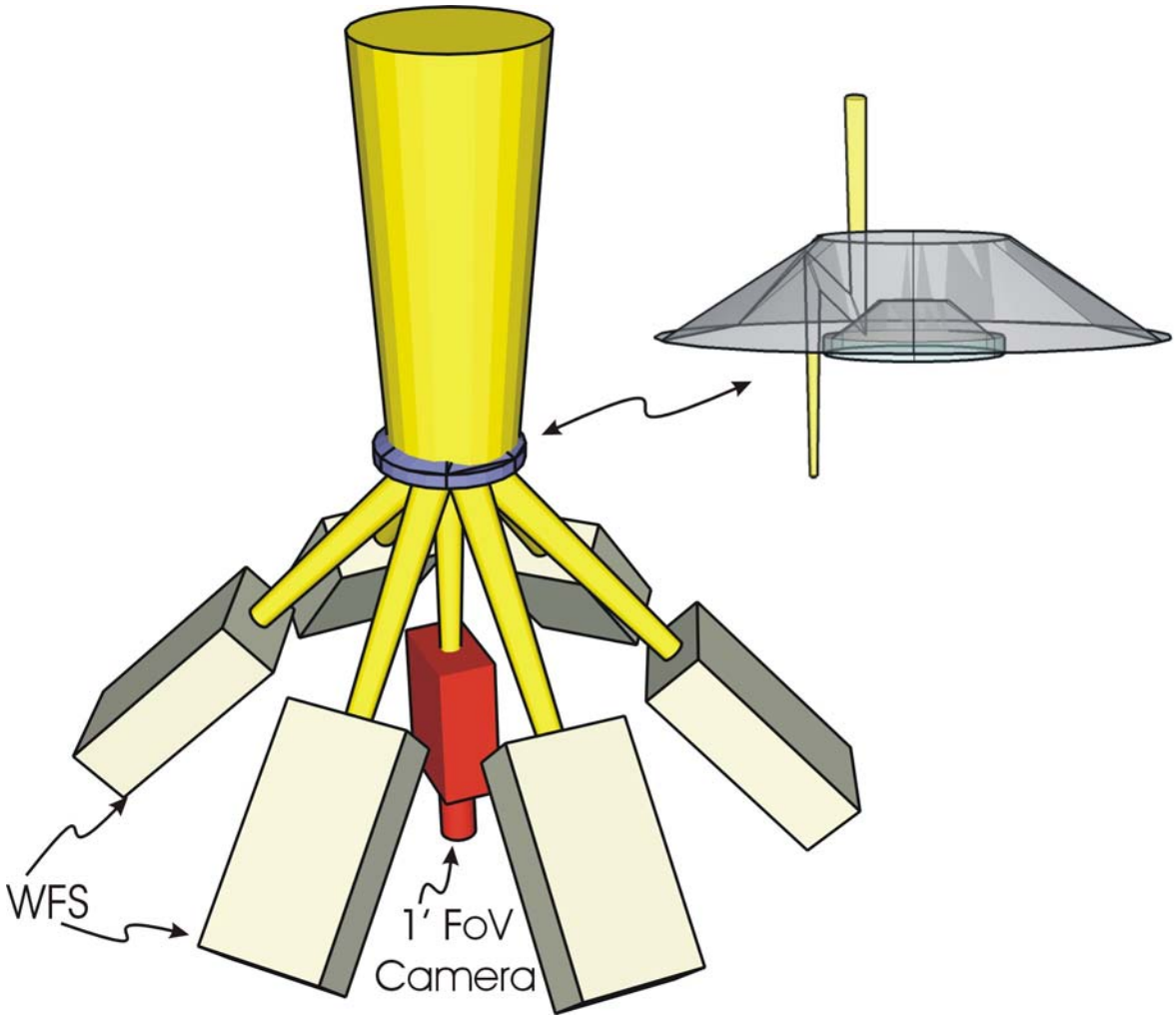

Figure 52: In the picture is presented a mechanical compact version of the split LOWFS solution, where the light in annular FoV (from 1' to 6') is used for WFS purposes while the central 1' FoV is used by the camera. In this arrangement the wide field option for the scientific camera is not considered. In the top-left inset a conceptual solution for FoV-split.

There are several alternative designs to the one just proposed, all based on the usage of 6 or 7 MAD like wavefront sensors individually using the optical co-add:

- The light which is passing through the central flat part of the pyramid in Figure 49 could be sent to another MAD-like wavefront sensor instead that to the scientific camera (see Figure 53). Of course in this case a dichroic separating the visible (to the wavefront sensor) and the infrared (to the scientific camera) is needed, but the additional WFS could be conjugated to a different altitude, having in this case a full MCAO system based on Multiple FoV technique and driving an additional DM. In this solution, both kind of scientific cameras proposed (the two channels one, wide and narrow, and the single 1' channel) can be used.
- There might be another opto-mechanical arrangment for a full MCAO MFoV solution whith the advantage of avoiding the usage of the dichroic and of a more compact optomechanical design, but applicable only to the case of the NARROW FoV scientific camera. Following the original scheme of the MFoV approach, one could conceive a design with three different FoVs: the inner one of 1' for the scientific camera, an annular ring from 1' to 4' for the WFS conjugated to the high altitude layer and a FoV from 4' to 6' for the WFS conjugated to the ground. In this way, there is no loss of light for the camera and the 2 detectors (each of them is looking to a different FoV) opening interesting possibilities to use an infrared detector or anyway to increase the amount of

light collected by the wavefront sensors using proper detectors, of course at the expence of a smaller FoV for each wavefront sensor.

- An alternative way to have a full MCAO system without using the dichroic is to consider the design shown in Figure 49, send the light of the central flat part to the scientific camera (which in this case must be the single 1' channel) but consider the 6 MAD-like wavefront sensors exactly like they are in MAD, i.e. with the beam splitters and the 2 detectors conjugated to different altitude. In this case, a Layer-Oriented system is obtained, and the six groups of four pupils coming from the 6 detectors conjugated to the ground are numerically co-added in order to obtain the signal on the whole FoV to drive the ground layer DM, and the same happens to the six groups of four pupils coming from the 6 detectors conjugated to the high altitude layer. Of course, in this solution, every detector of each MAD-like wavefront sensor receives 50% of the light. The fact that in the central part of the FoV the WFS is not using any reference is not a problem being the overlap of the pupils very high even for a high altitude layer, when considering a 100m telescope.

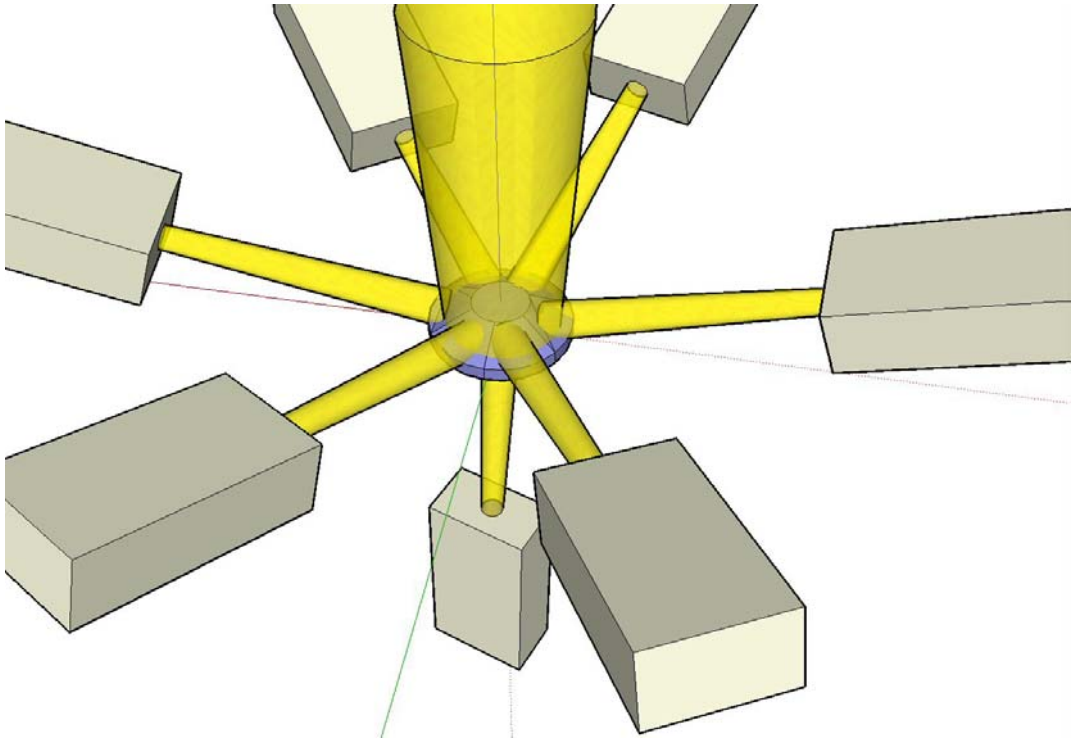

Figure 53: The Multiple FoV option for the proposed WFS. In this solution the WFS is opto-mechanically separated by the camera by a dichroic directing the visible portion of the spectra to the sketched WFS and the NIR to the scientific camera. This WFS solution can co-exist with the scientific wide field option.

PRO

- A much larger number of references can be used (up to 48, namely);
- Second order control loop is doable.

CON

- Because of the dichroic splitting (when needed), some disturbance is introduced in the scientific beam;
- Reaching the exact center of the FoV is hard so one has to accept a blind spot in the very center;
- Optomechanical complexity is rather large, but there are (as already mentioned) ideas to simplify the design and possibly to avoid the usage of the dichroic.

8.2.2 Numerical LO-WFS

In this solution a fully numerical GLAO system with a number (12 in the proposed case) of deployable sensors over the whole FoV is proposed. In Figure 54 a possible opto-mechanical layout for such a system is shown. The whole system, as already mentioned, is mechanically de-rotated by the means of a big bearing to compensate for the field rotation. The main constraints followed in developing this concept are:

- Maximum system flexibility
- To take advantage of L3CCDs or any future technology allowing close to zero RON CCDs
- All the FoV, including the central scientific part, shall be reachable to select possible references

The 12 movable sensors considered are pyramids, and each of them is individually coupled to a detector where, by the means of a small objective, they create four images of the pupil.

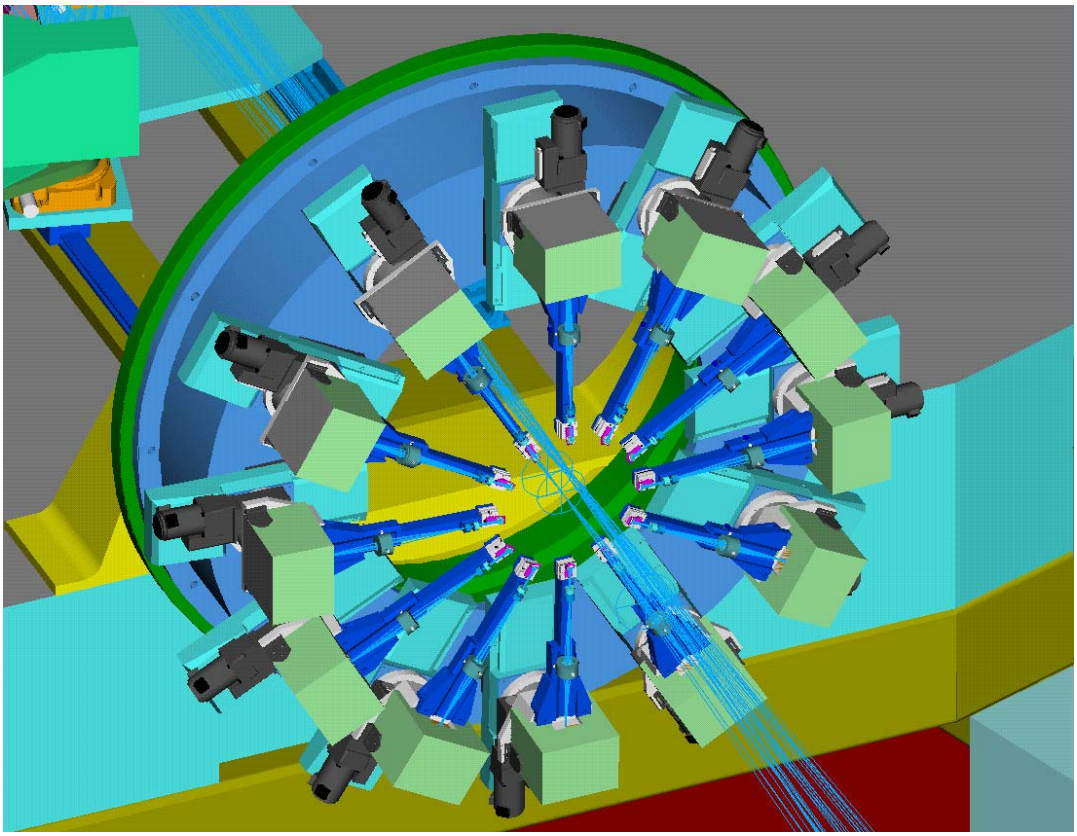

Figure 54: The Numerical Layer Oriented solution.

The light of all the pupils is than numerically co-added by the wavefront computer, in order to perform the wavefront sensing computation in the usual LO fashion. Every pyramid can be moved in a certain part of the FoV in order to be positioned on the reference stars. The movement is performed by using a linear stage coupled to rotator stages, and every pyramid can span about 1/6 of the complete FoV (see Figure 55).

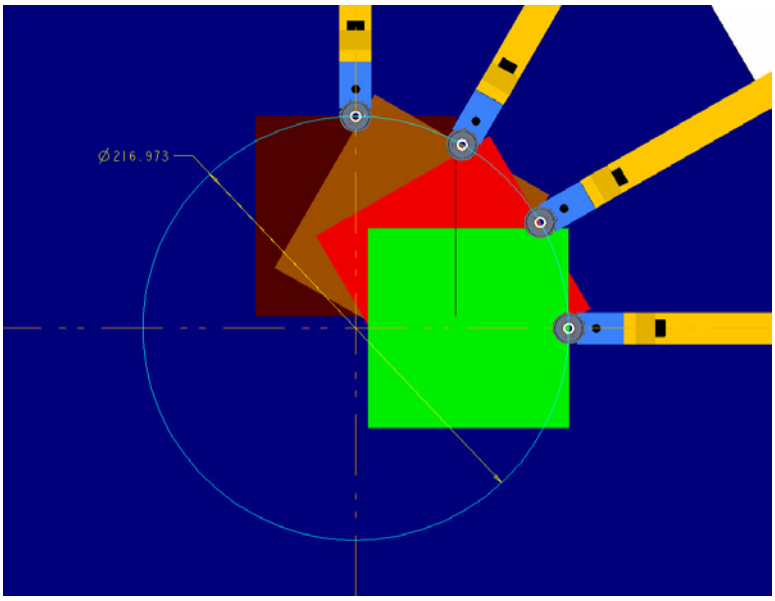

Figure 55: The area spanned by each individual pick-up system, of the order of 1/6 of the FoV.

The mixed linear-polar translation mechanism has been adopted in order to allow for movements of the probes till the center of the FoV without a too long arm (to minimise flexures of the latter). This will indeed introduce a differential rotation of the pupils, as seen from the detectors, but this fact can be treated numerically in the handling of the wavefront sensing data.

All of them can reach also the central position, in a way that in principle can allow to find suitable references even in the scientific FoV (the central 30") even if, when possible and/or needed, the references can be picked up only in the external annular part of the FoV (from 30" to 1'), leaving untouched the central part of the FoV used by the scientific camera. Of course, to minimise the space occupied by the moving systems, the solution presented here (see Figure 56) is using a pick-up mirror which is folding the light in the direction of the pyramid, after which is sent to the detector (the green box in the drawing) by the means of the objective.

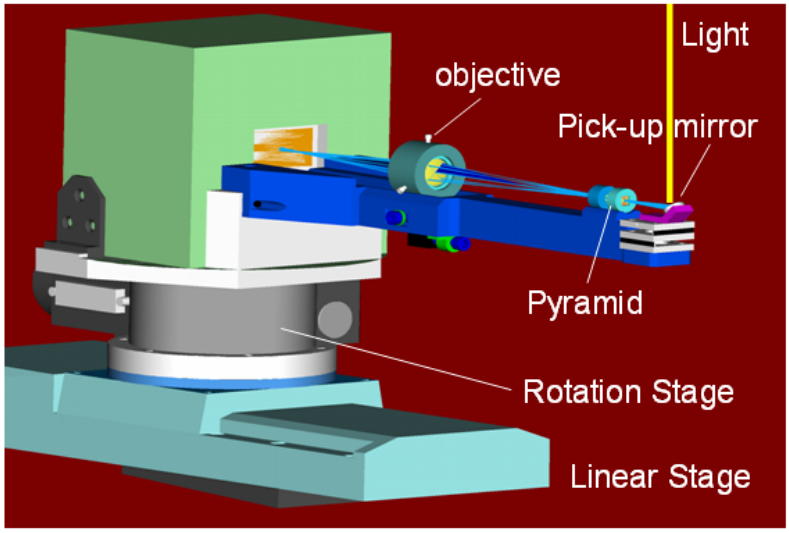

Figure 56: The positioning system for the pyramids in the Numerical LO-WFS case.

In case the pick-up system will be pushed inside the scientific FoV, there will be of course the vignetting of a part of it due to shadow of the moving arm. In case all the references are chosen in the external annular part of the FoV, there is no problem of vignetting but still their size will impose a limit to the minimum distance at which two references can be considered (which is of the order of 10-20 arcsec depending on the desired FoV of the pyramid).

Anyway, the moving arms must be as thin as possible in order to produce the minimum shadow on the scientific plane even if possibly (as already mentioned), in a number of cases, this will never interests the very central part of the FoV but only, marginally, the larger area interested by the faster camera.

Of course, care must be taken in avoiding possible collisions of the different pick-up system (see Figure 57) due to SW failures or to whichever error, and also in this case a MAD like system, where a collision detection system is implemented and properly working, could be used.

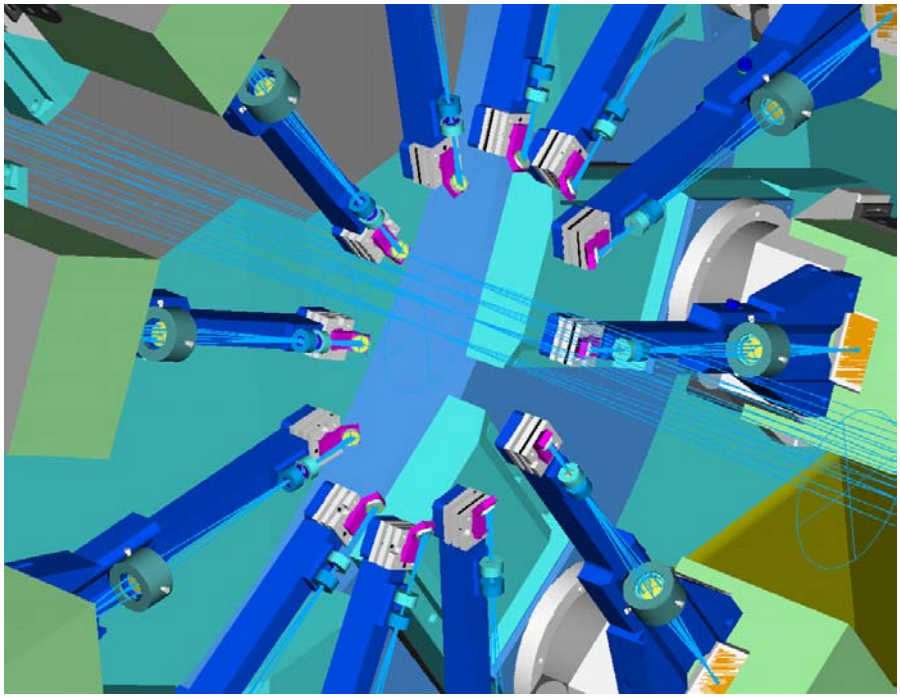

Figure 57: The crowding in the central area of the Numerical LO-WFS, where a collision might occur.

PRO

- Easy and "feasible today" opto-mechanical solution
- Every part of the FOV can be reached, including the very central one

CON

- There may be crowding problem in the FOV area, and this impose a limit to the maximum number of possible references to be used and impose the necessity of a detection collision control
- When the full FoV is used the density of the stars in the FoV is rather low
- When using references in the central scientific part of the FoV, there is an occultation of that reference and of a certain surrounding area, corresponding to the shadow on the field of the pick-up system arm.

8.2.3 General Remarks

- The average distance between uniformly scattered reference stars in the case SPLIT LO-WFS is about 23arcsec, while for the Numerical case is about 46arcsec. As typical figures for the isoplanatic patch are closer to the first estimate rather than to the second one, a more uniform sampling can be, in principle, achieved with the . However, it is questionable how these numbers of reference stars can be obtained far from the Galactic plane.
- Lower modes of correction (which are typical of the GLAO case), still favour the solution SPLIT LO-WFS, being of course the density of the faint stars much higher than the bright ones but allowing, in the case of faint stars, only low order correction.
- In the case of very faint objects, the not exactly zero RON of the detectors, as it is in practice the current situation for L3CCD, still favours slightly the solution of the SPLIT LO-WFS with optical co-addition of the light.
- In the numerical approach, given that there is enough margin in the movement of the pupil inside the sensitive area of the detectors, there is no a serious issue linked with flexures of the arms. We nevertheless point out that for a value of r_0 of about 330mm, still at least a 600×600pixels detector is needed. Note that for a SH with a one pixel band guard around each spot, a 1200×1200 detector is needed. Using the same technology of the Smart Fast Camera (RD2) for the WFS detector (see Figure 58) this translates into 5×5 or 10×10 of the existing 128×128 EEV detectors format. Assuming the newly developing 240×240 detectors the numbers drop down to about 3×3 or 6×6 detectors.

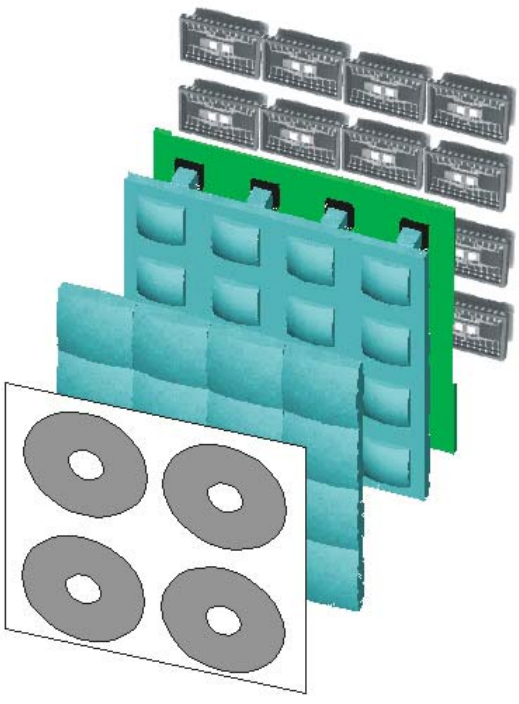

Figure 58: Splitting the FoV in order to use smaller size CCDs.

As some of the described advantages just discussed of the solution SPLIT LO-WFS depend on technological developments (RON close to zero) and some others deserve a deeper investigation, we indeed point out that the Numerical solution is certainly less complex from the opto-mechanical point of view and, a part from a smaller number of reference stars and for the Numerical co-add of the light, incorporates all the capabilities of the split LO-WFS case.

8.3 A possible mechanical arrangement

The mechanical structure of the camera is composed by a modular composite structure assembling the wide field channel, the so called Smart Fast Camera. The latter will incorporate on its entrance side the flange for the Rotator Adapter. The back of such a module can have the attachment points for a number of tubular trusses keeping within mechanical tolerances the rest, of the cryogenic structure, deploying the narrow field channel. In particular four sets of couple of tubular truss are linked to the final focal plane stations of the narrow field channel, while a similar set is constraining a circular structure keeping into position the folding assembly. This does include the pyramidic splitting of the beams after the first 1:2 relay, and the four foldings to keep reasonably compact the size of the whole instrument. The whole instrument has a small size with respect to the typical size of other 100m class instruments. While we show in the various pictures that this can be easily accommodated into the instrument bay we point out as a possible option the introduction of a further folding mirror, named M7 in the pictures, insertable through some sliding mechanics. This requires the duplication of the rotator Adapter unit above the foreseen one, but such a solution essentially retains the whole space available for instruments all deploying below the rotator adapter. With the proper choice of mechanical arrangement the NIR camera for OWL could, hence, be arranged as a sort of piggyback in the instrument bay of a larger instrument.

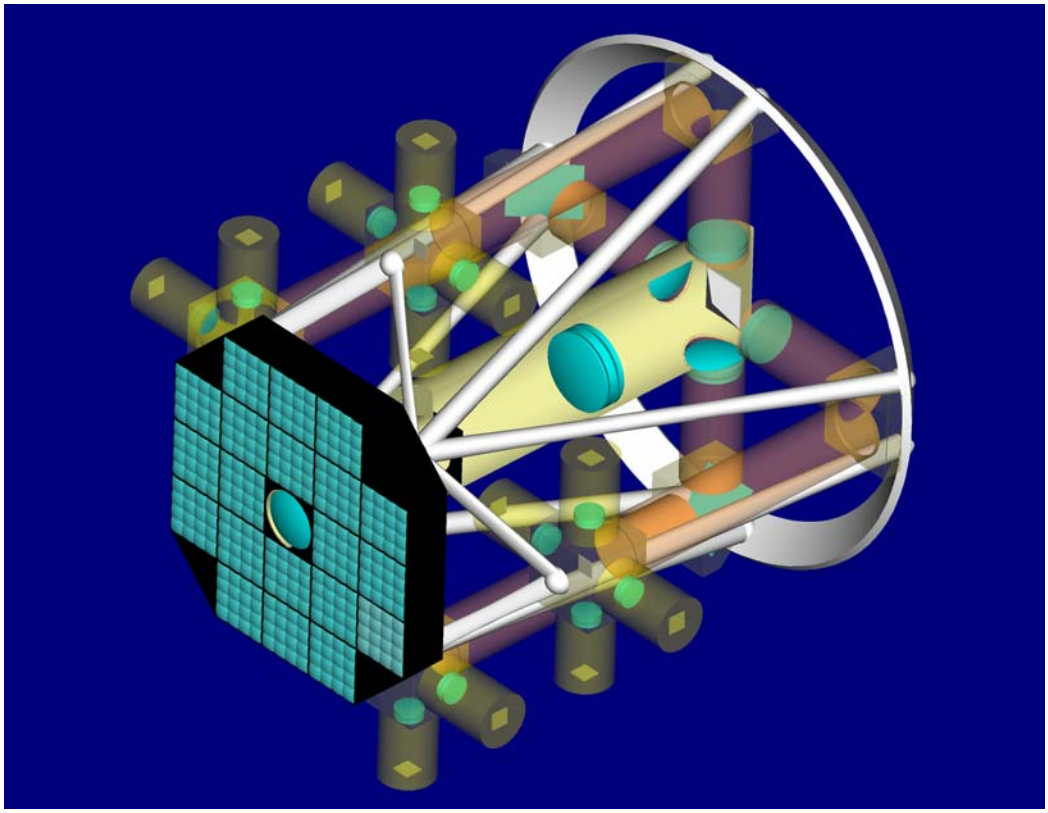

Figure 59: A possible opto-mechanical layout of the NIR Camera, including the two, wide and narrow, channels. The tubular trusses have the function to stiff the cryogenic tubes. Structurally speaking the weight is kept from such a truss in order to allow for maintenance the dismounting of sections of the cryogenic vacuumed sections.

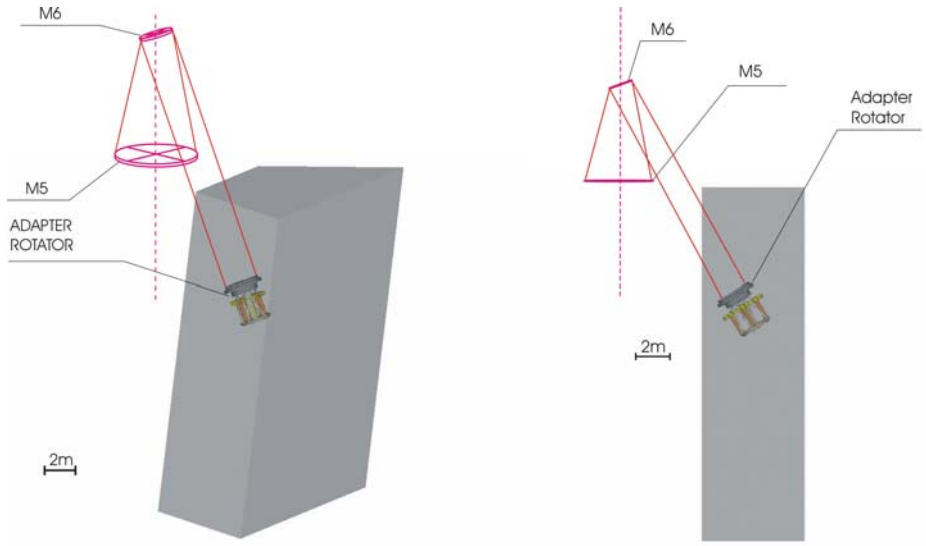

Figure 60 Left: Conventional accommodation in the instrument bay of the NIR camera. Right: A cross section of the conventional accommodation layout.

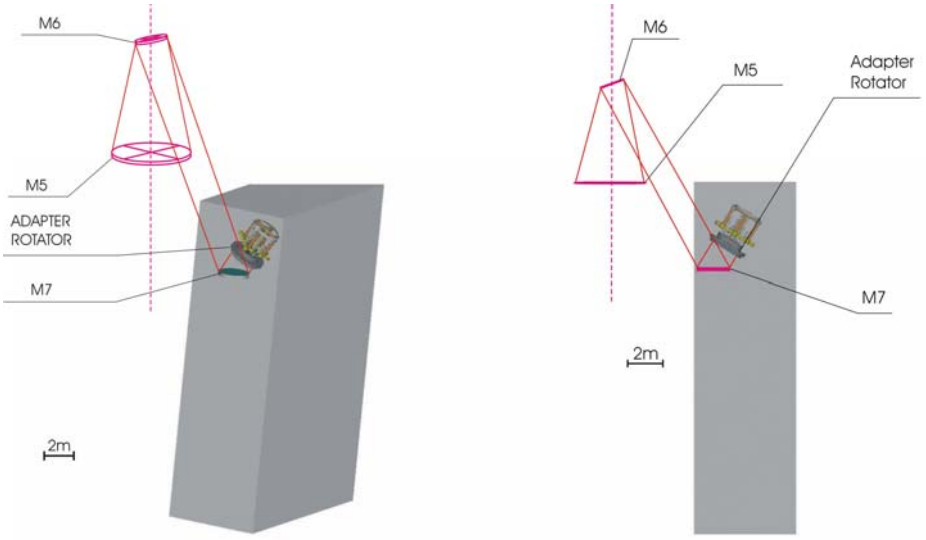

Figure 61: Adopting an insertable flat mirror (M7) the camera can be accommodated in a folded position still well whiting the volumes of the instrument bay allowing plenty of spaces for a major instrument, provided this will deploy all from the back side of the focal plane of the unfolded focal plane. On the left a 3D view, on the right a cross section.

The requirements in the mechanical accuracy of the derotation bearing and the precision of its movement are typical of any diffraction limited system as they do no tscale with the size of the telescope. Of course the weight and unbalance involved are the ones characteristics of this camera. As this is supposed to be covered by the derotator, part of the telescope structure, there is no a detailed study here. We just mention that custom-made available bearing and rotation systems, like the one developed by Maccon for the Linc-Nirvana, aboard LBT, equipped with DSM series motor (RD11), for derotation of the ground layer wavefront sensor, is almost suitable for the scope.

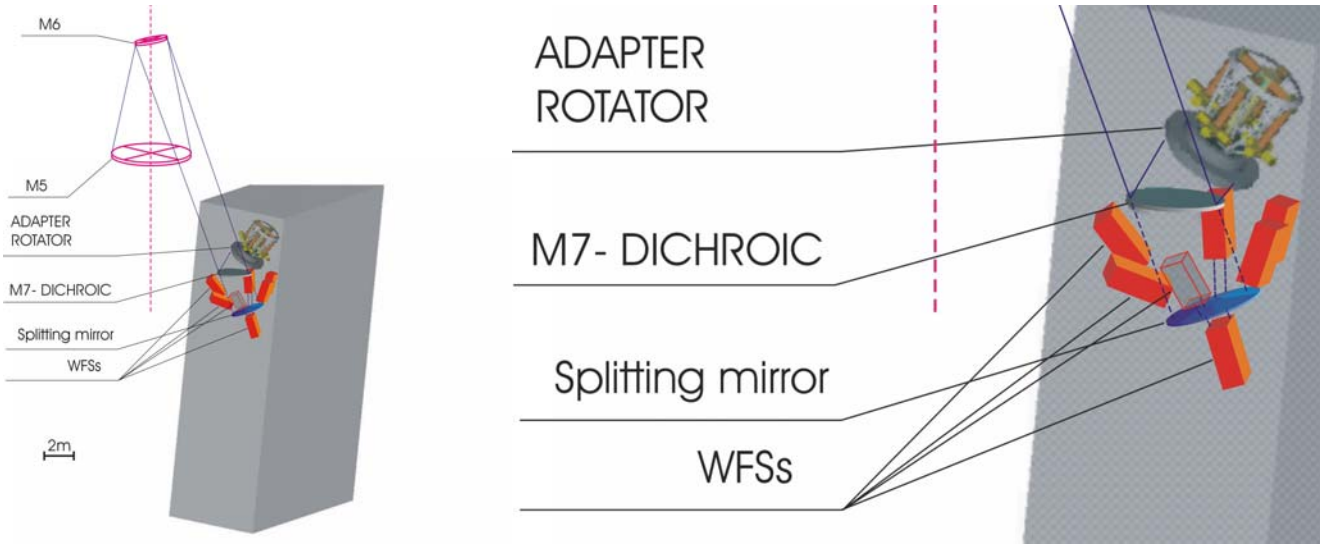

Figure 62: The figure shows a possible mechanical arrangement of the camera with the WFS, in the split LOWFS option. In particular here has been selected the MFoV option with the 7th WFS box at the bottom of the system. The light coming from the telescope is split in two parts: Infrared wavelengths up to the camera, visible light to the WFSs.

8.4 Atmospheric Dispersion Compensator

The obvious place to position the Atmospheric Dispersion Compensator (ADC) is where cold pupils are: emissivity is minimized because of cryogenic arrangement and we take advantadge of the not converging beam for optical design. Moreover this is an easy to design solution with respect to ones where ADC is much larger or it has to rotate with the field. One drawback is availability of glasses with such a relatively large diameter.

It is well known that ADC is a debated issue in the ELTs studies and is the subject of a number of forthcoming studies. Here we explore a number of different solutions that can leads possibly to a road map to establish a solution for such a problem:

1. Having ADCs only in the end of the trees, of course this will requires MORE ADC and in this case the solution has to take care of possibly further relative sources of mis-calibrations between the various arms;
2. Making ADCs in segment, each one covering portion pupil and not in the whole pupil. As the segments are not circular this implies one cannot make continuously variable ADCs, like counter rotating prisms. So one is faced with the option of having a big filter heel or a similar kind of mechanism able to intsert various ADCs in the pupil, each in fact, made up by several smaller ADCs each exploiting a fraction of the OWL pupil.

8.5 The star enlargers issue

The advantage of the Layer Oriented concept respect to the Star Oriented one is the possibility to use a great number of reference stars in the FoV and optically co-add the light into a CCD conjugated to a certain turbulence layer, making the fainter stars contribute to the wave front sensing. The light of each reference is collected by a dedicated star enlarger (RD3), simply a couple of lenses mounted in a tube that is moved into the field of view by two orthogonal remote guided linear stages, that magnifies the F/# of the incoming that is then split by a pyramid and by a field lens re-imaged into the CCD. The total superimposition of the pupils coming from all the references in the ground layer wave front sensing case risks to fail due to the star enlargers tilt coming from the introduced pitch and roll of the commercial and

even custom made stages during the star enlarger positioning. Taking into account 1/10 of rms pupil displacement for the ground layer overlapping for a 100mt class telescope the maximum tolerated pitch and roll are of the order of 1 arc second, strongly under the stages working accuracy. The idea is to use the WFS also for the active optics (RD4) part which consists in a slowly rate (respect to the adaptive optics) of star enlargers alignment that can be mounted over piezo-electric tip-tilt stages that assure fast and precise response to the inputs (Figure 63).

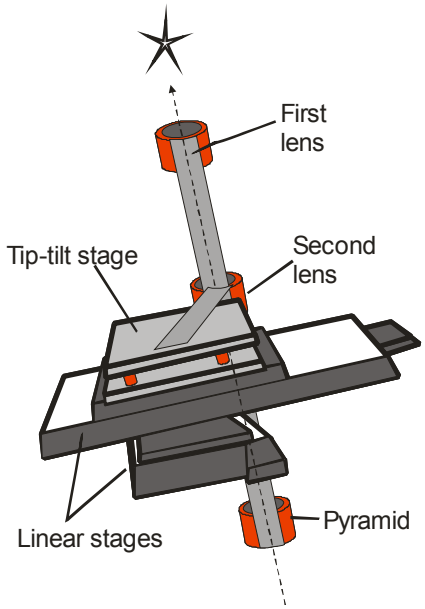

Figure 63: A star enlarger sketch with the linear stages and the piezo-electric tip-tilt stage

In the Figure 64 left it is simulated the footprint of the OWL pupils coming from all the pyramids, taking into account the central obstruction and the spiders. The tilt of the star enlargers causes pupils displacement. The pixels receiving light from all the star enlargers will experience only a light variation due to the poissonian noise, thus the intensity value will be almost constant. The border pixels instead will experience a higher signal variation, so a mask comprehending he pixels in the surroundings of the borders in order is created to have a sufficiently covering of the 4-pupil movements (Figure 64 right). The star enlargers are rotated respect to their axes with different frequencies, in this way the singles contributions of the different star enlargers to the metapupil shape can be computed and iteratively the process is repeated until the pupils displacement is reduced under the specifications.

Figure 64: A simulation of OWL metapupil (left) and the mask selection for the star enlargers tip tilt calculation and nulling (right).

9 Conclusions

As we just mentioned in the beginning of this document a camera for a telescope, whatever diameter is, is necessarily condemned to be used as a general purpose instrument. In order to establish the best position in the parameter space (field of view, pixel size, wavelgnth coverage), already severely constrained by the expected performances of Adaptive Optics and MCAO in particular, we have used a couple of scientific cases. One requires just a limited number of exposures. This allows us to assume that the camera is being used under particularly favourable atmospheric conditions and are expected to shed new light in star formation issues, especially expanding dramatically the kind of galaxies where such information will be extracted. In the second one, by far most risky and hard to precisely predict today, we speculate on the possibility to find out by direct detection the first stars shining in our Universe, a topic where only theroetical and controversial descriptions can be found in the literature. Again, dozens of other scientific cases could be found, and we sketched here just a further couple, without a through discussion, as a matter of example. Although such a camera could be assigned to an industrial Phase-A study within some time, we didn't base the design under the projection of technology development. However we indicated the areas where such development will makes a positive effect on the various designs depicted here. As explained in Sec. 8, infact, only moderate technological development has been assumed and only for some of the proposed concepts. Most of the ideas presented in this document, both for what is concerning the scientific camera and for what is regarding the MCAO wavefront sensor, can be realised with technology available today. Furthermore, most of the concepts concerning the MCAO system are based on existing systems or ongoing projects, in order to take full advantage on the experience already acquired based on them at the moment of the real final design. Dimensions of the optics and of the mechanical parts, required materials for the glasses, optical tolerances are indeed demanding but all comparable with the biggest systems available today. The field where are required the for sure efforts in Research and Development is the one concerning the detectors. Both in the camera design and in the wavefront sensor area, even if with different technical requirements, some technological improvements could lead to significantly different designs of both systems simplifying a lot their opto-mechanical complexity. In the field of the IR detectors, of course the need goes in the directions of smaller pixels with bigger size CCDs, but also improvements in the cooling systems (above all in their dimensions) could lead to significative changes in the design of the scientific camera. In the field instead of the wavefront sensors, bigger chips with fast integration times and low RON (possibly nearly zero) are the parameters where improvements are clearly needed, even if not necessary. In fact, we emphasize again that several proposed ideas are based on technology existing today, of course paying the price of a more complex opto-mechanical layout.

Once the preliminary feasibility of such an instrument is, we believe, established the road-map for further development consists into choosing a baseline design, also in connection with the studies on OWL about the MCAO concept to be preliminarly adopted and to carry out a detailed optomechanical study. The cryogenic part, although relevant, is not more complex than several already existing instruments, even for 4m class telescopes! This will allow establishing a detailed assessment of the hardware cost, manpower and overll time required to turn into reality this instrument. A possible precursor instrument for VLT can only be indivduated, here, on the wide field channel, eventually extending to the visible wavelegnth side. This option, although mentionable, is no longer discussed here.

As a final remark we should point out that the wide channel side could in principle exploit novel Adaptive Optics approach, at the moment of writing only in terms of development, and hard to predict in a safe manner, allowing for a limited Strehl but concentrating the energy in a core of size significantly larger than the diffraction limited spike allowing, in principle, to extend the sky coverage to even further faint magnitudes.

10 APPENDIX

10.1 The theoretical tool for deriving SFH from CMD

Simulated CMDs corresponding to a star formation history akin to late type galaxies are shown in Figure 65, with the different colours encoding the different age range of the stars (see legend in the right panel). The CMD in the left panel corresponds to a total astrated mass of 2.3×10^7 M_{sun}, and a total mass currently in stars and remnants of 1.7×10^7 M_{sun}. The different evolutionary phases can be distinguished: the Main Sequence (MS) with stars in the core Hydrogen burning phase; the Horizontal Branch (HB), the Red Clump (RC) and the Blue Loop (BL), with respectively low, intermediate and high mass stars in the core Helium burning phase, but different age ranges; the Red Giant Branch (RGB), where stars older than 1-2 Gyr evolve while burning H in a shell, and the Asymptotic Giant Branch (AGB), with stars in the double shell burning stage. It is worth to note that in the NIR the cool portion of the CMD is much brighter (about 4 mag) than the MS region. This is because during the evolution, stars with low and intermediate mass get much brighter than on the MS. Therefore, although the star counts on the MS are an important diagnostic of the SFH, at a given level of limiting magnitude much longer look back times can be probed in the evolved portion of the diagram. Analysis of this portion of the CMD yields valuable information on the Star Formation History throughout the galaxy lifetime.

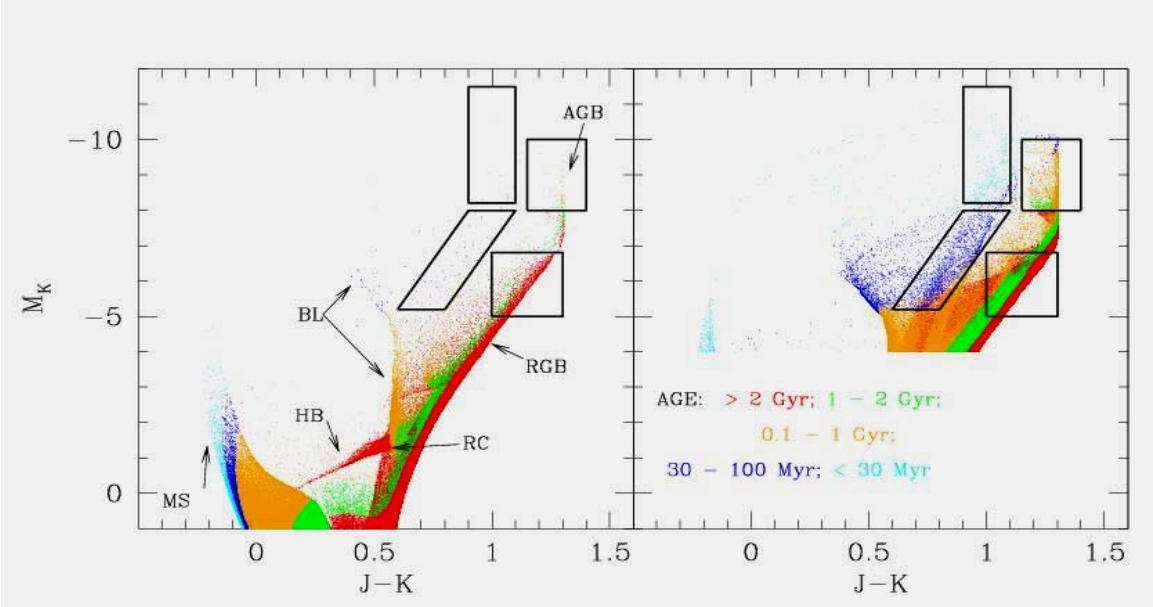

Figure 65: Synthetic CMDs of stellar populations with an age and metallicity distributions akin to late type galaxies. The simulations correspond to a total stellar mass of 2.4e+07 M_0 (left panel) and of 8.4e+08 M_0 (right panel). Only the stars brighter than M_K=-4 have been plotted in the right panel. The colour encodes the star's age, as labelled in the right panel. The diagnostic boxes over plotted are meant to sample different age ranges.

Massive stars have short life and are disadvantaged by the IMF: as a consequence they appear poorly sampled in the CMD if this corresponds to a too low total stellar mass. The right panel of Figure 66 shows a CMD with the same SFH as the one in the left panel, but relative to a total mass in stars and remnants of 8.4×10^8 M_{sun} It can be noticed that with this sampling the upper Main Sequence appears

populated in the CMD, and the various branches in the evolved portion of the diagram are much better traced.

It is possible to derive a thick brush picture of the SFH in a stellar system from star counts in selected diagnostic regions on the CMD (see Figure 65). To do that it is crucial to establish how well the stars falling in the different regions separate in age. In Figure 66 we show the age distribution of the stars belonging to the simulation shown in the right panel of Figure 67, which fall in the 4 boxes. The four boxes appear essentially populated with stars belonging to different age ranges: the stellar counts in each box will then be proportional to the mass transformed into stars within different time intervals during the galaxy lifetime.

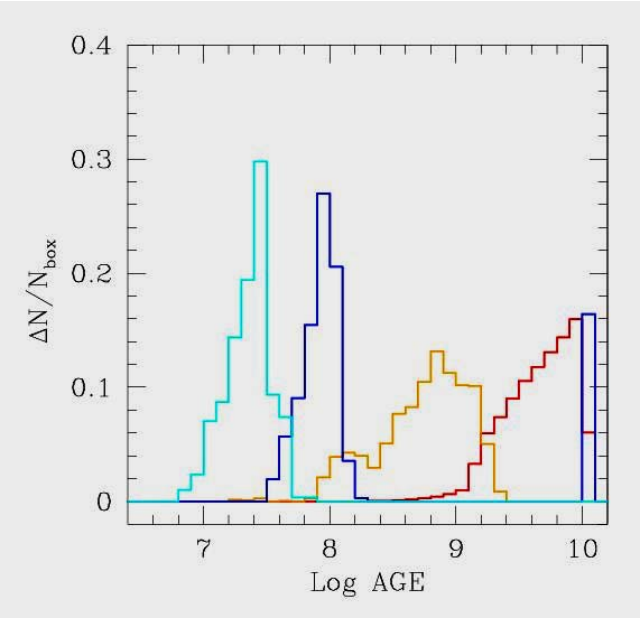

Figure 66: Age distribution of the stars sampled by the 4 boxes drawn in Figure 65. The line colours relate to the box: cyan refers to the top-left box, blue to the bottom left box, orange to the top right and red to the bottom right box.

We will thus derive the average Star Formation Rate in four (wide) age bins by applying the relation:

$$\Delta N_j = M < \delta n_j >$$

between the stars counted in the box j and the mass in stars of the parent population. To do that we need the quantity $< \delta n_j >$, which is the average of the specific production of objects in the *j* box with a single age and single metallicity stellar populations (SSPs), where the average is performed over the relevant age and metallicity range.

In Figure 67 we show various sets of isochrones (taken from Girardi et al., 2002) for 6 different values of metallicity Z, with superimposed the diagnostic boxes. It can be noticed that, due to the systematic reddening of isochrones with increasing metallicity, the boxes do not always target the same range of stellar ages.

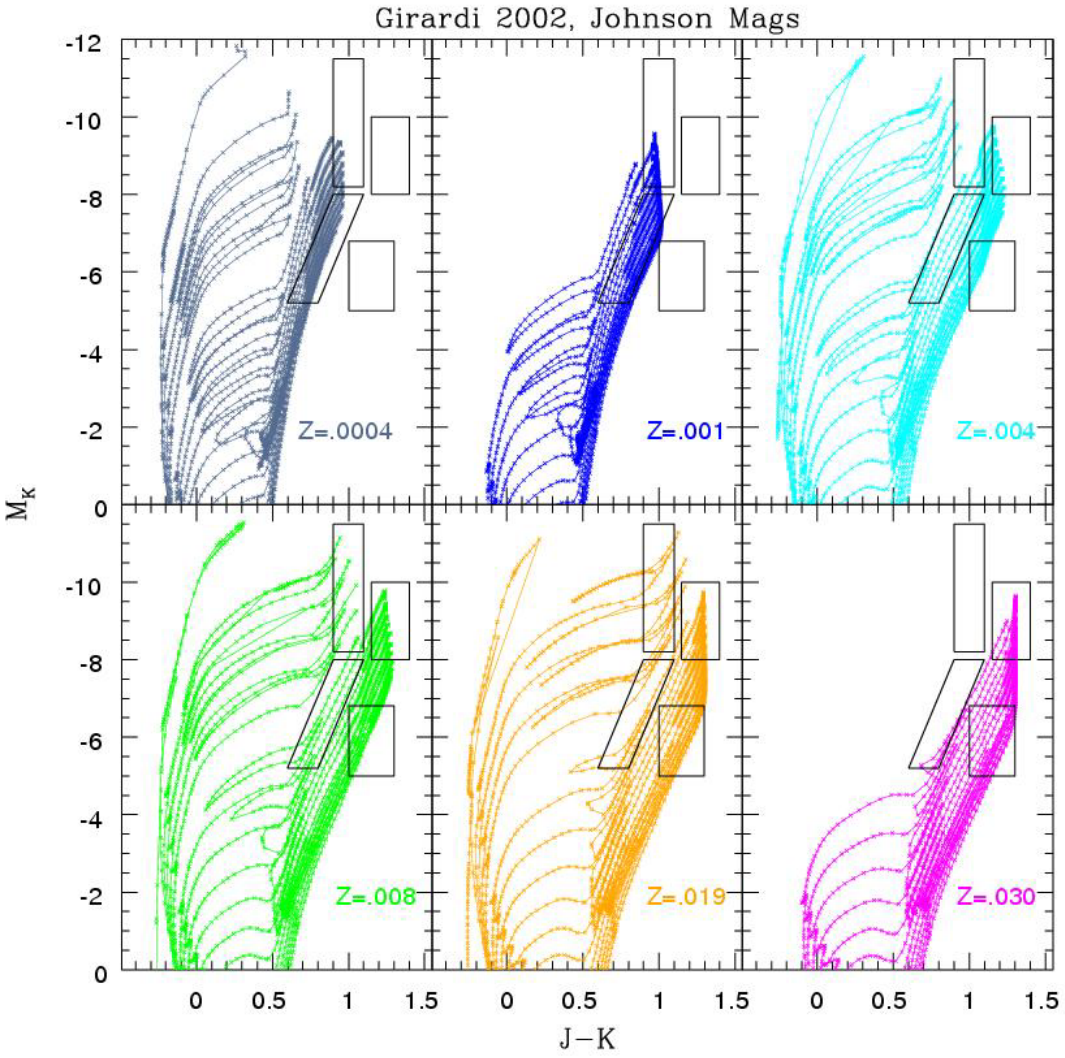

Figure 67: Sets of isochrones in the plane K, J-K for different stellar metallicity (Girardi et al 2002). The plotted isochrones span a range in age from 4 Myr to 10 Gyr, except for Z=0.001 and 0.03, in which cases the youngest isochrones are 63 Myr old. Depending on the metallicity the boxes intercept different ages.

In particular, for metallicities larger than Z=0.008 (0.4 of the solar value) the four boxes Sample the same evolutionary phases, i.e. Red Supergiants in the upper right, AGB stars in the upper left, RGB stars in the lower left and high mass core Helium burners in the slanted box. As a consequence, also the ages sampled will be similar irrespectively of metallicity. The situation is markedly different at low metallicity, with AGB stars falling in the bright and blue box, and RGB stars in the slanted box, while the two red boxes appear not populated at all. This is the consequence of the property of evolutionary tracks to be bluer for lower metallicity. The intermediate metallicity Z=0.004 (1/5 solar) exhibits intermediate properties. Therefore there is a non trivial dependence on metallicity of the age range sampled by the four boxes. This characteristic introduces an intrinsic limitation on the method of reconstructing the SFH from the analysis of the CMD.

In Figure 68 we show the specific productions of SSPs of various age and metallicity in the four diagnostic boxes. The colour encodes the metallicity as in Figure 67. The upper left panel shows the specific production in the faint red box; it can be seen that this box is essentially populated with stars older than about 2 Gyr, and that this is the case only for metallicities greater than Z=0.004 approximately. The upper right panel shows the specific production in the bright red box: indeed the box samples stars with ages between 0.1 and 2 Gyr, again provided that the metallicity is large enough. Young stellar

populations with solar metallicity also produce stars in this box, but they do so with a very modest efficiency. The lower left panel relates to the bright blue box, meant to target the most recent star formation. As anticipated, this box collects young stars with high metallicity (orange and green lines), and intermediate age stars with low metallicity (blue and grey lines). Due to the progressive enrichment of the interstellar medium during the galaxy evolution, it is expected that only very old stars do have such low abundances. It follows that in real galaxies there should not be a sizeable population of intermediate age and low metallicity stars, at least for non Dwarf galaxies. Therefore the stellar counts in this box should reflect the most recent star formation. Finally, the lower right panel shows the production within the slanted box, meant to target intermediate age stars in the core Helium burning phase. Again, we notice that this box samples both intermediate and old ages: the high metallicity isochrones provide stars with ages between 30 and 150 Myr, approximately; the low metallicity isochrones contribute stars older than 0.5 Gyr, down to the age of the galaxy. This contribution will always be present, since the oldest stars are presumably of low metallicity, and its size will depend on the chemical enrichment history of the galaxy. Indeed, the fact that this box contains old stars is apparent in Figure 66 as a blue bin at ages between 10 and 12 Gyr.

BOX	AGE RANGE	$< \delta n_j >$	Notes
RGB: faint red	from 2 to 12 Gyr	5.4×10^{-5}	Average over whole Z range
AGB: bright red	from 0.1 to 2 Gyr	1.7×10^{-5}	Average over whole Z range
RSG: bright blue	from 0 to 0.04 Gyr	6×10^{-5}	Average around Z_{sun}
HeB: slanted	from 0.03 to 0.15 Gyr	1.7×10^{-4}	Average around Z_{sun}

Table 16: Average specific productions and sampled age ranges of the four diagnostic boxes have been listed.

The ratio between the stellar counts in each box and the mass of the parent stellar population is the weighted average of the specific productions, according to the age and metallicity distribution of the stellar population. When applying this method to a real galaxy such distribution is not known a priory; as a first approximation we consider the specific productions averaged over a flat distribution of age and metallicity. For each box we list in Table 16 the sampled age range and the average specific productions used in this exercise. Roughly, we expect to count 5 star in the faint red box per 10^5 M_{sun} of stellar population with age older than 2 Gyr; 2 stars in the bright red box per 10^5 M_{sun} of stellar population with age between 2 and 0.1 Gyr; 6 stars in the bright blue box per 10^5 M_{sun} of stellar population with age younger than 0.04 Gyr; 2 stars in the slanted box per 10^4 M_{sun} of stellar population with age between 0.03 and 0.15Gyr.

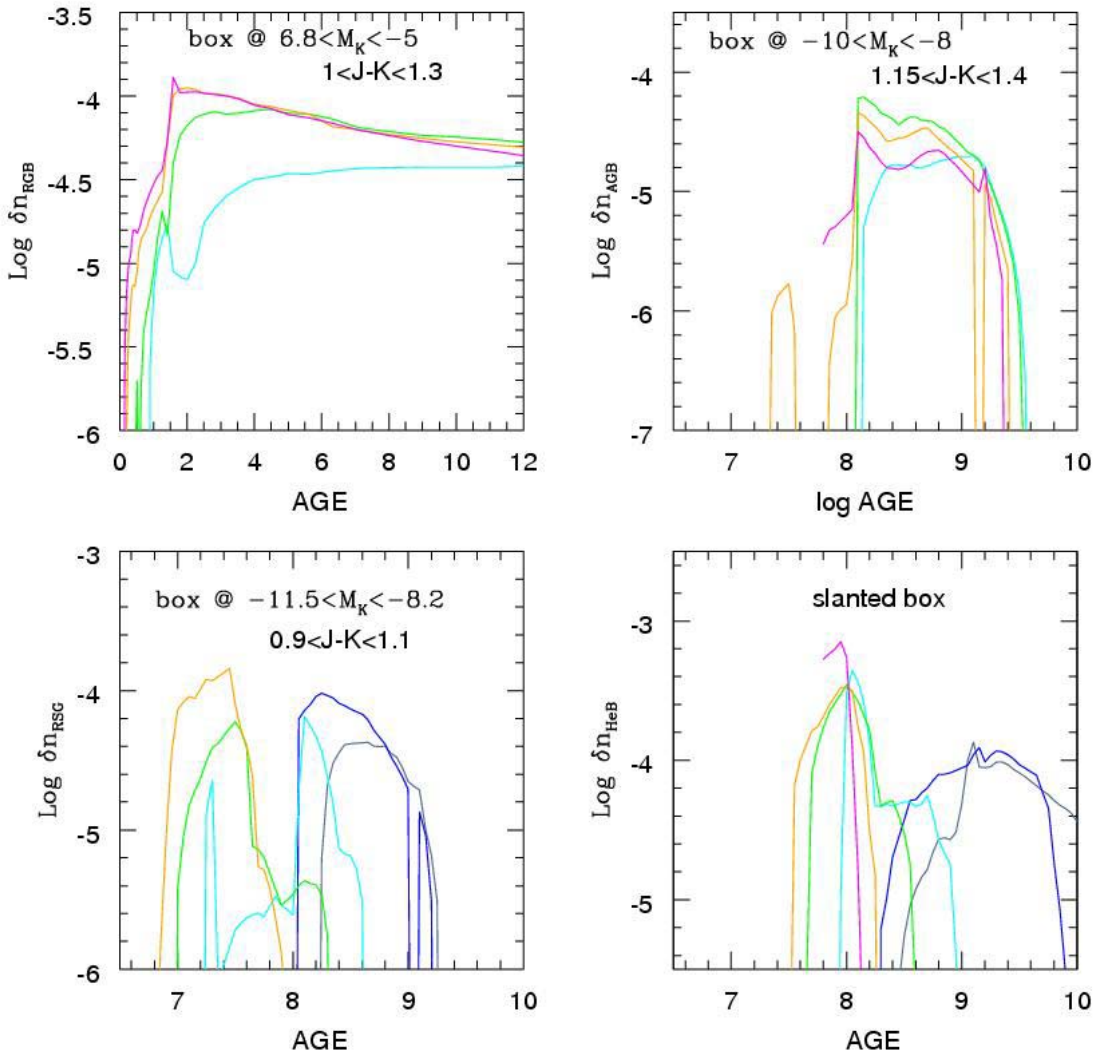

Figure 68: The specific production of SSPs of various metallicities, in the 4 selected diagnostic boxes, plotted versus the age of the SSP.

10.2 Sky-coverage for ONIRICA

In this section the sky-coverage study for ONIRICA will be presented. The results obtained are based on the real data collected analyzing the star information in the USNO-B catalogue RD6. Using this catalogue it is possible to retrieve the R (0.7μm) magnitude of the reference stars and to avoid the use of extended source (as galaxies) in the computation.

In this catalogue are listed the objects identified by scanning plates taken in the last 50 years by different observatories. These data cover all the galactic latitudes and longitudes and the catalogue gives information about positions, proper motions, magnitudes in various optical pass bands (B, R and I), and a star/galaxy estimator for more than 1 billion objects. This catalogue has an accuracy of about 0.2 arcsec for astrometry, 0.3 arcsec in photometry and 85 percent in star/galaxy classification. It is supposed to be completed until the magnitude 21 in the V band. However the study we are presenting refers to the R band only and we checked that the catalogue presents lack of data for stars fainter than 19th magnitude in this band (see Figure 69).

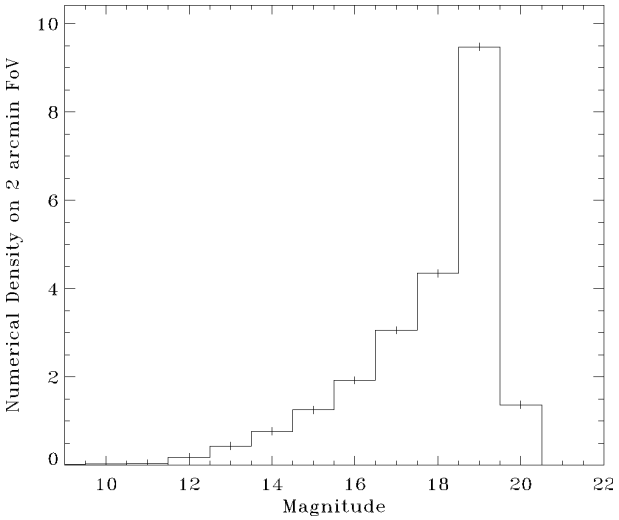

Figure 69: This histogram shows the distribution of the numerical density of the stars in the catalogue with respect to the magnitude in the direction of the Galactic anti-center. The numerical density represents the average number of stars over 2 arcmin FoV for each unit magnitude range. It is clear that the catalogue is not complete for stars fainter than 19th R-magnitude.

Here we assumed that the WFS use only Natural Guide Stars (NGS) as references. Another important issue taken into account is the availability of 0electrons Read Out Noise (RON) CCD, such as L3CCD.

Ground Layer Adaptive Optics (GLAO) and MCAO corrections have been taken into account:

AO correction	DM number	FoV	# Star	R Mag range	AO mode
GLAO	1 @ 0km	4arcmin	3,6 & 12	14-21	Numerical LO/SO
			18	Δ=3.5	Optical LO
MCAO	2 @ 0km-high	4+2arcmin	3,6 & 12	14-21	Numerical LO/SO
			18	Δ=3.5	Optical LO

Table 17: In this table the characteristics of the WF sensing system considered for the sky coverage analysis.

In this analysis we consider different galactic latitude cases at 50 and 90 degrees and two scientific relevant cases in the direction of the Virgo and Coma clusters:

- 2×2 degrees at 90°;
  - North Galactic Pole
  - South Galactic Pole
- 2×2 degrees at 50° at opposite direction of the sky:
  - b = 50, l = 90 deg;
  - b = -50, l = 270 deg;
- 2×2 degree on Coma Cluster at J2000=12:59:48.7 +27:58:50;
- 2×2 degree on Virgo Cluster at J2000=12:26:32.1 +12:43:24

In the following sections are presented the results relative to the selected case. It should be notice that here the computation the distribution of the reference stars over the field has been considered: in fact in order to perform a useful correction the reference stars have to be arranged around the scientific Field of View, otherwise the correction performed could be directed on a region outside the Scientific FoV. The stars should be arranged in different quadrants of the field in order to avoid strong anisoplanatism of the correction. Because of this reasons we considered the additional constrain that the barycenter of the

reference stars has to stay in the 2arcmin FoV centered in the on-axis direction. For the LO case with numerical coaddition we compute the barycenter weighted for the brightness of the reference stars.

10.2.1 GLAO sky-coverage

For the GLAO correction we assume adaptive systems using reference stars on a 4 FoV centered on the telescope on axis direction. The GLAO Star Oriented and GLAO Layer Oriented approaches are conceptually very similar in their basic definitions. Moreover using CCD with Zero Read Out Noise (RON) the Star Oriented and the Numerical Layer Oriented disadvantage of having as many sources of noise as many reference stars is avoided. However should be stressed that the optical coaddition advantage to use less WFSs (as many conjugation altitudes) still remains.

So we analyzed the optical coaddition mode with at most 18 reference stars and the Numerical Layer Oriented/Star Oriented approach with different number and limiting magnitude of the reference stars.

10.2.1.1 Layer Oriented Optical coaddition

In the optical coaddition has been evaluated if the barycenter of the selected reference stars weighted for the relative intensities (in photons) stays in a 2arcmin circle on axis. In principle in this case there is no limitation on the brightness and the number of reference stars, but 20 is a reasonable number for the references and 21st the limit magnitude given by the catalogue. A limiting difference of 3.5 Mag has been considered.

- **North Galactic Pole**

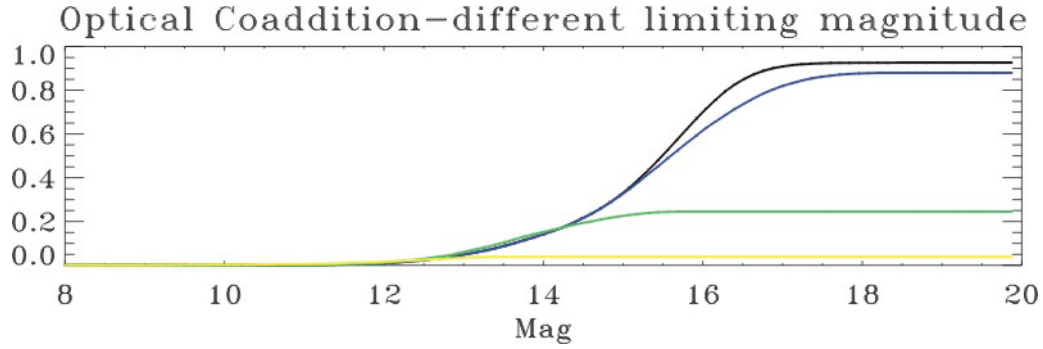

Figure 70: North Galactic Pole coverage for optical LO - GLAO approach. Here have been considered the different limiting magnitudes for the single reference stars and at most 18 reference stars over the 4arcmin FoV. The different lines colours represent different limit on limit magnitude of each reference stars: 15, 17, 19.5 and 21 going from the bottom to the top. Sky coverage is plotted in ordinate and it goes from 0 to 1. A system with a 15th magnitude limit for the brightness of the reference is useless.

Integr. / Single Star	14	15	16	17	18	19
21	0.152/0.419	0.331/0.692	0.700/0.786	**0.909**	**0.926**	**0.926**
19.5	0.152	0.327	0.616	**0.819**	**0.877**	**0.880**
17	0.152	0.226	0.245	0.245	0.245	0.245

Table 18: Results relative to North Galactic Pole. Values go from 0 to 1. 4armin FoV has been considered. In bold style the sky coverage values greater than 0.75 have been written.

- **South Galactic Pole**

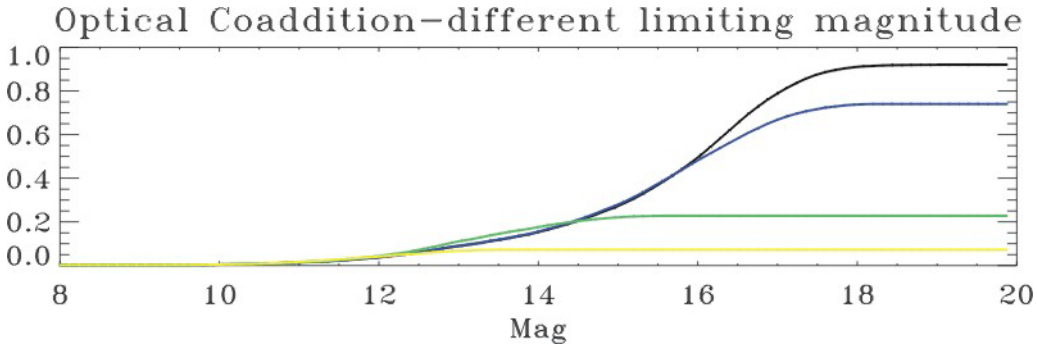

Figure 71: South Galactic Pole coverage for optical LO - GLAO approach. Here have been considered the different limiting magnitudes for the single reference stars and at most 18 reference stars over the 4arcmin FoV. The different lines colours represent different limit on limit magnitude of each reference stars: 15, 17, 19.5 and 21 going from the bottom to the top. Sky coverage in ordinate.

Integr. / Single Star	14	15	16	17	18	19
21	0.155	0.279	0.495	**0.789**	**0.911**	**0.920**
19.5	0.155	0.279	0.482	0.668	0.738	0.740
17	0.176	0.221	0.228	0.228	0.228	0.228

Table 19: Results relative to South Galactic Pole. 4armin FoV has been considered.

- **b 50 l +90**

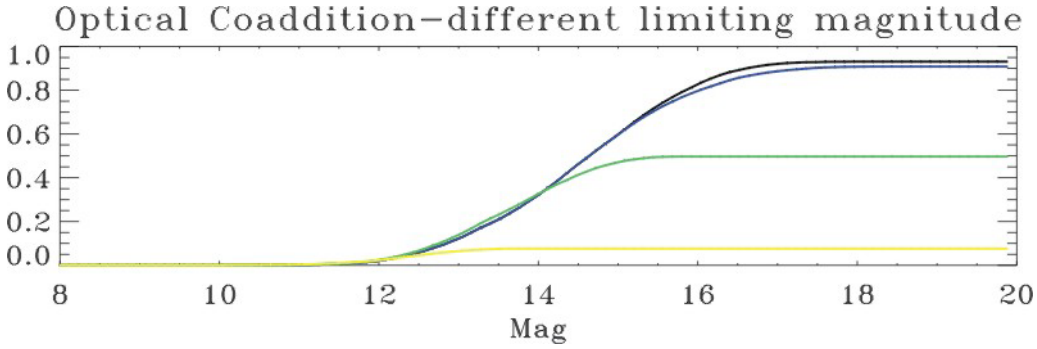

Figure 72 Mid galactic latitude North case coverage for optical LO - GLAO approach. Here have been considered the different limiting magnitudes for the single reference stars and at most 18 reference stars over the 4arcmin FoV. The different lines colours represent different limit on limit magnitude of each reference stars: 15, 17, 19.5 and 21 going from the bottom to the top. Sky coverage in ordinate.

Integr. / Single Star	14	15	16	17	18	19
21	0.321	0.598	**0.827**	**0.920**	**0.930**	**0.931**
19.5	0.321	0.596	**0.797**	**0.887**	**0.908**	**0.908**
17	0.326	0.471	0.497	0.497	0.497	0.497

Table 20: Results relative to mid galactic latitude North case. 4armin FoV has been considered.

- **b -50 l +270**

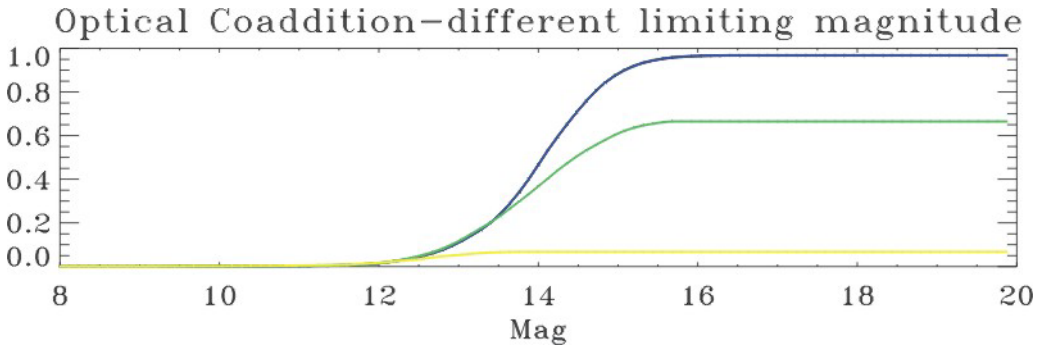

Figure 73: Mid galactic latitude South case coverage for optical LO - GLAO approach. Here have been considered the different limiting magnitudes for the single reference stars and at most 18 reference stars over the 4arcmin FoV. The different lines colours represent different limit on limit magnitude of each reference stars: 15, 17, 19.5 and 21 going from the bottom to the top. Sky coverage in ordinate.

Integr. / Single Star	14	15	16	17	18	19
21	0.466	**0.884**	**0.965**	**0.968**	**0.968**	**0.968**
19.5	0.466	**0.884**	**0.965**	**0.968**	**0.968**	**0.968**
17	0.367	0.610	0.665	0.665	0.665	0.665

Table 21: Results relative to mid galactic latitude South case. 4armin FoV has been considered.

- **Coma cluster**

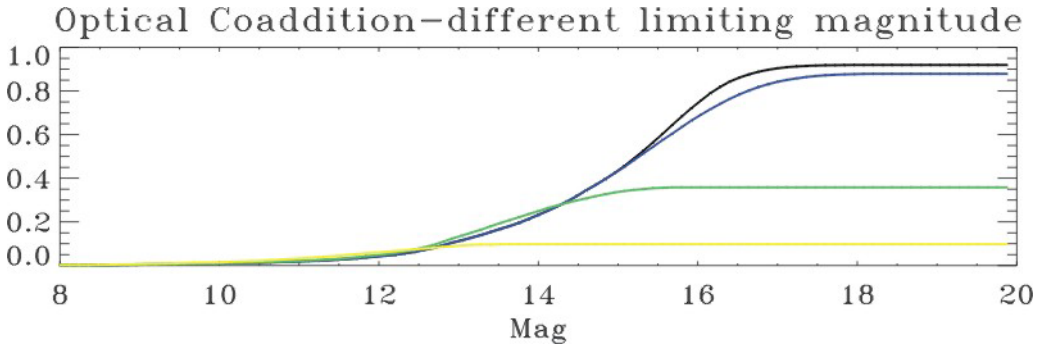

Figure 74: Coma cluster case coverage for optical LO - GLAO approach. Here have been considered the different limiting magnitudes for the single reference stars and at most 18 reference stars over the 4arcmin FoV. The different lines colours represent different limit on limit magnitude of each reference stars: 15, 17, 19.5 and 21 going from the bottom to the top. Sky coverage in ordinate.

Integr. / Single Star	14	15	16	17	18	19
21	0.232	0.435	0.745	**0.904**	**0.919**	**0.919**
19.5	0.232	0.432	0.682	**0.842**	**0.878**	**0.879**
17	0.249	0.337	0.358	0.358	0.358	0.358

Table 22: Results relative to Coma cluster case. 4armin FoV has been considered.

- **Virgo cluster**

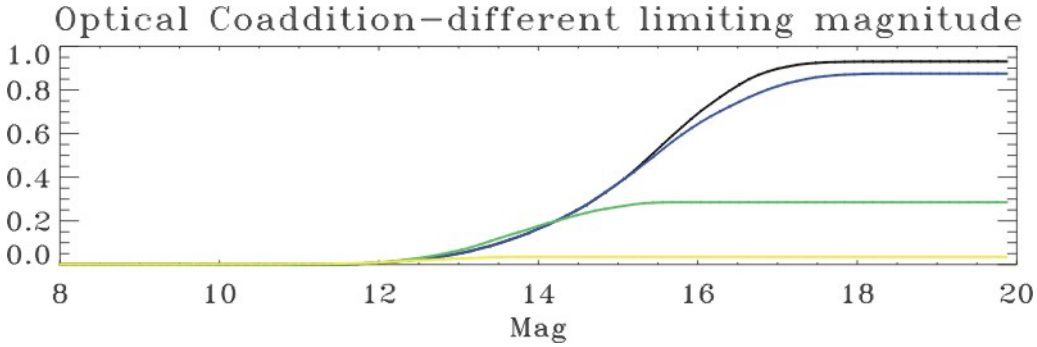

Figure 75: Virgo cluster case coverage for optical LO - GLAO approach. Here have been considered the different limiting magnitudes for the single reference stars and at most 20 reference stars over the 4arcmin FoV. The different lines colours represent different limit on limit magnitude of each reference stars: 15, 17, 19.5 and 21 going from the bottom to the top. Sky coverage stays in ordinate and it goes from 0 to 1. The case with 15 magnitude limiting star is senseless.

Integr. / Single Star	14	15	16	17	18	19
21	0.163	0.372	0.692	**0.897**	**0.930**	**0.931**
19.5	0.165	0.371	0.644	**0.817**	**0.873**	**0.875**
17	0.177	0.264	0.286	0.286	0.286	0.286

Table 23: Results relative to the Virgo cluster case. 4armin FoV has been considered. In bold style the sky coverage values greater than 0.75 have been written.

10.2.1.2 Layer Oriented Numerical coaddition/ Star Oriented

In this case the number references depends on the number of available WFS. The relationship between this number and the achievable sky-coverage is fundamental. In fact we analyzed three different cases with: three, six and twelve WFS/reference. From this analysis came out that for faint limiting magnitude as it is the case we are investigating. Moreover was investigated the dependency by the limit magnitude of the single reference star. Such as for the previous case with optical coaddition has been considered if the barycenter of the field is inside the central 2arcmin, but no weight has been applied.

Because of numerical coaddition (or SO approach) no limit on the magnitude range of the reference stars it is theoretically necessary to assure correction uniformity. This is definitely true if the Signals of the each reference are high enough, otherwise a numerical weight on the different signal should be applied in order to minimize the noise on the Ground layer measurement (according to uniformity constraints). In this study no such optimize has been performed but to let it possible a 7 magnitude range has been chosen.

- **North Galactic Pole**

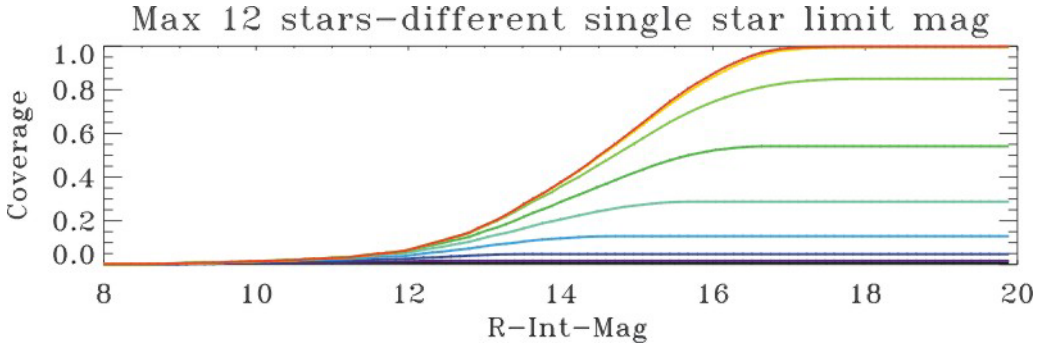

Figure 76: The picture shows North Galactic Pole coverage for a Numerical LO or SO GLAO approach with 12 reference stars. The different colours represent different limit magnitude of the single reference stars (from 21 to 14 going from the top to the bottom). Sky coverage in ordinate.

Integr / Single Star	14		15		16		17		18		19	
	4'	**6'**	**4'**	**6'**	**4'**	**6'**	**4'**	**6'**	**4'**	**6'**	**4'**	**6'**
13	0.007	0.013	0.007	0.013	0.007	0.013	0.007	0.013	0.007	0.013	0.007	0.013
14	0.016	0.039	0.016	0.039	0.016	0.039	0.016	0.039	0.016	0.039	0.016	0.039
15	0.047	0.127	0.047	0.127	0.047	0.127	0.047	0.127	0.047	0.127	0.047	0.127
16	0.120	0.297	0.129	0.313	0.129	0.313	0.129	0.313	0.129	0.313	0.129	0.313
17	0.206	0.472	0.270	0.549	0.287	0.560	0.287	0.560	0.287	0.560	0.287	0.560
18	0.287	0.614	0.424	**0.749**	0.522	**0.789**	0.541	**0.791**	0.541	**0.791**	0.541	**0.791**
19	0.356	0.716	0.560	**0.890**	0.743	**0.939**	**0.833**	**0.945**	**0.849**	**0.945**	**0.849**	**0.945**
20	0.374	**0.766**	0.618	**0.952**	**0.858**	**0.993**	**0.983**	**0.997**	**0.995**	**0.997**	**0.996**	**0.997**
21	0.377	**0.775**	0.628	**0.957**	**0.873**	**0.994**	**0.991**	**0.997**	**0.998**	**0.997**	**0.998**	**0.997**

Table 24: In this table the result for the N=12 stars on NGP. Different rows correspond to different limiting magnitude of each reference stars. Different columns to different integrated magnitudes. Each integrated magnitude column is divided in two: left for 4arcmin FoV case (in red), right for the 6arcmin FoV (in blue). In bold style the sky coverage values greater than 0.75 have been written.

- **South Galactic Pole**

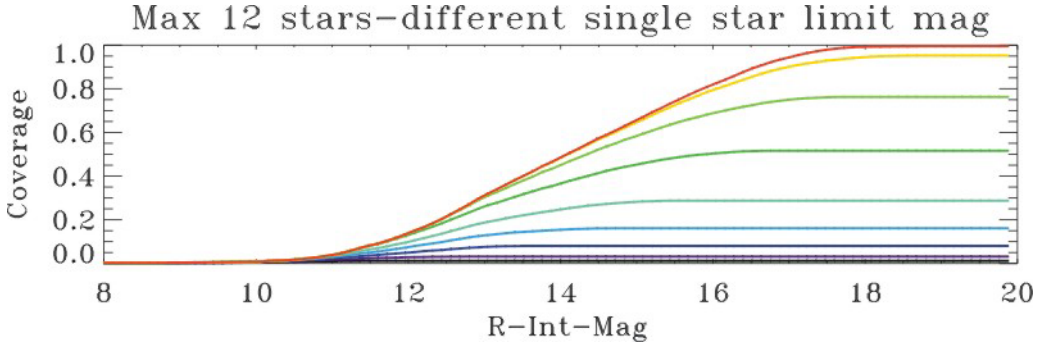

Figure 77: The picture shows South Galactic Pole coverage for a Numerical LO or SO GLAO approach with 12 reference stars. The different colours represent different limit magnitude of the single reference stars (from 21 to 14 going from the top to the bottom). Sky coverage in ordinate.

Integr. / Single Star	14		15		16		17		18		19	
	4'	**6'**	**4'**	**6'**	**4'**	**6'**	**4'**	**6'**	**4'**	**6'**	**4'**	**6'**
13	0.012	0.029	0.012	0.029	0.012	0.029	0.012	0.029	0.012	0.029	0.012	0.029
14	0.032	0.097	0.032	0.097	0.032	0.097	0.032	0.097	0.032	0.097	0.032	0.097
15	0.081	0.219	0.081	0.219	0.081	0.219	0.081	0.219	0.081	0.219	0.081	0.219
16	0.155	0.390	0.162	0.398	0.162	0.398	0.162	0.398	0.162	0.398	0.162	0.398
17	0.247	0.540	0.282	0.570	0.287	0.574	0.287	0.574	0.287	0.574	0.287	0.574
18	0.366	0.697	0.453	**0.757**	0.503	**0.775**	0.516	**0.778**	0.516	**0.778**	0.516	**0.778**
19	0.451	**0.787**	0.584	**0.869**	0.688	**0.900**	**0.750**	**0.907**	**0.762**	**0.908**	**0.762**	**0.908**
20	0.483	**0.823**	0.647	**0.922**	**0.794**	**0.964**	**0.901**	**0.972**	**0.945**	**0.973**	**0.952**	**0.973**
21	0.486	**0.831**	0.656	**0.934**	**0.819**	**0.975**	**0.943**	**0.981**	**0.992**	**0.993**	**0.995**	**0.995**

Table 25: In this table the result for the N=12 stars on SGP. Different rows correspond to different limiting magnitude of each reference stars. Different columns to different integrated magnitudes. Each integrated magnitude column is divided in two: left for 4arcmin FoV case (in red), right for the 6arcmin FoV (in blue). In bold style the sky coverage values greater than 0.75 have been written.

- **b 50 l +90**

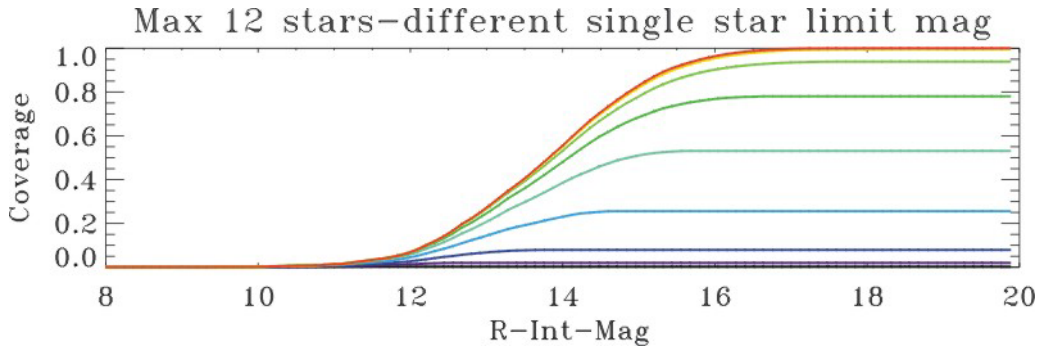

Figure 78: The picture shows Mid Galactic North coverage case for a Numerical LO or SO GLAO approach with 12 reference stars. The different colours represent different limit magnitude of the single reference stars (from 21 to 14 going from the top to the bottom). Sky coverage in ordinate.

Integr / Single Star	14	15	16	17	18	19
13	0.003	0.003	0.003	0.003	0.003	0.003
14	0.020	0.020	0.020	0.020	0.020	0.020
15	0.079	0.079	0.079	0.079	0.079	0.079
16	0.230	0.256	0.256	0.256	0.256	0.256
17	0.385	0.511	0.531	0.531	0.531	0.531
18	0.481	0.685	**0.768**	**0.780**	**0.780**	**0.780**
19	0.531	**0.779**	**0.902**	**0.935**	**0.939**	**0.939**
20	0.550	**0.820**	**0.954**	**0.990**	**0.995**	**0.995**
21	0.555	**0.830**	**0.964**	**0.997**	**0.999**	**0.999**

Table 26: In this table the result for the N=12 stars on mid-galactic altitude case north. Different rows correspond to different limiting magnitude of each reference stars. Different columns to different integrated magnitudes. In bold style the sky coverage values greater than 0.75 have been written.

- **b -50 l +270**

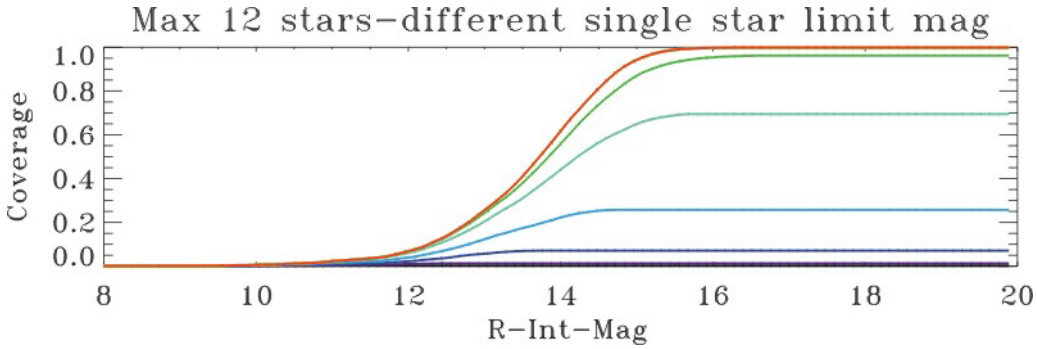

Figure 79: The picture shows Mid South Galactic case coverage for a Numerical LO or SO GLAO approach with 12 reference stars. The different colours represent different limit magnitude of the single reference stars (from 21 to 14 going from the top to the bottom). Sky coverage in ordinate.

Integr. / Single Star	14		15		16		17		18		19	
	4'	**6'**	**4'**	**6'**	**4'**	**6'**	**4'**	**6'**	**4'**	**6'**	**4'**	**6'**
13	0.003	0.005	0.003	0.005	0.003	0.005	0.003	0.005	0.003	0.005	0.003	0.005
14	0.013	0.045	0.013	0.045	0.013	0.045	0.013	0.045	0.013	0.045	0.013	0.045
15	0.072	0.188	0.072	0.188	0.072	0.188	0.072	0.188	0.072	0.188	0.072	0.188
16	0.223	0.495	0.259	0.521	0.259	0.521	0.259	0.521	0.259	0.521	0.259	0.521
17	0.440	**0.806**	0.650	**0.863**	0.695	**0.867**	0.695	**0.867**	0.695	**0.867**	0.695	**0.867**
18	0.558	**0.947**	**0.870**	**0.986**	**0.954**	**0.987**	**0.962**	**0.987**	**0.962**	**0.987**	**0.962**	**0.987**
19	0.617	**0.967**	**0.942**	**0.998**	**0.997**	**0.999**	**0.998**	**0.999**	**0.998**	**0.999**	**0.998**	**0.999**
20	0.617	**0.967**	**0.942**	**0.998**	**0.997**	**0.999**	**0.998**	**0.999**	**0.998**	**0.999**	**0.998**	**0.999**
21	0.618	**0.967**	**0.943**	**0.998**	**0.997**	**0.999**	**0.998**	**0.999**	**0.998**	**0.999**	**0.998**	**0.999**

Table 27: In this table the result for the N=12 stars on mid-galactic altitude case south. Different rows correspond to different limiting magnitude of each reference stars. Different columns refer to different integrated magnitudes. Each integrated magnitude column is divided in two: left for 4arcmin FoV case (in red), right for the 6arcmin FoV (in blue). In bold style the sky coverage values greater than 0.75 have been written.

- **Coma cluster**

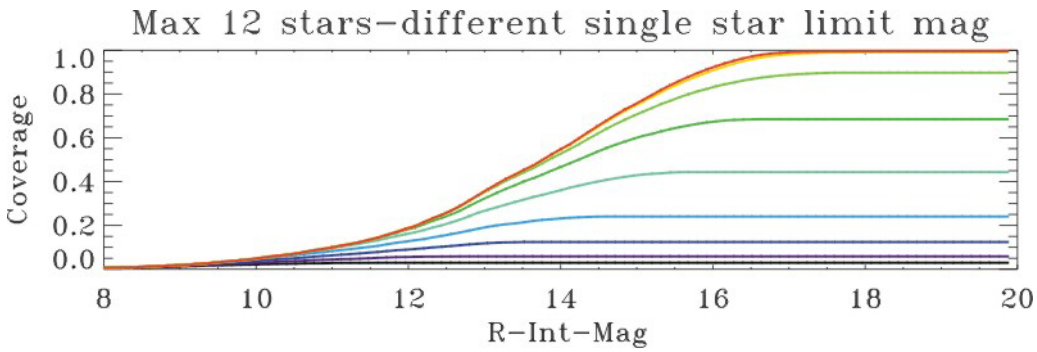

Figure 80: The picture shows Coma cluster sky-coverage for a Numerical LO or SO GLAO approach with 12 reference stars. The different colours represent different limit magnitude of the single reference stars (from 21 to 14 going from the top to the bottom). Sky coverage in ordinate.

Integr / Single Star	14		15		16		17		18		19	
	4'	**6'**	**4'**	**6'**	**4'**	**6'**	**4'**	**6'**	**4'**	**6'**	**4'**	**6'**
13	0.030	0.064	0.030	0.064	0.030	0.064	0.030	0.064	0.030	0.064	0.030	0.064
14	0.059	0.148	0.059	0.148	0.059	0.148	0.059	0.148	0.059	0.148	0.059	0.148
15	0.125	0.306	0.125	0.306	0.125	0.306	0.125	0.306	0.125	0.306	0.125	0.306
16	0.232	0.489	0.240	0.496	0.240	0.496	0.240	0.496	0.240	0.496	0.240	0.496
17	0.360	0.660	0.429	0.702	0.444	0.708	0.444	0.708	0.444	0.708	0.444	0.708
18	0.467	**0.786**	0.601	**0.854**	0.673	**0.872**	0.685	**0.873**	0.685	**0.873**	0.685	**0.873**
19	0.528	**0.853**	0.707	**0.940**	**0.831**	**0.963**	**0.888**	**0.966**	**0.897**	**0.966**	**0.897**	**0.965**
20	0.545	**0.878**	**0.750**	**0.967**	**0.908**	**0.991**	**0.981**	**0.992**	**0.991**	**0.992**	**0.991**	**0.992**
21	0.548	**0.884**	**0.757**	**0.971**	**0.922**	**0.992**	**0.991**	**0.992**	**0.992**	**0.992**	**0.992**	**0.992**

Table 28: In this table the result for the N=12 stars on Coma. Different rows correspond to different limiting magnitude of each reference stars. Different columns refer to different integrated magnitudes. Each integrated magnitude column is divided in two: left for 4arcmin FoV case (in red), right for the 6arcmin FoV (in blue). In bold style the sky coverage values greater than 0.75 have been written.

- **Virgo cluster**

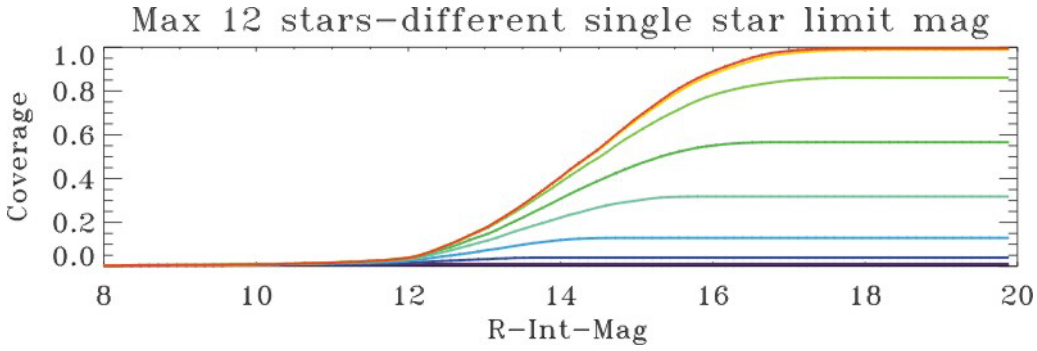

Figure 81: The picture shows Virgo Cluster sky-coverage for a Numerical LO or SO GLAO approach with 12 reference stars. The different colours represent different limit magnitude of the single reference stars (from 21 to 14 going from the top to the bottom). Sky coverage in ordinate.

Integr. / Single Star	14		15		16		17		18		19	
	4'	**6'**	**4'**	**6'**	**4'**	**6'**	**4'**	**6'**	**4'**	**6'**	**4'**	**6'**
13	0.005	0.007	0.005	0.007	0.005	0.007	0.005	0.007	0.005	0.007	0.005	0.007
14	0.010	0.033	0.010	0.033	0.010	0.033	0.010	0.033	0.010	0.033	0.010	0.033
15	0.039	0.138	0.039	0.138	0.039	0.138	0.039	0.138	0.039	0.138	0.039	0.138
16	0.119	0.339	0.130	0.352	0.130	0.352	0.130	0.352	0.130	0.352	0.130	0.352
17	0.226	0.544	0.300	0.609	0.319	0.618	0.319	0.618	0.319	0.618	0.319	0.618
18	0.309	0.676	0.463	**0.786**	0.551	**0.812**	0.566	**0.815**	0.566	**0.815**	0.566	**0.815**
19	0.383	**0.774**	0.611	**0.915**	**0.782**	**0.947**	**0.848**	**0.951**	**0.861**	**0.951**	**0.861**	**0.951**
20	0.404	**0.809**	0.668	**0.960**	**0.876**	**0.992**	**0.956**	**0.996**	**0.988**	**0.996**	**0.990**	**0.996**
21	0.407	**0.815**	0.678	**0.964**	**0.889**	**0.994**	**0.983**	**0.997**	**0.994**	**0.997**	**0.995**	**0.997**

Table 29: In this table the result for the N=12 stars on Virgo. Different rows correspond to different limiting magnitude of each reference stars. Different columns refer to different integrated magnitudes. Each integrated magnitude column is divided in two: left for 4arcmin FoV case (in red), right for the 6arcmin FoV (in blue). In bold style the sky coverage values greater than 0.75 have been written.

10.2.1.3 Overall considerations GLAO case

From the analysis performed appears a sky-coverage of at least 75% is achievable using a technology or a technique able to use 19th magnitude star as valid guide source. With this assumption the integrated magnitude 16th can be achieved in more than 75% percent of the cases us.

The analysis shows that the coverage for the Layer Oriented approach with optical coaddition characterized by a limiting 15th magnitude of the single reference star is betwen 10% and 25% with a 6arcmin FoV while in the 4 arcmin case is much lower. In this case (4') at least the 17th limit magnitude is needed.

One of the most relevant outcomes is the gain of ~1 integrated magnitude going from 4' to 6' arcmin (taking constant skycoverage). This translates in a gain on the achievable results shifting performances one magnitude ahead.

The computation for the Layer Oriented optical coaddition has been performed considering a WFS that coadds the lights of all references on a single detector conjugated to the ground, actually in section **Split LO-WFS SOLUTION** we describe a WFS with 6arcmin annular FoV divided in 6 regions of 4.4square arcsec each (1.8 in the 4arcmin solution): the optical coadd is performed in each of the 6regions by a sub-WFS and then the computed 6 WF derivatives are coadded numerically in order to obtain a single signal to drive the Ground Layer DM. The constraint about the limit on the magnitude range (3.5 Mag in this analysis) falls, because the integration of the signals, coming from the different 6regions, could take into account the different illuminations giving the proper weights to each sub-signal. Actually the limit on the magnitude range still remains only on the reference stars optically coadded in each of the sub-WFS. In practice this translates on a gain in sky-coverage with respect to the analysis presented above. Moreover the possibility to use also only one star for each sub-region gives a pure numerical WFS system for free. In practice it could be seen as numerical WFS with, at most, 6 reference stars on a large FoV (up to 4 or to 6 arcmin according to the design), even if they should stay in the 6 sub-regions.

Integr / Single	14		15		16		17		18		19	
	4'	**6'**	**4'**	**6'**	**4'**	**6'**	**4'**	**6'**	**4'**	**6'**	**4'**	**6'**
Virgo	0.388	**0.789**	0.645	**0.950**	**0.852**	**0.992**	**0.967**	**0.997**	**0.994**	**0.997**	**0.995**	**0.997**
Coma	0.529	**0.861**	0.733	**0.965**	**0.893**	**0.990**	**0.981**	**0.992**	**0.996**	**0.992**	**0.996**	**0.992**
b-50 l270	0.572	**0.932**	**0.897**	**0.997**	**0.995**	**0.999**	**0.998**	**0.999**	**0.998**	**0.999**	**0.998**	**0.999**
b50 l90	0.343	**0.926**	0.547	**0.991**	0.737	**0.998**	**0.832**	**0.998**	**0.849**	**0.998**	**0.849**	**0.998**
SGP	0.397	**0.799**	0.550	**0.917**	0.722	**0.972**	**0.894**	**0.982**	**0.981**	**0.982**	**0.995**	**0.982**
NGP	0.358	0.744	0.597	**0.940**	**0.826**	**0.992**	**0.969**	**0.997**	**0.997**	**0.997**	**0.997**	**0.997**

Table 30: In this table we list the sky coverage results (from 0. to 1.) for the 2×2 degrees fields analysed. The system is a numerical WFS with at most 6 reference stars, which barycentre lays in the central 2arcmin. Each integrated magnitude column is divided in two: left for 4arcmin FoV case (in red), right for the 6arcmin FoV (in blue). In bold style the sky coverage values greater than 0.75 have been written.

10.2.2 MCAO sky coverage

For the MCAO case a standard 2 arcmin FoV has been considered to look for reference stars. As for the GLAO case the two different approaches, LO and SO, as been considered and for both different setups of the adaptive systems has been investigated. Layer Oriented Optical coaddition

In the optical coaddition there is no limitation on the brightness and the number of reference stars, here a limit of 18 has been taken into account and for the references the 21st limit magnitude is given directly by the catalogue. A limiting difference of 3.5 Mag among the stars has been considered.

- **North Galactic Pole**

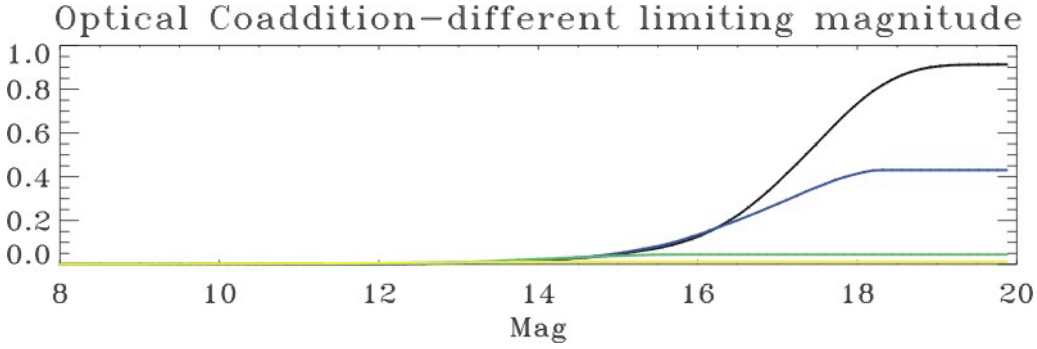

Figure 82: North Galactic Pole coverage for optical LO - MCAO approach. Here have been considered the different limiting magnitudes for the single reference stars and at most 20 reference stars over the 2arcmin FoV. The different lines colours represent different limit on limit magnitude of each reference stars: 15, 17, 19.5 and 21 going from the bottom to the top. Sky coverage in ordinate.

Integr. / Single Star	14	15	16	17	18	19
21	0.018	0.046	0.126	0.374	0.735	**0.904**
19.5	0.019	0.050	0.135	0.276	0.414	0.431

Table 31: Results relative to North Galactic Pole. Values go from 0 to 1, results for magnitude limit 15 and 17 have not been presented because lower then 0.1 (at best).

- **South Galactic Pole**

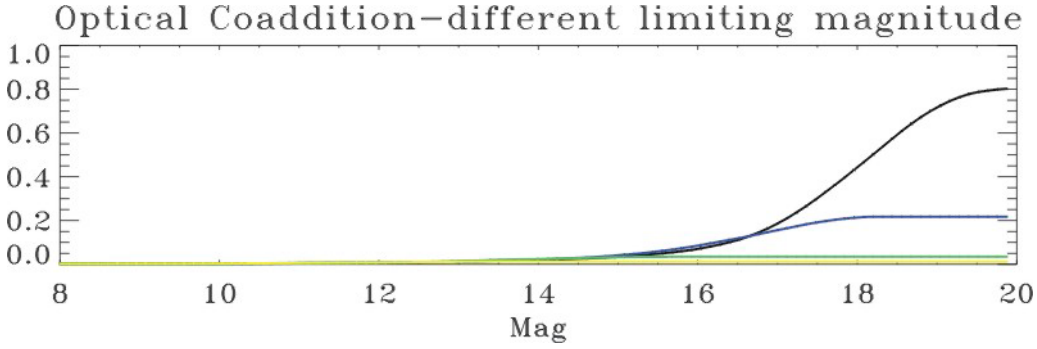

Figure 83 South Galactic Pole coverage for optical LO - MCAO approach. Here have been considered the different limiting magnitudes for the single reference stars and at most 20 reference stars over the 2arcmin FoV. The different lines colours represent different limit on limit magnitude of each reference stars: 15, 17, 19.5 and 21 going from the bottom to the top. Sky coverage in ordinate.

Integr. / Single Star	14	15	16	17	18	19
21	0.018	0.034	0.070	0.186	0.443	0.716
19.5	0.021	0.041	0.085	0.156	0.214	0.217

Table 32: Results relative to South Galactic Pole.

- **b 50 l +90**

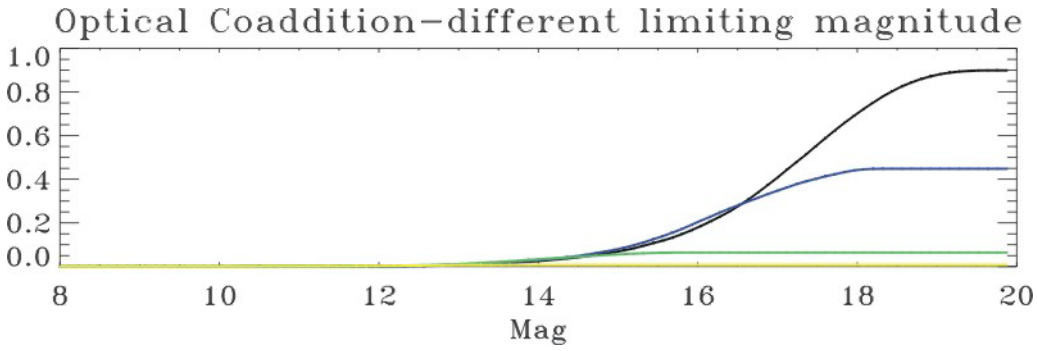

Figure 84: Mid galactic latitude North case coverage for optical LO - MCAO approach. Here have been considered the different limiting magnitudes for the single reference stars and at most 20 reference stars over the 4arcmin FoV. The different lines colours represent different limit on limit magnitude of each reference stars: 15, 17, 19.5 and 21 going from the bottom to the top. Sky coverage in ordinate.

Integr. / Single Star	14	15	16	17	18	19
21	0.025	0.069	0.179	0.408	0.701	**0.878**
19.5	0.028	0.080	0.204	0.347	0.443	0.448

Table 33: Results relative to mid galactic latitude North case.

- **b -50 l +270**

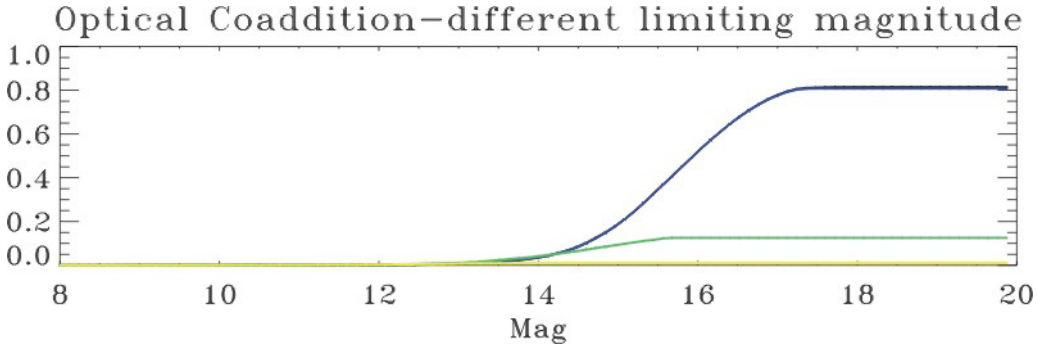

Figure 85: Mid galactic latitude South case coverage for optical LO - MCAO approach. Here have been considered the different limiting magnitudes for the single reference stars and at most 20 reference stars over the 2arcmin FoV. The different lines colours represent different limit on limit magnitude of each reference stars: 15, 17, 19.5 and 21 going from the bottom to the top. Sky coverage in ordinate.

Integr. / Single Star	14	15	16	17	18	19
21	0.036	0.187	0.519	**0.778**	**0.814**	**0.815**
19.5	0.036	0.189	0.519	**0.777**	**0.808**	**0.808**
17	0.041	0.094	0.125	0.125	0.125	0.125

Table 34: Results relative to mid galactic latitude South case.

- **Coma cluster**

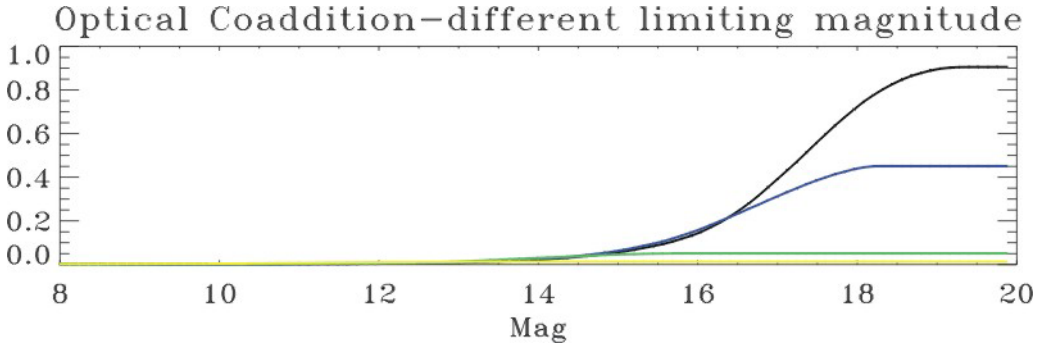

Figure 86 Coma cluster case coverage for optical LO - MCAO approach. Here have been considered the different limiting magnitudes for the single reference stars and at most 20 reference stars over the 2arcmin FoV. The different lines colors represent different limit on limit magnitude of each reference stars: 15, 17, 19.5 and 21 going from the bottom to the top. Sky coverage in ordinate.

Integr / Single Star	14	15	16	17	18	19
21	0.022	0.056	0.143	0.392	0.732	**0.895**
19.5	0.024	0.063	0.157	0.313	0.441	0.451

Table 35: Results relative to Coma cluster case.

- **Virgo cluster**

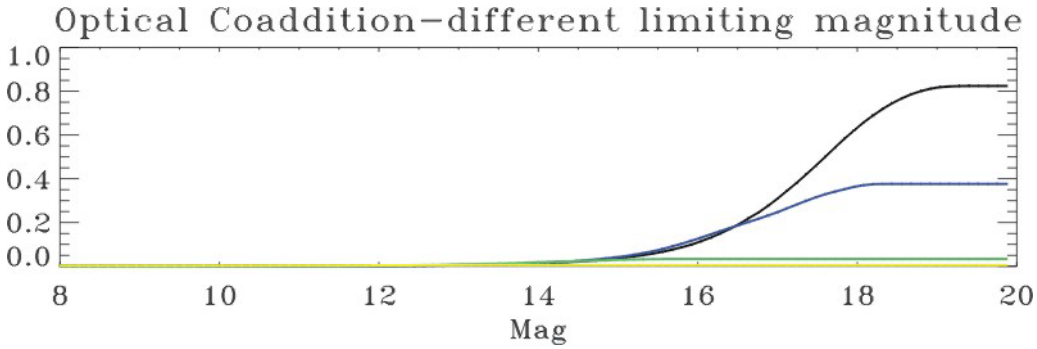

Figure 87: Virgo cluster case coverage for optical LO - MCAO approach. Here have been considered the different limiting magnitudes for the single reference stars and at most 20 reference stars over the 2arcmin FoV. The different lines colours represent different limit on limit magnitude of each reference stars: 15, 17, 19.5 and 21 going from the bottom to the top. Sky coverage in ordinate.

Integr. / Single Star	14	15	16	17	18	19
21	0.013	0.036	0.109	0.309	0.634	**0.817**
19.5	0.015	0.042	0.126	0.248	0.366	0.376

Table 36: Results relative to the Virgo cluster case. In bold style the sky coverage values greater than 0.75 have been written.

10.2.2.1 Layer Oriented Numerical coaddition/ Star Oriented

In this case the references number depends on the number of available WFS. The relationship between this number and the achievable sky-coverage is fundamental. In fact we analyzed three different cases with: three, six and twelve WFS/reference. Moreover was investigated the dependency by the limit magnitude of the single reference star. Such as for the previous case with optical coaddition has been considered if the barycenter of the field is inside the central 2arcmin, but no weight has been applied.

Because of numerical coaddition (or SO approach) no limit on the magnitude range of the reference stars it is theoretically necessary to assure correction uniformity. This is definitely true if the Signals of the each reference are high enough, otherwise a numerical weight on the different signal should be applied in order to minimize the noise on the Ground layer measurement (according to uniformity constraints). In this study no such optimize has been performed but to let it possible a 7 magnitude range has been chosen.

- **North Galactic Pole**

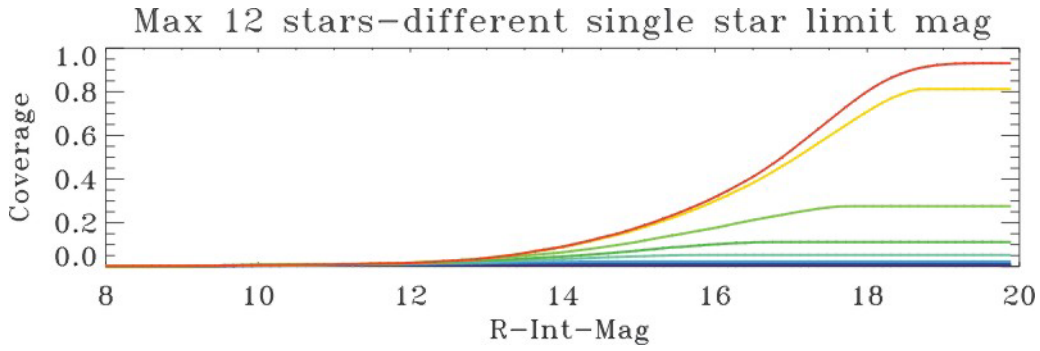

Figure 88: The picture shows North Galactic Pole coverage for a Numerical LO or SO MCAO approach. From the top to the bottom respectively with 3, 6 and 12 reference stars. The different lines colours represent different limit magnitude of the single reference stars (from 21 to 14 going from the top to the bottom). Sky coverage in ordinate.

Integr. / Single Star	14	15	16	17	18	19
13	0.004	0.004	0.004	0.004	0.004	0.004
14	0.006	0.006	0.006	0.006	0.006	0.006
15	0.012	0.012	0.012	0.012	0.012	0.012
16	0.020	0.022	0.022	0.022	0.022	0.022
17	0.033	0.046	0.052	0.052	0.052	0.052
18	0.045	0.073	0.101	0.111	0.111	0.111
19	0.065	0.114	0.176	0.244	0.276	0.276
20	0.089	0.172	0.300	0.483	0.709	**0.812**
21	0.090	0.180	0.317	0.531	**0.801**	**0.925**

Table 37: In this table the result for the N=12 stars on NGP. Different rows correspond to different limiting magnitude of each reference stars. Different columns to different integrated magnitudes. The selected reference are lying in the 2 arcmin central FoV. In bold style the sky coverage values greater than 0.75 have been written.

- **South Galactic Pole**

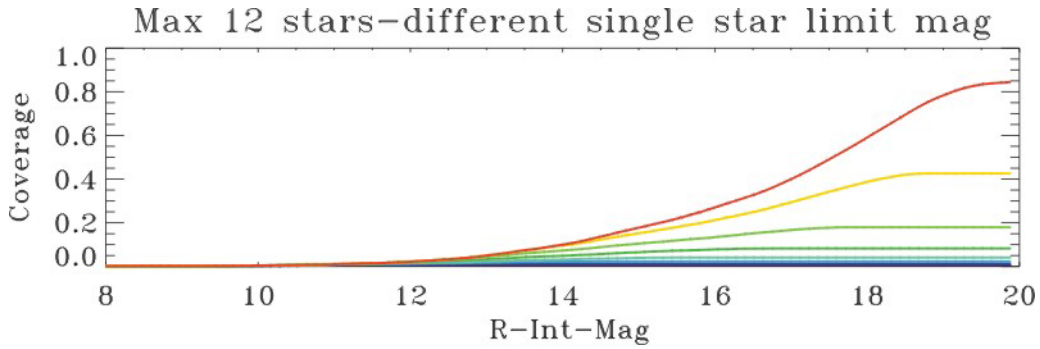

Figure 89: The picture shows South Galactic Pole coverage for a Numerical LO or SO MCAO approach. Here the case with 12 reference stars is presented. The different colours represent different limit magnitude of the single reference stars (from 21 to 14 going from the top to the bottom). Sky coverage in ordinate.

Integr. / Single Star	14	15	16	17	18	19
13	0.005	0.005	0.005	0.005	0.005	0.005
14	0.008	0.008	0.008	0.008	0.008	0.008
15	0.013	0.013	0.013	0.013	0.013	0.013
16	0.022	0.023	0.023	0.023	0.023	0.023
17	0.032	0.039	0.041	0.041	0.041	0.041
18	0.049	0.065	0.078	0.082	0.082	0.082
19	0.073	0.104	0.134	0.167	0.179	0.179
20	0.096	0.152	0.212	0.293	0.387	0.426
21	0.099	0.177	0.270	0.400	0.591	**0.783**

Table 38: In this table the result for the N=12 stars on SGP. Different rows correspond to different limiting magnitude of each reference stars. Different columns to different integrated magnitudes. In bold style the sky coverage values greater than 0.75 have been written.

- **b 50 l +90**

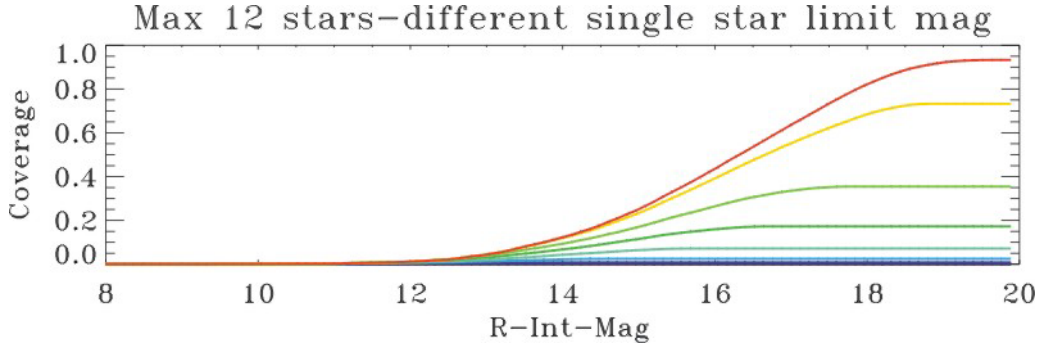

Figure 90: The picture shows South Galactic Pole coverage for a Numerical LO or SO MCAO approach. Here the case with 12 reference stars is presented. The different colours represent different limit magnitude of the single reference stars (from 21 to 14 going from the top to the bottom, 1ΔMag). Sky coverage in ordinate.

Integr. / Single Star	14	15	16	17	18	19
13	0.001	0.001	0.001	0.001	0.001	0.001
14	0.017	0.017	0.017	0.017	0.017	0.017
15	0.081	0.081	0.081	0.081	0.081	0.081
16	0.022	0.025	0.025	0.025	0.025	0.025
17	0.043	0.064	0.072	0.072	0.072	0.072
18	0.067	0.115	0.160	0.173	0.173	0.173
19	0.093	0.170	0.264	0.335	0.355	0.355
20	0.119	0.233	0.392	0.552	0.685	0.732
21	0.123	0.251	0.435	0.636	**0.822**	**0.921**

Table 39: In this table the result for the N=12 stars on mid-galactic altitude case north. Different rows correspond to different limiting magnitude of each reference stars. Different columns to different integrated magnitudes. In bold style the sky coverage values greater than 0.75 have been written.

- **b -50 l +270**

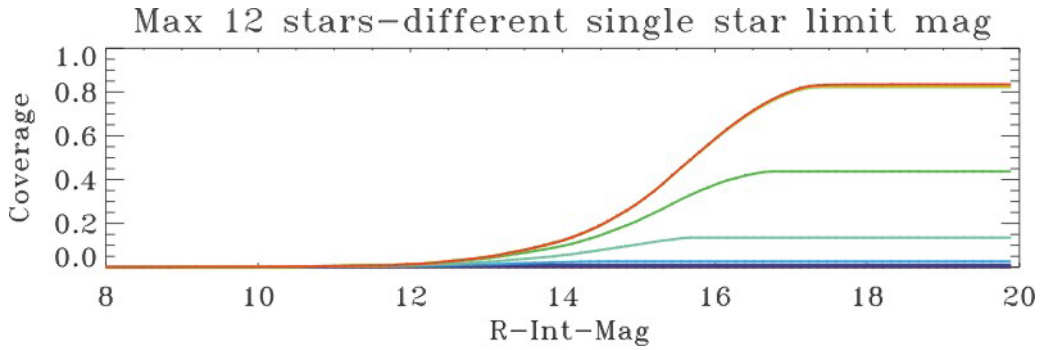

Figure 91: The picture shows South Galactic Pole coverage for a Numerical LO or SO MCAO approach. Here the case with 12 reference stars is presented. The different colours represent different limit magnitude of the single reference stars (from 21 to 14 going from the top to the bottom). Sky coverage in ordinate.

Integr. / Single Star	14	15	16	17	18	19
13	0.001	0.001	0.001	0.001	0.001	0.001
14	0.003	0.003	0.003	0.003	0.003	0.003
15	0.010	0.010	0.010	0.010	0.010	0.010
16	0.023	0.026	0.026	0.026	0.026	0.026
17	0.055	0.105	0.135	0.135	0.135	0.135
18	0.098	0.214	0.376	0.438	0.438	0.438
19	0.122	0.294	0.582	**0.797**	**0.823**	**0.823**
20	0.122	0.295	0.585	**0.801**	**0.830**	**0.830**
21	0.122	0.296	0.586	**0.804**	**0.834**	**0.834**

Table 40: In this table the result for the N=12 stars on mid-galactic altitude case south. Different rows correspond to different limiting magnitude of each reference stars. Different columns to different integrated magnitudes. In bold style the sky coverage values greater than 0.75 have been written.

- **Coma cluster**

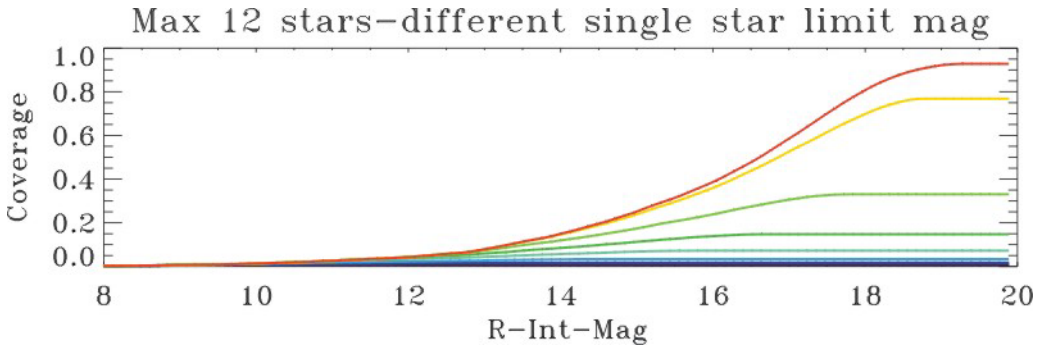

Figure 92: The picture shows South Galactic Pole coverage for a Numerical LO or SO MCAO approach. Here the case with 12 reference stars is presented. The different colours represent different limit magnitude of the single reference stars (from 21 to 14 going from the top to the bottom). Sky coverage stays in ordinate.

Integr. / Single Star	14	15	16	17	18	19
13	0.007	0.007	0.007	0.007	0.007	0.007
14	0.010	0.010	0.010	0.010	0.010	0.010
15	0.017	0.017	0.017	0.017	0.017	0.017
16	0.033	0.033	0.033	0.033	0.033	0.033
17	0.057	0.068	0.072	0.072	0.072	0.072
18	0.084	0.113	0.139	0.148	0.148	0.148
19	0.119	0.174	0.238	0.306	0.330	0.330
20	0.146	0.239	0.359	0.526	0.698	**0.768**
21	0.150	0.251	0.386	0.586	**0.807**	**0.921**

Table 41: In this table the result for the N=12 stars on Coma. Different rows correspond to different limiting magnitude of each reference stars. Different columns to different integrated magnitudes. In bold style the sky coverage values greater than 0.75 have been written.

- **Virgo cluster**

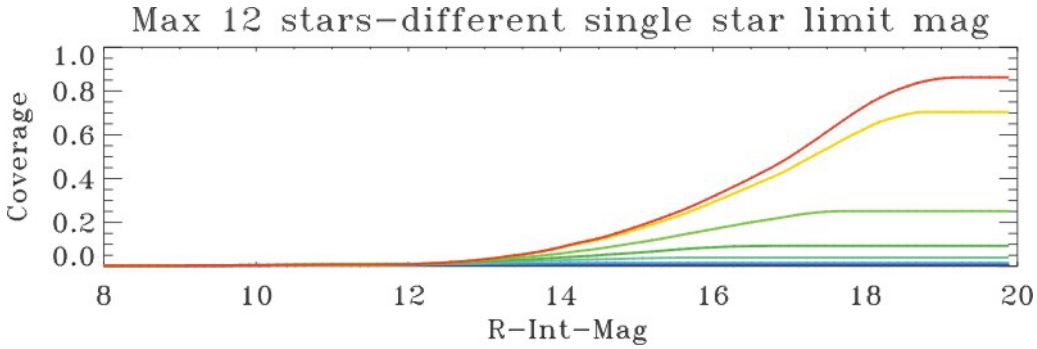

Figure 93: The picture shows South Galactic Pole coverage for a Numerical LO or SO MCAO approach. Here the case with 12 reference stars is presented. The different colours represent different limit magnitude of the single reference stars (from 21 to 14 going from the top to the bottom). Sky coverage in ordinate.

Integr. / Single Star	14	15	16	17	18	19
13	0.004	0.004	0.004	0.004	0.004	0.004
14	0.005	0.005	0.005	0.005	0.005	0.005
15	0.007	0.007	0.007	0.007	0.007	0.007
16	0.013	0.014	0.014	0.014	0.014	0.014
17	0.027	0.035	0.039	0.039	0.039	0.039
18	0.040	0.062	0.086	0.093	0.093	0.093
19	0.058	0.107	0.169	0.228	0.252	0.252
20	0.084	0.169	0.292	0.443	0.628	0.704
21	0.087	0.180	0.318	0.497	0.731	**0.857**

Table 42: In this table the result for the N=12 stars on Virgo. Different rows correspond to different limiting magnitude of each reference stars. Different columns refer to different integrated magnitudes. In bold style the sky coverage values greater than 0.75 have been written.

10.3 Parameters and simulation conditions cross table for ONIRICA

Based on E. Marchetti – ESO – 12 May 2005, and updated documents.

10.3.1 Standard Atmosphere and seeing conditions

Seeing	**Good**			**Bad**		
r_o(0.5μm)	0.193 m			0.10559 m		
L_o	25 m			25 m		
Layer	*Height*	*Weight*	*Speed*	*Height*	*Weight*	*Speed*
1	0	0.33461	12.05	0	0.33461	2.05
2	600	0.22307	8.6	600	0.22307	5.6
3	1200	0.11154	18.6	1200	0.11154	6.6
4	2500	0.09041	12.4	2500	0.09041	10.4
5	5000	0.07960	8.0	5000	0.07960	8.0
6	9000	0.05156	33.7	7000	0.05156	20.7
7	11500	0.04499	23.2	9500	0.04499	18.2
8	12800	0.03391	22.2	11800	0.03391	22.2
9	14500	0.01911	8.0	13500	0.01911	8
10	18500	0.01120	10.0	16500	0.01120	10.0

Table 43: Standard Atmosphere and seeing conditions. The turbulence spectrum is Von-Karman. The good seeing condition has τ_o=4.0 ms and θ_o=3" both @ 0.5μm. The bad seeing condition has τ_o=2.5 ms and θ_o=3" both @ 0.5μm.

10.3.2 Atmosphere and seeing conditions for top level scientific targets

Seeing	λ/r_0=0.4arcsec			
r_o(0.5μm)	0.258 m			
L_o	25 m			
Layer	*Height*[m]	*Weight*	r_0 [m]	*Speed*
1	0	0.251439	0.590	12.05
2	600	0.167623	0.753	8.6
3	1200	0.0838155	1.141	18.6
4	2500	0.135875	0.854	12.4
5	5000	0.119629	0.928	8.0
6	9000	0.0774884	1.196	33.7
7	11500	0.0676145	1.298	23.2
8	12800	0.0509626	1.538	22.2
9	14500	0.0287200	2.170	8.0
10	18500	0.0168322	2.990	10.0

Table 44: In this table are listed the atmospheric parameters for the observation of the top scientific targets. The atmosphere has Von-Karman power spectrum where r_0 has not the common sense. Here r_0 are representing the overall power such as in Kolmogorov power spectrum.

Starting from the assumption that Superb scientific results could/should be achieved in the best cases of atmospheric condition we suppose to let the camera working on an atmosphere derived by the one above for "Standard Atmosphere and seeing conditions" table but with the overall amount of turbulence reduced down to a seeing of 0.3 arcsec (at V band=0.5μm). In particular we supposed that the ground layer, the powerful seeing component, is reduced by a factor 2 in weight with respect to the other altitude components.

Simulation Parameters	**ESO**	**SIRIO (to be compiled by INAF)**
GLAO		
Corrected FoV	6×6 arcmin	6x6 arcmin
Imaging bands	J-H-K	K then scaled to J and H
WFS (NGS) number	3 to 6	3 to 12
WFS type	SH and Pyramid	Pyramid (SH?)
NGS V magnitude	15 to 17	
Number of points in the	8 including the NGSs	9 on a square 1armin FoV
Simulation outputs	• PSF	• PSF
Other outputs	Sky coverage at Galactic poles and *b*=50°	Sky coverage at Galactic poles and *b*=50°
MCAO		
MCAO approach		Only LO, Optical/Numerical
Corrected FoV	2×2 and 3×3 arcmin	2arcmin
Imaging bands	J-H-K	K
WFS (NGS) Number	3 to 6	3 to 12
WFS type	SH and Pyramid	SH and Pyramid
NGS V magnitude	15 to 17	
Number of points in the FoV for correction estimation	8 including the NGSs (1 at the FoV center)	9 on a square 1armin FoV side
Simulation outputs (per position in the FoV)	• PSF • Strehl ratio	• PSF • Strehl Ratio
Other outputs	Sky coverage at Galactic poles and *b*=50°	Sky coverage at Galactic poles and *b*=50°

Table 45: Simulation contions cross check table. WFS L3CCD RON: 0e^-, WFS path bandwidth: 0.5-0.9 μm, Zero Point at m(V)=0 G0V star: 1.37×10^{10} photons/m^2/s, <u>this includes</u> already the 6 OWL mirrors (Ag coating 97%) and the WFS L3CCD QE + 50% QE reduction. <u>This doesn't include</u> the additional transmission of the AO optical, train which must be computed on the specific AO design.

<u>Deformable Mirrors</u>

For the deformable mirrors we believe in the availability of *LBT technology (25 mm pitch):*

DM	**Baseline**	**Goal**	**High order option**
M5	8Km altitude conjugation, 145×145 actuators (0.78m sampling)	8Km altitude conjugation, 185×185 actuators (0.61m sampling)	8KM or TBD conjugation, 300×300 (0.38m sampling)
M6	Pupil conjugation, 98×98 actuators (1.02m sampling)	Pupil conjugation, 125×125 actuators (0.80m sampling)	Pupil conjugation, 200×200 (0.50m sampling)

Table 46: M5 and M6 deformable mirror solutions.